MODEL-BASED CONTROL OF CARDIAC ALTERNANS ON ONE DIMENSIONAL TISSUE

A Thesis
Presented to
The Academic Faculty

by

Alejandro Garzon

In Partial Fulfillment
of the Requirements for the Degree
Doctor of Philosophy in the
School of Physics

Georgia Institute of Technology
December 2010

MODEL-BASED CONTROL OF CARDIAC ALTERNANS ON ONE DIMENSIONAL TISSUE

Approved by:

Professor Roman O. Grigoriev,
Advisor
School of Physics
Georgia Institute of Technology

Professor Thomas J. Burkholder
School of Applied Physiology
Georgia Institute of Technology

Professor Kurt Wiesenfeld
School of Physics
Georgia Institute of Technology

Professor Robert J. Butera
School of Electrical and Computer
Engineering
Georgia Institute of Technology

Professor Daniel I. Goldman
School of Physics
Georgia Institute of Technology

Date Approved: 16 August 2010

To my mother and

to the memory of my father.

ACKNOWLEDGEMENTS

I owe my deepest gratitude to my advisor, Dr. Roman O. Grigoriev, for helping me develop as a scientist and for providing his intuition that I transformed into concrete results in this work. I am also grateful to Dr. Flavio H. Fenton for sharing his experimental and modeling expertise which helped me bring this theoretical research closer to practical application. I also want to thank Dr. John F. Gibson for a brief but very useful communication concerning the Newton-Krylov method. Finally, I thank the thesis committee members whose suggestions helped improve this thesis and made it more accessible to a broader audience.

TABLE OF CONTENTS

LIST OF TABLES

LIST OF FIGURES

SUMMARY

When excitable cardiac tissue is electrically paced at a sufficiently high rate, the duration of excitation can alternate from beat to beat despite a constant stimulation period. This rhythm, known as alternans, has been identified as an early stage in a sequence of increasingly complex instabilities leading to the lethal arrhythmia ventricular fibrillation (VF). This connection served as as a motivation for research into the control of alternans as a strategy to prevent VF. Control methods that do not use a model of the dynamics have been used for the suppression of alternans. However, these methods possess limitations.

In this thesis we study theoretically model-based control techniques with the goal of developing protocols that would overcome the shortcomings of non model-based approaches. We consider one dimensional tissue in two different geometrical configurations: a ring and a fiber with free ends (open fiber). We apply standard control methods for linear time invariant systems to a stroboscopic map of the linearized dynamics around the normal rhythm. We found that, in the ring geometry, model-based control is able to suppress alternans faster and with lower current, thereby reducing the risk of tissue damage, compared with non-model-based control. In the open fiber, model-based control is able to suppress alternans for longer fibers and higher pacing frequencies in comparison with non-model-based control. The methodology presented here can be extended to two- and three-dimensional tissue, and could eventually lead to the suppression of alternans on the entire ventricles.

CHAPTER I

INTRODUCTION

The contraction of the heart is controlled by an electrical wave that originates at the sinus node, the heart's natural pacemaker. In order for the heart to pump, this wave (electrical activity) must propagate in a coordinated manner. Under some conditions the heart can transition into a state of turbulent electrical activity known as ventricular fibrillation (VF) [45]. During VF the contraction of the ventricles lacks the organization required for pumping blood. If circulation is not restored, death usually occurs within less than ten minutes due to lack of oxygen supply to vital organs.

VF has been associated with the clinical phenomenon of *sudden cardiac death* (SCD). SCD is generally defined as the unexpected death from cardiovascular causes within a period of 1 hour from the onset of symptoms, in a person without any prior condition that would appear fatal [23, 55]. SCD is one of the major causes of death in industrialized countries, exceeding 300 000 events per year in the United States, or about 20% of all deaths annually [56]. In 60% to 80% of cases, SCD occurs in the setting of coronary heart disease [92], a narrowing of the blood vessels that supply blood to the heart. In more that half of such cases coronary heart disease has not previously been diagnose and SCD occurs as its first symptom [15]. It is believed that most instances of SCD are caused by VF [52] or by ventricular tachycardia (VT), a state of fast contraction of the ventricles.

An important development for the treatment of VF is the implantable cardioverter-defibrillator (ICD), a device that is placed inside the chest cavity and that can terminate VT and VF by applying shocks of electric current. Although proven to have

decreased the arrhythmia-related mortality [66], due to its cost, complications and life-style limitations that it imposes, this therapy is not recommended for the population at large, but rather its administration is restricted to patients with a significant risk of SCD. The identification of this population at risk has remained a challenge [79].

Development of more efficient approaches to treatment of arrhythmias such as VF and VT requires detailed understanding of the electrophysiology of the cardiac tissue. At the scale of a single cell (cardiomyocite), the electrical activity is described by the transmembrane voltage, defined as the difference between the intracellular and extracellular electric potentials. Models of cell electrophysiology are usually formulated in terms of a set of coupled nonlinear ordinary differential equations (ODEs) representing the dynamics of the transmembrane voltage and the associated ionic currents across the cell membrane, with parameters chosen to reproduce experimental measurements. There is a variety of electrophysiological (ionic) models representing the differences between cell types and species (see Ref. [9]). When applied to tissue rather than single cells the ODE describing the transmembrane voltage is replaced with a partial differential equation (PDE) with a diffusion-like term representing electrical coupling between adjacent cells [27, 78].

These models reflect the basic property of cardiac cells to manifest excitable dynamics. The cells possess a stable rest state. When excited from that state by, for instance, a current injection exceeding a certain threshold, the voltage and the ionic currents undergo a transient excursion before returning to the resting state. Experimentally this excursion is often characterized by the increase of the transmembrane voltage above that of the rest state referred to as action potential. The duration of the excitation is correspondingly referred to as action potential duration (APD). In tissue, electrical coupling between cells gives rise to the propagation of waves of excitation. In particular, in atria and ventricles this excitation triggers the contraction

of the myocardial tissue.

Experimental evidence has established that excitation waves that circulate repeatedly thought the tissue at a rate higher than that of the sinus node (*reentrant waves*) underlie VF and VT [58, 70, 9]. Although many different mechanisms for the initiation and destabilization of reentrant waves have been proposed theoretically [1, 14, 80, 65, 26], it has been difficult to verify experimentally which mechanisms are responsible for the induction and development of fibrillation [45, 75, 90, 60, 42]. One of the mechanisms that has been the subject of much study is electrical alternans [63, 33], a long-short beat-to-beat alternation in APD that arises at fast pacing rates. At relatively low pacing rates and in small tissues, all the cells go through the same phase of the sequence, either "short" or "long", on each beat (known as concordant alternans). At faster rates or in much larger tissues, adjacent tissue regions with opposite phases can develop (discordant alternans)[67, 71, 88]. Further increases in the rate can produce conduction block[29, 71, 26], which often can subsequently develop into reentry and fibrillation[10].

At the scale of the entire heart, cellular alternans is believed to be manifested on the electrocardiogram as QRS and/or T-wave alternans[67, 88], although recent evidence suggests this association may not be complete[57]. It has been found that patients exhibiting even small T-wave alternans that is not visually apparent (microvolt T-wave alternans) are at a higher risk of developing ventricular arrhythmias [77], and a number of studies have led to the establishment of T-wave alternans as an important marker of susceptibility to sudden cardiac death [86]. Therefore, it would be desirable to have methods to suppress alternans when they develop in tissue, before they can evolve into fibrillation.

Several feedback control methods for the suppression of alternans and reentrant arrhythmias based on the application of external electrical stimuli of small intensity

have been proposed as methods for the prevention of VF. As of this time, however, none of these methods are close to the stage of development required for clinical implementation. Historically, the first schemes were based on time delay autosynchronization (TDAS) control. What makes these methods appealing is the ease of their implementation: the calculation of the timing and intensity of the control current is computationally inexpensive and no knowledge of the laws governing the system dynamics is required. In the context of cardiac tissue, TDAS was originally proposed as a way to suppress alternans by Rappel, Fenton, and Karma [72]. They investigated models of both 1D and 2D tissue and concluded that a grid of control electrodes was necessary to stabilize the normal heart rhythm (non-alternating time-periodic solution).

Echebarria and Karma [21] showed that alternans in paced short (about 1 cm) open Purkinje fibers (specialized quasi one dimensional conduction fibers located in the inner ventricular walls) could be suppressed using a single electrode. This is achieved by varying the pacing interval by an amount proportional to the difference between two successive APDs, which is conceptually similar to TDAS. Their findings were later verified experimentally by Christini *et al.* [11]. The experiments used 2 cm long canine Purkinje fibers paced at one of the ends. It was discovered that the variation of the pacing interval can indeed suppress small amplitude alternans but this approach will fail for alternans of large amplitude away from the location of the pacing electrode. Another experimental validation of this approach is provided by the study of Hall and Gauthier [35] which showed successful suppression of alternans in small pieces of bullfrog cardiac muscle. Although simple, pacing interval adjustment has a limitation of becoming ineffective at larger tissue sizes and large alternans amplitudes. As we will show in this thesis, this is due to the failure of this approach when there is more than one unstable mode.

More recently, several systematic control approaches have been developed which

use specific electrophysiological models to design the control algorithm. One such approach based on quasi-instantaneous suppression of the linearly unstable modes was proposed by Li and Otani [51] for single cells and by Allexandre and Otani [3] for two dimensional (2D) tissue. A significant limitation of this approach is that it is aimed at systems with only one pair of unstable modes. It is unclear whether (and how) it can be generalized to situations where multiple unstable modes coexist. Moreover, as we show in this work, it tends to produce conduction block for one dimensional (1D) tissue.

Dubljevic [18] and Dubljevic *et al.* [19] introduced a control method for 1D fibers based on the amplitude equation formalism [20]. Since the amplitude equation formalism is only valid when the action potential duration varies over distances much larger than the wavelength of the spatially periodic solution, the applicability of this approach to cardiac tissue of realistic dimensions is questionable. A canine Purkinje fiber (which is a few cm long), for instance, cannot fit even a single wavelength. For reference, the shortest wavelength of action potential can be estimated as the product of the minimum APD, 120 ms [48], and the minimum conduction velocity, 200 cm/s [16], or about 24 cm.

To address the limitations of these approaches, in this work we study the performance of standard control theoretic methods for linear time invariant systems [91, 17, 5]. The electrical activity in cardiac tissue is modeled by a set of nonlinear partial differential equations (PDE). We simplify the dynamics by linearizing the evolution equation around the state (target state) that the control method intends to stabilize. In this way we obtain a linear PDE that describes the dynamics of perturbations to the target state. This linear dynamics presents eigenmodes that decay or increase exponentially in the absence of control. By introducing a stroboscopic map from the linear evolution equation and projecting it onto a few of the eigenmodes (Galerkin projection) we obtain an approximation to the dynamics in terms

of a small number of modal amplitudes.

We consider one-dimensional models of cardiac tissue in two different geometries: a fiber with free ends (open fiber) and a ring. The open fiber is paced periodically at one end and simulates the propagation of a wave of excitation from the sinus node. On the other hand, the ring can sustain a traveling wave circulating around it without the need of periodic pacing. It serves as a model for reentrant waves.

In Chapter 2 we present the model equations of electrical activity in the heart together with a more detailed description of the state of alternans. In chapter 3 we perform the bifurcation analysis of the model PDE's to gain a better understanding of the onset of alternans. This analysis is one of the original contributions of this thesis. Chapter 4 is devoted to both non-model-based and model-based control. The non-model-based approach is not novel, hence the results are presented (Sect. 4.2) mainly for comparison purposes, as a reference. Sect. 4.3 covers the model-based control methods. This is the main original contribution of this thesis. In chapter 5 we discuss the implications of this work and the ways in which it could be extended. The numerical methods used are described in Appendix A.

CHAPTER II

MATHEMATICAL MODELS OF CARDIAC DYNAMICS

2.1 Introduction

The contraction of cardiac tissue cells is triggered by a wave of the transmembrane voltage (defined as the difference in electrical potential between the intracellular and extracellular spaces) that propagates through the tissue. The coupling between this excitation of the cell membrane and the cell's contractile machinery is mediated by a cycle of release and uptake of calcium from intracellular compartments. For a detailed treatment of the intracellular calcium dynamics see for instance [73]. In this chapter we present the general form of the models that describe the evolution of the transmembrane voltage. We then use these models to simulate two plausible experimental situations involving quasi-one dimensional strands of cardiac tissue. In the first, pulses are produced by stimulating periodically a fiber at one end. Experimental and theoretical studies of this arrangement have been carried out using Purkinje fibers [21, 11]. For the purpose of comparison with these studies, we use the Noble model [62]. In the second arrangement, a pulse is created and then allowed to travel indefinitely on a ring of tissue. Such a ring can be excised from the ventricular myocardium. To simulate this type of tissue with a low computational cost while at the same time retaining essential features of the dynamics, we use the 3-variable Fenton-Karma model [25]. For both geometries, we study how the asymptotic behavior of the model solutions varies in response to parameter changes. Even though we are using specific models and specific geometries, our approach is very general and can be extended in a straightforward manner to other models and geometries.

2.2 Model equations of cardiac electrical activity

In a one-dimensional strand of cardiac cells the evolution of the transmembrane voltage V is described by the cable equation [27]

$$\partial_t V = D\partial_x^2 V - (I_{\text{ion}} + I_{\text{ext}})/C_m, \tag{1}$$

where I_{ion} is the total membrane ionic current density, I_{ext} is an external current density, C_m is the membrane capacitance per unit area, and $D \equiv 1/(\rho S C_m)$ is the diffusion constant of the fiber that depends on the intracellular resistivity ρ and the cell surface to volume ratio S. I_{ion} depends on V and a set of *gate variables*, $\mathbf{n} = [n_1, n_2, ..., n_\zeta]$ determining the conductance of the ion channels

$$I_{\text{ion}} = I_{\text{ion}}(V, \mathbf{n}). \tag{2}$$

Each gate variable changes in time at a rate that typically is a function only of the gate variable itself and V,

$$\partial_t n_i = f_i(V, n_i), \qquad i = 1, ..., \zeta \tag{3}$$

The number of gate variables ζ and the functional forms of $I_{\text{ion}}(V, \mathbf{n})$ and $f_i(V, n_i)$ depend on the accuracy of the model and the type of cell studied.

While the gate variables take values between 0 and 1, the voltage V, when expressed in mV, can be of order 100. As this difference in the orders of magnitude of V and the gate variables can bring about instabilities in the numerical methods, it is convenient to work with a scaled voltage u rather than with V,

$$u = \frac{V - V_{\text{off}}}{V_{\text{sc}}} \tag{4}$$

where V_{off} and V_{sc} are chosen so that u takes values mostly in the range [0,1]. For the sake of simplicity we also define the scaled current densities j,

$$j = \frac{I}{C_m V_{\text{sc}}}. \tag{5}$$

Using the scaled variables, equations (1) and (3) can be written in compact form as

$$\partial_t \mathbf{z} = \widetilde{D}\partial_x^2 \mathbf{z} + F(\mathbf{z}) - \mathbf{j}_{\text{ext}}, \tag{6}$$

where the state variable $\mathbf{z}(x,t) = [u(x,t), n_1(x,t), ..., n_\zeta(x,t)]^{\mathcal{T}}$ (the superscript $\mathcal{T}$ denotes matrix transposition, such that $\mathbf{z}$ is a column vector), $\widetilde{D}$ is a $(\zeta+1)\times(\zeta+1)$ matrix whose only nonzero entry is $\widetilde{D}_{11} = D$, $F(\mathbf{z}) = [j_{\text{ion}}(u,\mathbf{n}), f_1(u,n_1), ..., f_\zeta(u,n_\zeta)]^{\mathcal{T}}$ and

$$\mathbf{j}_{\text{ext}} = [j_{\text{ext}}(x,t), 0, ..., 0]^{\mathcal{T}}, \tag{7}$$

where $j_{\text{ext}}(x,t)$ is the scaled external current density.

2.2.1 Electrodes

In typical experiments with Purkinje fibers microelectrodes are used to record voltages and apply currents. To properly account for the effect of extracellular stimulation one should use a bidomain model which incorporates electrical conduction in both the cellular and the extracellular medium. Without going into the details, numerical simulations of bidomain models show that even a point-like current injection in the extracellular medium produces a pattern of transmembrane polarization of finite spatial extent (see e.g. Ref.[85, 78]). The corresponding current density $j_{\text{ext}}(x,t)$ is typically a narrow function of spatial variables with a maximum at the electrode location. As the exact shape of this distribution is not expected to be of relevance, we assume it to be Gaussian. We also assume the spatial profile of $j_{\text{ext}}(x,t)$ to be independent of the magnitude of the net current injected through the electrode. Thus for a single electrode we assume

$$j_{\text{ext}}(x,t) = \mathcal{I}(t) g(x - x_0), \tag{8}$$

where $\mathcal{I}(t)$ is proportional to the current (the surface integral of the current density), x_0 is the electrode location and $g(x)$ is a normalized Gaussian,

$$g(x) = \frac{2}{\omega}\sqrt{\frac{\ln 2}{\pi}} \exp\left[-\left(\frac{x}{\omega/2}\right)^2 \ln 2\right], \tag{9}$$

$$\int_{-\infty}^{\infty} g(x)dx = 1,$$

where the full width ω at half the maximum is much less than the fiber length L. For several electrodes $j_{\text{ext}}(x,t)$ is a superposition of terms of the form (8). Expressions (7) and (8) can be combined conveniently as

$$\mathbf{j}_{\text{ext}} = \mathcal{I}(t)\mathbf{g}(x - x_0), \tag{10}$$

where $\mathbf{g}(x - x_0) = [g(x - x_0), 0, ..., 0]^{\mathcal{T}}$.

It is worthwhile to discuss the units of $\mathcal{I}(t)$. By transforming (8) to physical units with the help of (5) we obtain

$$I_{\text{ext}} = \widetilde{\mathcal{I}}(t)g(x - x_0), \tag{11}$$

where $\widetilde{\mathcal{I}}(t)$ is $\mathcal{I}(t)$ expressed in physical units. I_{ext} has dimensions of current (ampere) over area (m^2) and $g(x - x_0)$ has dimensions of inverse of length (m^{-1}). Therefore, $\widetilde{\mathcal{I}}(t)$ must have dimensions of current over length (A/m). Hence, $\widetilde{\mathcal{I}}(t)$ can be thought of as the current injected by the electrode divided by the width of the cross section of the fiber. Notwithstanding this difference, we will continue referring to $\mathcal{I}(t)$ as the *current*.

2.2.2 Pacing and control currents

In this work external currents are used for two purposes. One is to create traveling waves in the tissue. In this case, the current is strong enough to exceed the threshold of excitability of the cell membrane (a current of 50 $\mu\text{A/cm}^2$ applied during 5 ms, for instance). The other purpose is to control the dynamics. In this case, the current is usually small as it must not drive the dynamics away from the linear regime for which the control protocols are designed. We call the first type of external current the *pacing current* $\mathbf{j}_p$ (we will sometimes refer to current densities as *currents*) and the second one the *control current* $\mathbf{j}_c$. In general the net external current is a superposition of

both types

$$\mathbf{j}_{\text{ext}} = \mathbf{j}_p + \mathbf{j}_c. \tag{12}$$

2.3 Alternans in an open fiber

Consider a fiber of length L, paced by an electrode at position x_p. The initial studies of this system were done by Echebarria and Karma [20, 21]. While in Ref. [21] the pacing electrode is located exactly at the left end ($x_p = 0$) we used $x_p = 0.25$ cm. The location $x_p = 0$ was avoided on the assumption that in an experimental setting it might be difficult to achieve proper electrical contact between the fiber end and the electrode. We will see that this difference in x_p does not introduce any significant discrepancy between our results and those of Ref. [21].

The electrode injects a pacing current $j_p(x,t)$,

$$j_p(x,t) = \mathcal{I}_p(t) g(x - x_p), \tag{13}$$

with $\mathcal{I}_p(t)$ consisting of a sequence of brief pulses applied at times $t_n = nT, \quad n = 0, 1, 2, ...$, with a constant pacing period T,

$$\mathcal{I}_p(t) = \begin{cases} a & 0 < t < \Delta \\ 0 & \Delta < t < T \end{cases}, \tag{14a}$$

$$\mathcal{I}_p(t+T) = \mathcal{I}_p(t), \tag{14b}$$

where a is the pulse strength and Δ is the pulse duration. Each pulse (pacing stimulus) produces a traveling wave of action potential that propagates toward the right end as well as the left. Following [21] we use no flux boundary conditions at both ends $\partial_x u|_{x=0,L} = 0$. These boundary conditions cause the right end to absorb (rather than reflect) the arriving excitation waves, a behavior that is observed in experiments. Physically, they correspond to an intracellular current that vanishes at each end (see reference [27] for details).

In order to compare our results with those of Echebarria and Karma [21] we used the Noble model [62] for the ionic current $I_{\rm ion}$,

$$I_{\rm ion} = I_{\rm Na} + I_{\rm K} + I_{\rm An}, \tag{15}$$

where $I_{\rm Na}, I_{\rm K}$ are the sodium and potassium ionic currents respectively and $I_{\rm An}$ is the anion current (an important deficiency of the Noble model, formulated in 1962, is the absence of calcium currents, not demonstrated until 1967 [28, 74]). Following Echebarria and Karma (internal communication), we set $I_{\rm An} = 0$. For the remaining ionic currents

$$I_{\rm Na} = g_{\rm Na}(V - E_{\rm Na}), \tag{16}$$

$$I_{\rm K} = g_{\rm K}(V - E_{\rm K}), \tag{17}$$

where $g_{\rm Na}$ and $g_{\rm K}$ are the sodium and potassium conductances respectively and $E_{\rm Na} = 40$ mV and $E_{\rm K} = -100$ mV are the equilibrium potentials. The sodium conductance is given by

$$g_{\rm Na} = (400 n_1^3 n_2 + 0.014) \text{ mmho/cm}^2, \tag{18}$$

where n_1 and n_2 are gate variables. The potassium conductance corresponds to

$$g_{\rm K} = g_{\rm K1} + g_{\rm K2} \tag{19}$$

$$g_{\rm K1} = 1.2 \exp[(-V - 90)/50] + 0.015 \exp[(V + 90)/60] \tag{20}$$

$$g_{\rm K2} = 1.2 n_3^4, \tag{21}$$

where n_3 is a gate variable (the units of conductances, mmho/cm^2, and voltages, mV, have been omitted for the sake of simplicity). The dynamics of all gate variables is given by

$$\partial_t n_i = \alpha_i(1 - n_i) - \beta_i n_i, \qquad i = 1, 2, 3, \tag{22}$$

with coefficients α_i, β_i,

$$\alpha_1 = \frac{0.1(-V-48)}{\exp[(-V-48)/15]-1}, \tag{23}$$

$$\beta_1 = \frac{0.12(V+8)}{\exp[(V+8)/5]-1}, \tag{24}$$

$$\alpha_2 = 0.17\exp[(-V-90)/20], \tag{25}$$

$$\beta_2 = \left[\exp\left(\frac{-V-42}{10}\right)+1\right]^{-1}, \tag{26}$$

$$\alpha_3 = \frac{0.0001(-V-50)}{\exp[(-V-50)/10]-1}, \tag{27}$$

$$\beta_3 = 0.002\exp[(-V-90)/80]. \tag{28}$$

We simulated the generation and propagation of action potentials by integrating (6) in time using explicit Euler time stepping. Finite difference approximation was used for the diffusion term. Fig. 1 shows the computed voltage u as a function of position at a fixed time. Fig. 2 shows u at a fixed location as a function of time for several pacing intervals. Action potentials present a sharp front corresponding to a fast increase of u from its rest value (depolarization) followed by smooth tail corresponding to a slow return of u to this value (repolarization). The action potential duration (APD) at a given location is defined as the time that lapses between the instant u surpasses a threshold value u_{th} during depolarization and the instant it falls below that value during repolarization (Fig. 2). The APD therefore is associated with a particular position x and a particular pacing stimulus n. We indicate this dependence with the notation $\text{APD}_n(x)$. When a fiber is paced over a long time interval, it is observed that after a transient period during which the dynamics depends on the initial conditions, $\text{APD}_n(x)$ approaches an asymptotic regime. Two distinct asymptotic regimes are observed. When T is bigger than some critical value T_c, $\text{APD}_n(x)$ is constant from beat to beat, $\text{APD}_n(x) = \text{APD}(x)$. This is the normal (or 1:1) rhythm.

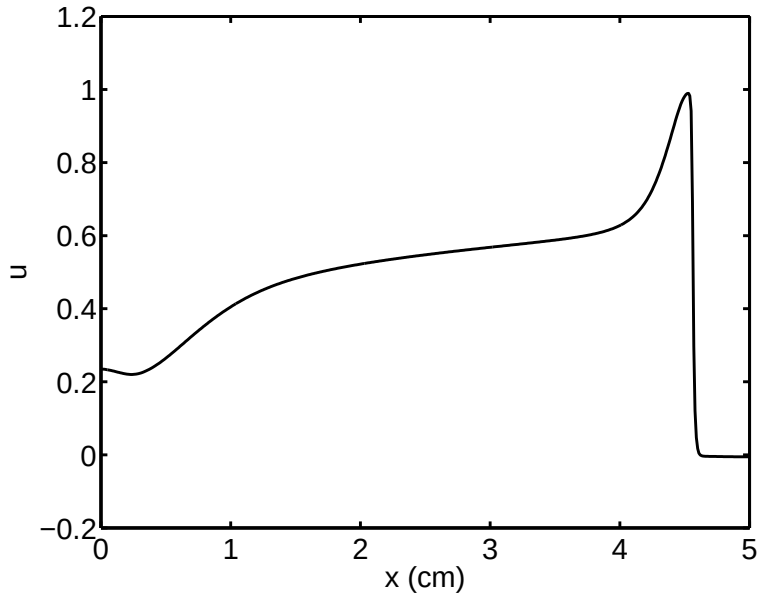

Figure 1: Normal rhythm: transmembrane potential $u(x,t)$ at $t = 0.7T$. The parameters are $L = 5$ cm and $T = 270$ ms.

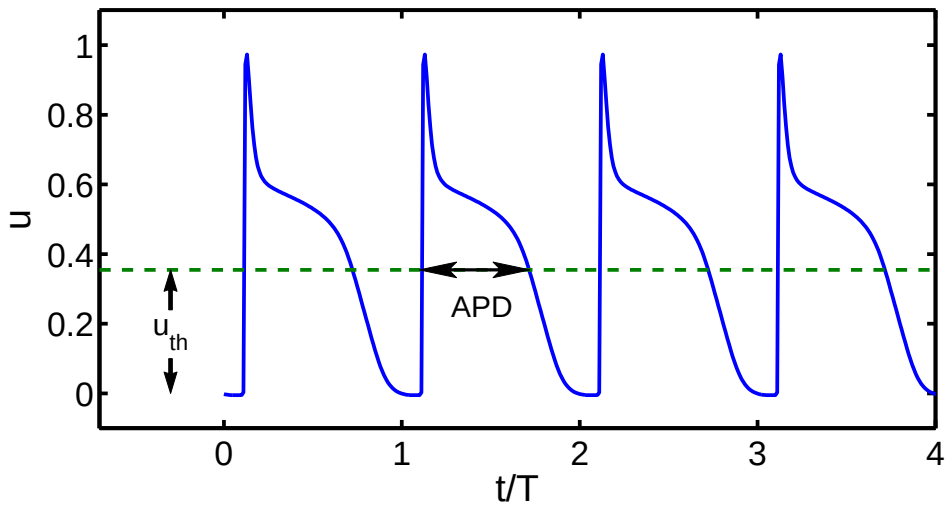

Figure 2: Normal rhythm: transmembrane potential $u(x,t)$ at $x = 1$ cm. The parameters are $L = 5$ cm and $T = 270$ ms.

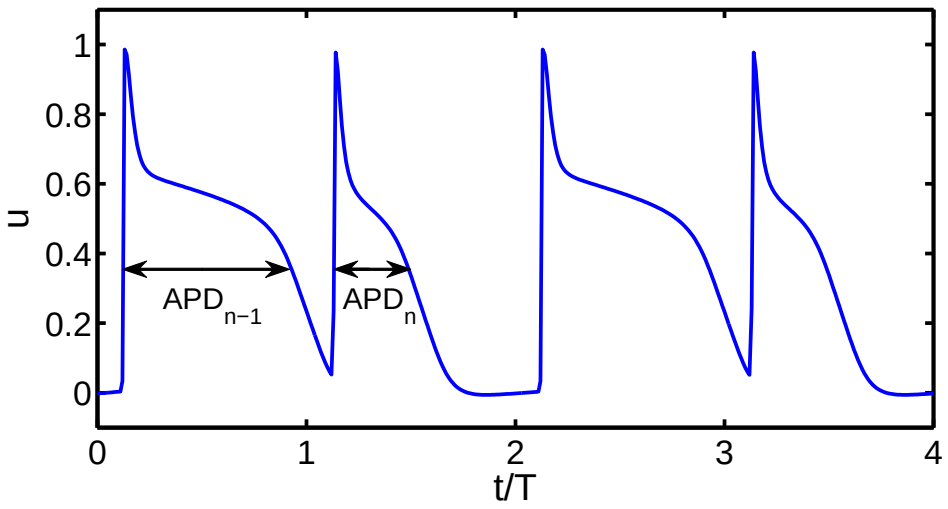

Figure 3: Alternans: transmembrane potential $u(x,t)$ at $x = 1$ cm. The parameters are $L = 5$ cm and $T = 250$ ms.

When T is less than T_c, $\mathrm{APD}_n(x)$ alternates between long and short from beat to beat. That is, $\mathrm{APD}_{n+1}(x) \neq \mathrm{APD}_n(x)$ for most x-values but $\mathrm{APD}_{n+2}(x) = \mathrm{APD}_n(x)$ for all x. This second regime is known as the state of alternans (or 2:2) rhythm. Fig. 3 shows u as a function of time in this regime. The onset of the state of alternans when the pacing rate is increased is a well known fact in both experiments and simulations [63, 33, 67, 71, 88].

Alternans could be *concordant*, if $\mathrm{APD}_{n+1}(x) - \mathrm{APD}_n(x)$ has the same sign for all x (Fig. 4) or *discordant* if it does not (Fig. 5). A typical feature of discordant alternans is the presence of nodes, i. e. spatial locations x for which $\mathrm{APD}_{n+1}(x) - \mathrm{APD}_n(x) = 0$.

Figs. 6 and 7 offer a different perspective on the state of alternans. They show u as a function of space and time for the normal state (Fig. 6) and the state of alternans (Fig. 7). Note that in the state of alternans the shape of the action potential oscillates as it propagates, while in the normal rhythm it stays nearly constant. A similar behavior to that is exhibited by an action potential circulating on a ring (Figs. 8 and 10), as we will show below.

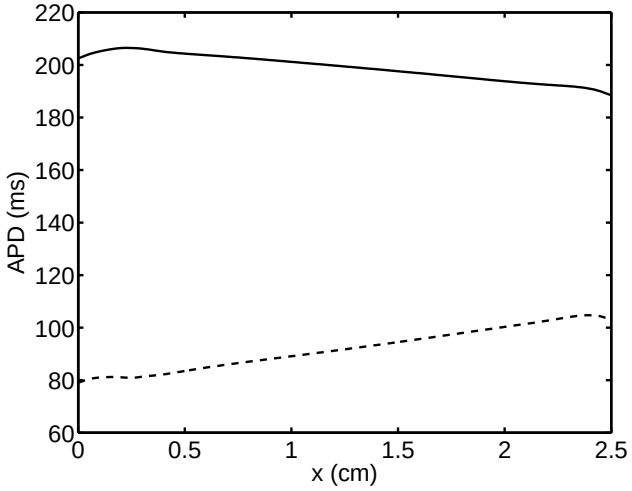

Figure 4: Concordant alternans: $\mathrm{APD}_n(x)$ following odd (solid line) and even (dashed line) pacing stimuli. The parameters are $L = 2.5$ cm and $T = 250$ ms.

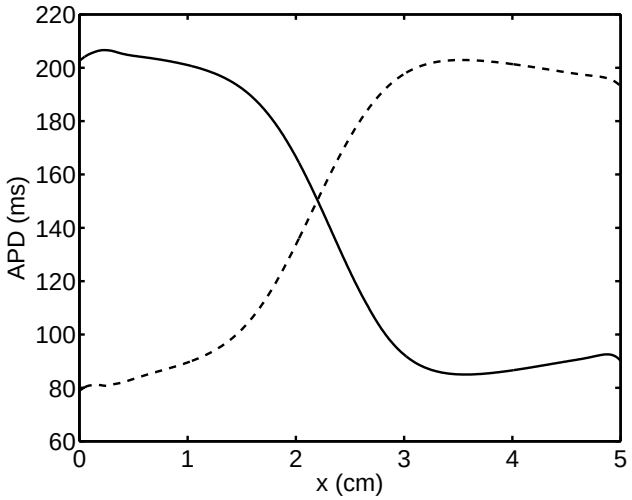

Figure 5: Discordant alternans: $\mathrm{APD}_n(x)$ following odd (solid line) and even (dashed line) pacing stimuli. The parameters are $L = 5$ cm and $T = 250$ ms.

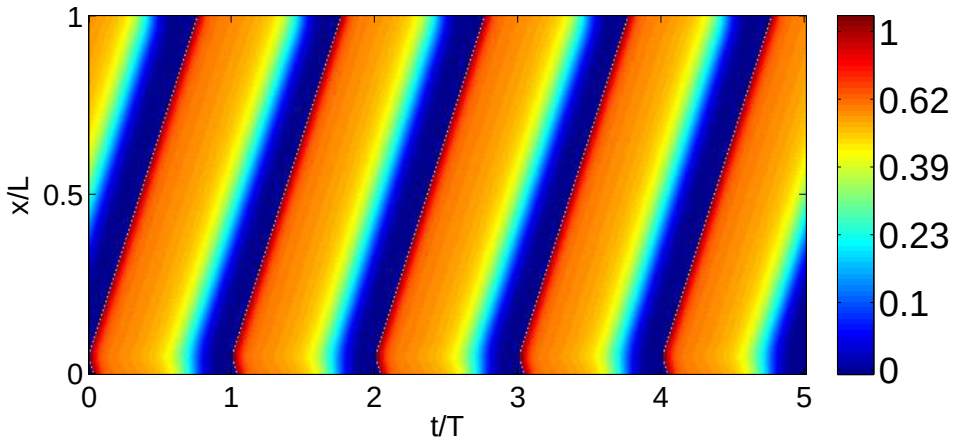

Figure 6: (color) $u(x,t)$ during normal rhythm ($L = 5$ cm, $T = 270$ ms).

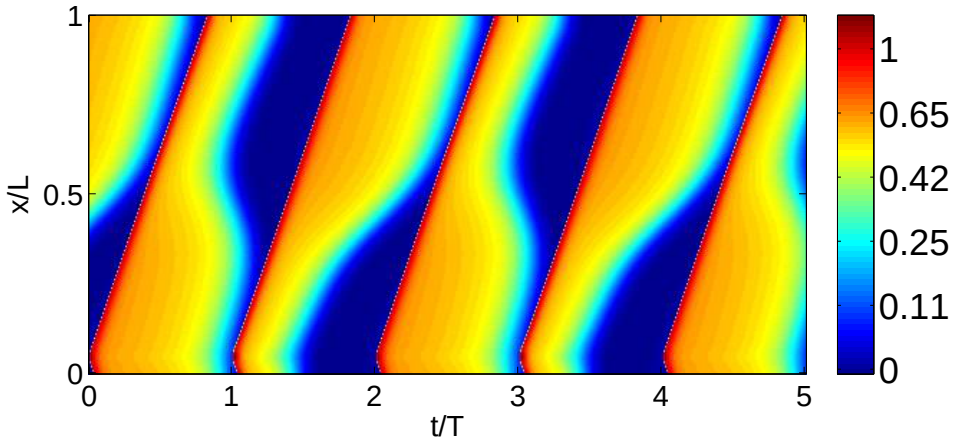

Figure 7: (color) $u(x,t)$ during alternans ($L = 5$ cm, $T = 250$ ms).

2.4 Alternans in a ring geometry

In a ring of excitable cardiac tissue an action potential can circulate indefinitely (as long as the tissue's physiological conditions are maintained) without the need of an external current to sustain it. Thus a ring can serve as a model for the study of reentrant waves. For instance, functional reentry is often associated with a spiral wave. Away from the tip, each segment of the spiral wave can be thought of as a traveling wave on a ring. Therefore, although the spiral wave dynamics in 2D is richer, some of the results obtained in the 1D ring geometry might be of relevance to spiral wave dynamics.

The ring geometry is accounted for by the periodic boundary conditions: $\mathbf{z}(0,t) = \mathbf{z}(L,t)$ for all t, where L is the ring length (circumference). We set $D = 1.171 \times 10^{-3}$ cm^2/ms [6]. For the ring geometry we used a slightly modified version of the 3-variable Fenton-Karma model [25] for the scaled ionic current $j_{\rm ion}$ in the dynamical equation (6),

$$j_{\rm ion} = j_{\rm fi} + j_{\rm so} + j_{\rm si}, \tag{29}$$

where $j_{\rm fi}$ is a fast inward current, $j_{\rm so}$ is a slow outward current and and $j_{\rm si}$ is a slow inward current (for a discussion of the correspondence between these currents and Na, K and Ca currents see Ref. [25]). In the original Fenton-Karma model the currents are given by

$$J_{\rm fi}(u,n_1) = -\frac{n_1}{\tau_d}\Theta(u-u_c)(1-u)(u-u_c), \tag{30}$$

$$J_{\rm so}(u) = \frac{u}{\tau_o}\Theta(u_c-u) + \frac{1}{\tau_r}\Theta(u-u_c), \tag{31}$$

$$j_{\rm si}(u,n_2) = -\frac{n_2}{2\tau_{\rm si}}(1+\tanh[\kappa(u-u_c^{\rm si})]),$$

where $\Theta(s)$ is the Heaviside step function

$$\Theta(s) = \begin{cases} 1, & s \geq 0 \\ 0, & s < 0 \end{cases}$$

and n_1 and n_2 are gate variables with dynamics governed by

$$\partial_t n_1 = \Theta(u_c - u)(1 - n_1)/\tau_v^-(u) - \Theta(u - u_c)n_1/\tau_v^+ \tag{32}$$

$$\partial_t n_2 = \Theta(u_c - u)(1 - n_2)/\tau_w^- - \Theta(u - u_c)n_2/\tau_w^+, \tag{33}$$

where

$$\tau_v^-(u) = \Theta(u - u_v)\tau_{v1}^- + \Theta(u_v - u)\tau_{v2}^-. \tag{34}$$

Except where stated otherwise, we set the parameters τ_d, u_c, τ_o, τ_r, $\tau_{\rm si}$, κ, $u_c^{\rm si}$, τ_{v1}^-, τ_{v2}^-, τ_v^+, τ_w^- and τ_w^+ to the values in Table 1 of Ref. [25] (column labeled MBR). The gate variables n_1 and n_2 will also be referred to as variables v and w respectively. Note that the right hand sides of equations (30) to (34) are particular instances of the step function $\Phi(u;\chi) = a(u)\Theta(u-\chi) + b(u)\Theta(\chi - u)$. For the dynamical reduction used in chapters 3 and 4, we will need the derivative with respect to u of the ionic current $j_{\rm ion}$ and the time rate of change of the gate variables [the right hand sides of equations (32) and (33)]. Given that $d\Phi/du$ is not defined at $u = \chi$, we substituted $\Phi(u;\chi)$ in all instances by its smoothed analogue

$$\widetilde{\Phi}(u;\chi) = \frac{1}{2}\left\{(a+b) + (b-a)\tanh\left[(u-\chi)/\iota\right]\right\}$$

with $\iota = 0.03$.

We generated action potentials on rings of different lengths with a current density applied by two electrodes of opposite polarity (bipolar current) located at $x_0 + d$ and $x_0 - d$, $d \ll L$ but $d > \omega$,

$$j_p(x,t) = \mathcal{I}_p(t)\{g[s(\tilde{x} - d)] - g[s(\tilde{x} + d)]\} \tag{35}$$

where $\tilde{x} = x - x_0$ and the shift function $s(x) = [(x + L/2) \bmod L] - L/2$ takes into account the periodic boundary conditions. This spatial distribution is not invariant under the inversion $\tilde{x} \to -\tilde{x}$. The lack of this symmetry is necessary as the current density must choose between the two possible directions of propagation on the ring.

The current $\mathcal{I}_p(t)$ is kept constant and then turned off after the action potential is created. For values of L above the critical value $L_c = 10.03$ cm, the action potential approaches asymptotically a traveling wave solution $\tilde{\mathbf{z}}(x,t)$ that propagates on the ring with constant speed c and constant shape $\mathbf{z}_p(x)$,

$$\tilde{\mathbf{z}}(x,t) = \mathbf{z}_p(x - ct). \tag{36}$$

This traveling wave solution has periods L and $T = L/c$ in space and time, respectively, and represents the normal rhythm.

The evolution of the action potential is most conveniently represented in a reference frame that moves along the ring with speed c (co-moving reference frame). The coordinates in the co-moving reference frame (primed) are related to the stationary reference frame coordinates (unprimed) by

$$x' = (x - ct) \bmod L \tag{37a}$$

$$t' = t \tag{37b}$$

By applying the chain rule to the spatial and temporal derivatives of the evolution equation in the fixed reference frame (6),

$$\partial_t \mathbf{z} = \frac{\partial \mathbf{z}}{\partial t} = \frac{\partial \mathbf{z}}{\partial t'}\frac{\partial t'}{\partial t} + \frac{\partial \mathbf{z}}{\partial x'}\frac{\partial x'}{\partial t}, \tag{38}$$

$$\partial_x \mathbf{z} = \frac{\partial \mathbf{z}}{\partial x} = \frac{\partial \mathbf{z}}{\partial t'}\frac{\partial t'}{\partial x} + \frac{\partial \mathbf{z}}{\partial x'}\frac{\partial x'}{\partial x}, \tag{39}$$

we obtain the evolution equation in the co-moving reference frame,

$$\partial_{t'} \mathbf{z} = c\partial_{x'} \mathbf{z} + \widetilde{D}\partial_{x'}^2 \mathbf{z} + F[\mathbf{z}] - \mathbf{j}'_{\text{ext}}, \tag{40}$$

where $\mathbf{j}'_{\text{ext}} = [j'_{\text{ext}}(x',t'), 0, ..., 0]^{\mathcal{T}}$ with $j'_{\text{ext}}(x',t') \equiv j_{\text{ext}}[(x'+ct') \bmod L, t']$ the external current density transformed to the co-moving reference frame. To simplify the notation we will drop the primes. When necessary, we will state whether the unprimed coordinates correspond to the fixed or the co-moving reference frame.

To visualize the dynamics in the co-moving reference frame one has two options. One is to integrate the evolution equation (6) in the fixed reference frame and then transform the solution to the co-moving reference frame using (37). The other is to directly integrate Eq. (40). As will be clear later, this second option is more convenient for the study of model-based control. For consistency we used it here also. The numerical method used is discussed in Sect. A.1.

In the co-moving frame, after a short transient, the traveling wave solution (36) becomes stationary for $L > L_c$, as Fig. 8 illustrates. We therefore choose the co-moving reference frame to present all the results for the ring geometry.

For $L < L_c$, the system state asymptotically approaches a limit cycle characterized by oscillation of the AP width (in the co-moving frame). An example, as observed in the co-moving reference frame, is shown in Fig. 10. This solution, which is time-periodic in the co-moving reference frame, will appear as quasi-periodic in the stationary reference frame since the frequency with which the pulse propagates around the ring is generally incommensurate with the frequency with which its width oscillates. This is consistent with the results of Courtemanche *et al.* [13] and Comtois and Vinet [12].

We will call the stationary solution ($L > L_c$) the *normal rhythm* and the oscillatory one ($L < L_c$) the *state of alternans*. The correspondence between these definitions and the more traditional ones in terms of the APD (introduced in the previous section) is discussed next.

2.5 Conclusion

Despite the differences in the ionic models used, the observed transition between stationary and oscillatory solutions on a ring is qualitatively similar to the transition between normal rhythm and alternans in an open fiber. The similarity holds in several ways. First, as Figs. 6 and 7 show, in the open fiber the shape of the AP is constant

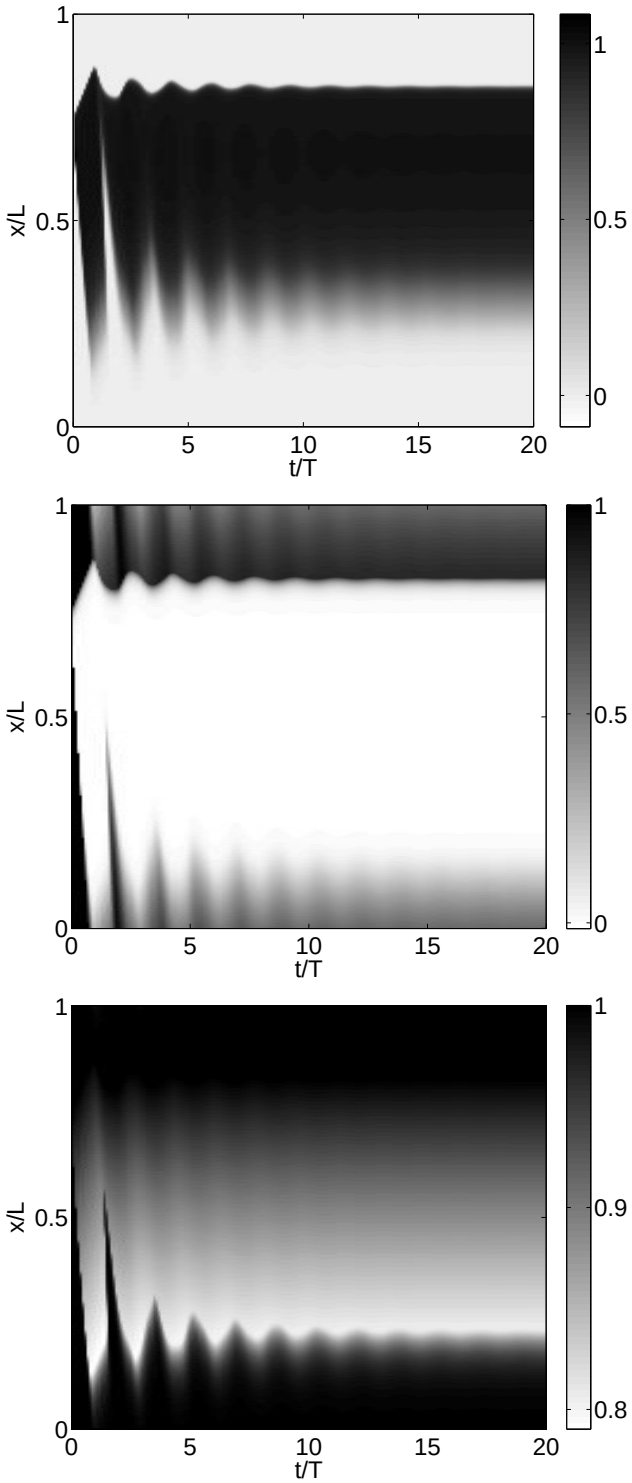

Figure 8: Evolution of the transmembrane voltage u (top) and the gate variables v (middle) and w (bottom) on a ring of length $L = 10.57$ cm. For aid in the interpretation of this figure see Fig. 9. Here and everywhere below the spatial position x refers to the *co-moving* reference frame.

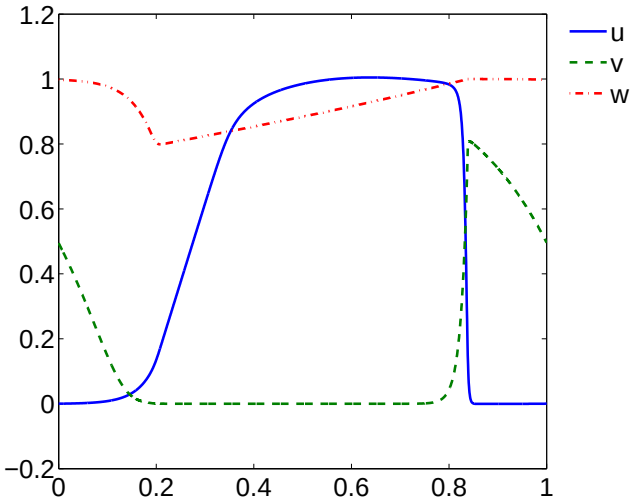

Figure 9: Voltage u and gate variables v and w from Fig. 8 for $t = 4.5T$.

(away from the boundaries) during the normal rhythm while it oscillates in the state of alternans. Second, when the voltage is recorded at a fixed location on the ring, the oscillations of the pulse shape appear as a beat-to-beat alternations of the APD (Fig. 11) which is the defining feature of the state of alternans in the open fiber (see Fig. 3). Finally, the increase of the pacing period in the open fiber is analogous to the reduction of length in the ring. A long enough open fiber can sustain a train of APs with a characteristic wavelength defined as the distance between two consecutive APs. Since the AP propagation speed (conduction velocity) does not vary significantly, the increase in the pacing rate is equivalent to a decrease in the wavelength. For the ring, the wavelength is the same as the ring length; therefore, we can identify the limit cycle oscillation of the pulse width with the state of alternans and the steady state with the normal rhythm.

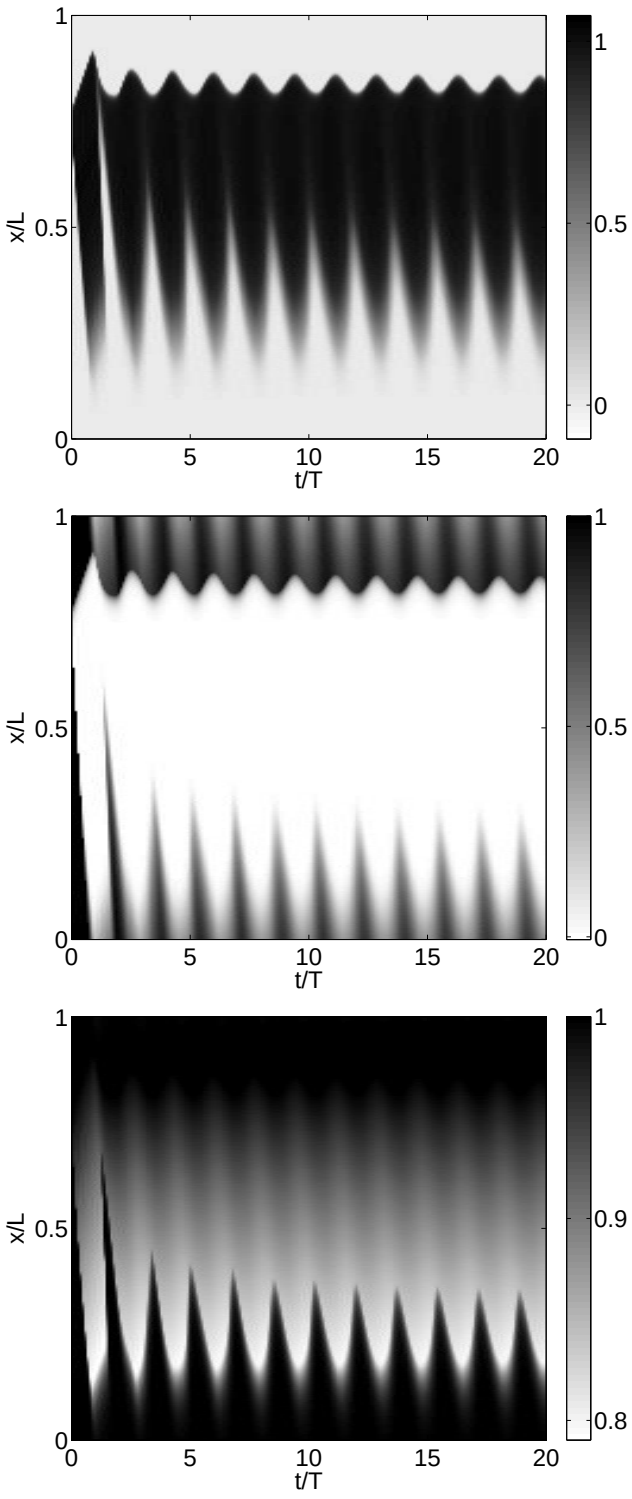

Figure 10: Evolution of the transmembrane voltage u (top) and the gate variables v (middle) and w (bottom) on a ring of length $L = 9.94$ cm. The asymptotic state corresponds to fully developed alternans.

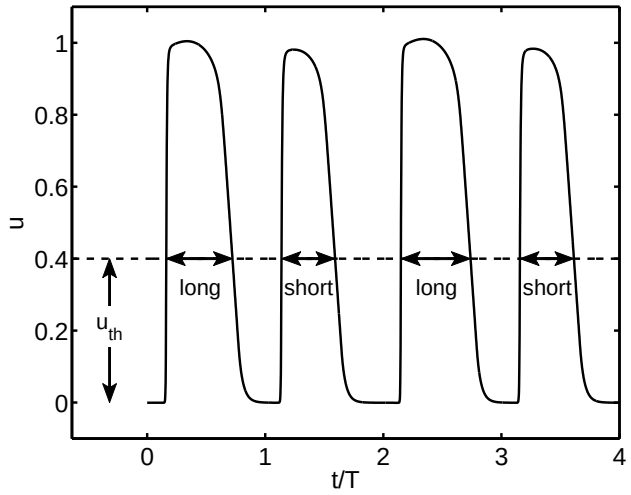

Figure 11: Transmembrane voltage at a fixed location on a ring of length $L = 9.94$ cm. One can see a pattern of alternation between long and short APD, characteristic of alternans.

CHAPTER III

BIFURCATION ANALYSIS

3.1 Introduction

More insight into the transition from the normal rhythm to the state of alternans can be gained by performing bifurcation analysis of the evolution equation. Although bifurcation analysis of the Fenton-Karma model and the Noble model has been performed previously for single cells, their dynamics are described by ordinary differential equations [84, 43, 87], so the results cannot be easily generalized for the 1D tissue considered here.

Bifurcation analysis has several stages. The first one is the identification of simple (e.g. stationary or fixed point) solutions of the dynamical equations. For instance, for the ring geometry, the normal rhythm is a fixed point of the dynamics in the co-moving reference frame. For the open fiber, the normal rhythm is a periodic orbit, which is to say, a fixed point of the evolution operator that evolves the system state on time intervals of duration T (stroboscopic map). The second step of the bifurcation analysis is linear stability analysis of the fixed points. In this step, we express a perturbation to the fixed point as a linear superposition of the eigenmodes of the evolution operator. We then study the dynamics of the superposition coefficients (modal amplitudes). For small perturbations and in the absence of control currents, the modal amplitudes have trivial dynamics: they grow (unstable modes) or decay (stable modes) exponentially, independently of each other. As we will show below, for both the open fiber and the ring, the transition to the state of alternans occurs when the normal rhythm becomes linearly unstable.

3.2 Modal decomposition and linear stability analysis

In this section we derive a description of the dynamics of perturbations in terms of the modal amplitudes. As a first step we obtain the evolution equation of perturbations in the linear approximation. We then define the modes in relation to this linear evolution equation. Finally, we express the perturbation as a superposition of modes and obtain the evolution equation for the modal amplitudes. As noted above, the normal rhythm is a stationary (periodic) solution of the evolution equation for the ring (open fiber). This difference demands that the two cases be given separate treatments.

3.2.1 Ring geometry

We start by writing the dynamical equation (40) in compact form as

$$\partial_t \mathbf{z} = \mathcal{N}[\mathbf{z}] - \mathbf{j}_c \tag{41}$$

where

$$\mathcal{N}[\mathbf{z}] = \widetilde{D}\partial_x^2 \mathbf{z} + c\partial_x \mathbf{z} + F[\mathbf{z}] - \mathbf{j}_p. \tag{42}$$

To understand the stability of the normal rhythm $\mathbf{z}_p$ we focus on the dynamics of small perturbations $\delta\mathbf{z} = \mathbf{z} - \mathbf{z}_p$ where

$$\partial_t \mathbf{z}_p = \mathcal{N}[\mathbf{z}_p]. \tag{43}$$

Substituting $\mathbf{z} = \mathbf{z}_p + \delta\mathbf{z}$ into (56) and subtracting (43) from the resulting equation we get

$$\partial_t \delta\mathbf{z} = \mathcal{N}[\mathbf{z}_p + \delta\mathbf{z}] - \mathcal{N}[\mathbf{z}_p] - \mathbf{j}_c. \tag{44}$$

If the perturbation $\delta\mathbf{z}$ is small enough, $\mathcal{N}[\mathbf{z}_p + \delta\mathbf{z}]$ can be approximated by the first two terms of the Taylor series expansion

$$\mathcal{N}[\mathbf{z}_p + \delta\mathbf{z}] \approx \mathcal{N}[\mathbf{z}_p] + J_{\mathcal{N}}|_{\mathbf{z}_p}\, \delta\mathbf{z}, \tag{45}$$

where $J_{\mathcal{N}}|_{\mathbf{z}_p}$ is the Jacobian of $\mathcal{N}$ evaluated at $\mathbf{z}_p$

$$J_{\mathcal{N}} = \widetilde{D}\partial_x^2 + c\partial_x + J_F|_{\mathbf{z}_p} \tag{46}$$

with $J_F|_{\mathbf{z}_p}$ the Jacobian of F, $(J_F)_{ij} = \partial F_i/\partial z_j$. Note that since $\mathbf{z}_p$ is stationary, $J_\mathcal{N}$ is a time independent operator. Substituting (45) into (44), we obtain a linear evolution equation for $\delta\mathbf{z}$,

$$\partial_t \delta\mathbf{z} \approx J_\mathcal{N}\delta\mathbf{z} - \mathbf{j}_c. \tag{47}$$

Let us define the eigenfunctions $\mathbf{e}_i$ and eigenvalues μ_i of $J_\mathcal{N}$

$$J_\mathcal{N}\mathbf{e}_i = \mu_i\mathbf{e}_i. \tag{48}$$

It is possible to further simplify the dynamics of perturbations by expressing $\delta\mathbf{z}(t)$ as a linear combination of the eigenfunctions $\mathbf{e}_i$,

$$\delta\mathbf{z}(t) = \sum_{i=1}^{\infty} \xi_i(t)\mathbf{e}_i. \tag{49}$$

Then, through a Galerkin projection of (47) one can obtain an evolution equation for the coefficients $\xi_i(t)$ (modal amplitudes). The notion of projection of a function onto another is formalized by the introduction of an inner product. With the definition of an inner product, the space of functions becomes a Hilbert space [44, 39]. Throughout this work, we use the inner product $\langle\cdot,\cdot\rangle$ between two functions, $\delta\mathbf{z}'$, $\delta\mathbf{z}''$, defined by

$$\langle\delta\mathbf{z}', \delta\mathbf{z}''\rangle = \sum_{i=1}^{\zeta+1} \int_0^L \delta z_i'^*(x)\delta z_i''(x)dx, \tag{50}$$

where the asterisk denotes complex conjugation. The definition of the inner product generates the definition of the adjoint of a linear operator. For a linear operator $\mathcal{L}$, for instance $J_\mathcal{N}$, the adjoint, $\mathcal{L}^\dagger$, is defined by

$$\langle\mathcal{L}\delta\mathbf{z}', \delta\mathbf{z}''\rangle = \left\langle\delta\mathbf{z}', \mathcal{L}^\dagger\delta\mathbf{z}''\right\rangle, \tag{51}$$

for all $\delta\mathbf{z}'$ and $\delta\mathbf{z}''$. Let $\mathbf{f}_i$ denote the eigenfunctions of $J_\mathcal{N}^\dagger$,

$$J_\mathcal{N}^\dagger\mathbf{f}_i = \mu_i^*\mathbf{f}_i. \tag{52}$$

With the appropriate normalization, the eigenfunction $\mathbf{f}_i$ and $\mathbf{e}_i$ satisfy the biorthogonality condition

$$\langle\mathbf{e}_i, \mathbf{f}_j\rangle = \delta_{ij}. \tag{53}$$

Substituting (49) into (47) and applying the operation $\langle \mathbf{f}_j, \cdot \rangle$ to each side of the resulting equation we obtain

$$\dot{\xi}_i = \mu_i \xi_i - \langle \mathbf{f}_i, \mathbf{j}_c(t) \rangle \,. \tag{54}$$

From (54) we see that the spontaneous ($\mathbf{j}_c(t) = 0$) evolution of the modal amplitudes $\xi_i(t)$ is given by

$$\xi_i(t) = \exp(\mu_i t)\xi_i(0). \tag{55}$$

Therefore, the normal rhythm will be unstable if $\mathrm{Re}(\mu_i) > 0$ for at least one eigenmode.

3.2.2 Open fiber

The dynamical equation (6) can be written in compact form as

$$\partial_t \mathbf{z} = \mathcal{N}[\mathbf{z}] - \mathbf{j}_c \tag{56}$$

where

$$\mathcal{N}[\mathbf{z}] = \widetilde{D}\partial_x^2 \mathbf{z} + F[\mathbf{z}] - \mathbf{j}_p. \tag{57}$$

Following steps similar to those in the previous section, we obtain a linear evolution equation for perturbations $\delta\mathbf{z} = \mathbf{z} - \mathbf{z}_p(t)$ to the time-dependent normal rhythm $\mathbf{z}_p(t)$ in the fixed reference frame,

$$\partial_t \delta\mathbf{z} \approx J_{\mathcal{N}}(t)\, \delta\mathbf{z} - \mathbf{j}_c, \tag{58}$$

where $J_{\mathcal{N}}(t)$ is the Jacobian of $\mathcal{N}$ evaluated at $\mathbf{z}_p(t)$,

$$J_{\mathcal{N}}(t) = \widetilde{D}\partial_x^2 + J_F|_{\mathbf{z}_p(t)} \tag{59}$$

with $J_F|_{\mathbf{z}_p(t)}$ the Jacobian of F, $(J_F)_{ij} = \partial F_i/\partial z_j$. $J_{\mathcal{N}}(t)$ is a time-dependent operator with period T as a consequence of the time-periodicity of $\mathbf{z}_p(t)$. In contrast to the ring geometry case, for which $J_{\mathcal{N}}$ is stationary, the eigenfunctions of $J_{\mathcal{N}}(t)$, $t \in [0, T)$, have no special dynamical meaning. However, the evolution of the stroboscopic section

$\delta\mathbf{z}(t_n)$, $t_n = nT$, $n = 1, 2, ...$, is governed by an autonomous (time independent) map that can serve as the basis for a modal decomposition of the dynamics. We begin by considering the time integrated form [4] of (58)

$$\delta\mathbf{z}(t_f) = U(t_f, t_i)\delta\mathbf{z}(t_i) - \int_{t_i}^{t_f} U(t_f, t)\mathbf{j}_c(t)dt \tag{60}$$

where $U(t_f, t_i)$ is the time evolution operator of (58) in the absence of control, $\mathbf{j}_c = 0$. Due to the time-periodicity of $J_{\mathcal{N}}(t)$, $U(t_f, t_i)$ is time-periodic with period T,

$$U(t_f + T, t_i + T) = U(t_f, t_i). \tag{61}$$

From (103) and (61) we obtain

$$\delta\mathbf{z}(t_{n+1}) = U(T, 0)\delta\mathbf{z}(t_n) - \int_0^T U(T, t)\mathbf{j}_c^n(t)dt, \tag{62}$$

where $\mathbf{j}_c^n(t) = \mathbf{j}_c(t_n + t)$, t in $[0, T]$.

Let us define the eigenfunctions $\mathbf{e}_i$ and eigenvalues λ_i (Floquet multipliers [4]) of $U(T, 0)$,

$$U(T, 0)\mathbf{e}_i = \lambda_i\mathbf{e}_i. \tag{63}$$

It is possible to further simplify the dynamics of perturbations by expressing $\delta\mathbf{z}(t_n)$ as a linear combination of the eigenfunctions $\mathbf{e}_i$,

$$\delta\mathbf{z}(t_n) = \sum_{i=1}^{\infty} \xi_i^n \mathbf{e}_i. \tag{64}$$

Then, through a Galerkin projection of (62) one can obtain an evolution equation for the coefficients ξ_i^n. Let $\mathbf{f}_i$ denote the eigenfunctions of $U^\dagger(T, 0)$,

$$U^\dagger(T, 0)\mathbf{f}_i = \lambda_i^*\mathbf{f}_i. \tag{65}$$

subject to normalization condition (53). Substituting (64) into (62) and applying the operation $\langle\mathbf{f}_j, \cdot\rangle$ to each side of the resulting equation we obtain

$$\xi_i^{n+1} = \lambda_i\xi_i^n - \left\langle \mathbf{f}_i, \int_0^T U(T, t)\mathbf{j}_c^n(t)dt \right\rangle. \tag{66}$$

From (66) we see that the spontaneous ($\mathbf{j}_c(t) = 0$) evolution of the modal amplitudes ξ_i^n is given by

$$\xi_i^{n+1} = \lambda_i^n \xi_i^0. \tag{67}$$

Therefore, the normal rhythm will be unstable if $|\lambda_i| > 1$ for at least one eigenmode.

3.3 Bifurcation analysis in the ring geometry

For the ring geometry, the period T and the length L are functions of each other, $T = L/c(L)$. So, they are essentially the same bifurcation parameter. In contrast, for the open fiber, T and L are independent, thereby constituting a two dimensional parameter space.

The methods for the calculation of the normal rhythm $\mathbf{z}_p$ and the left and right eigenfunctions, $\mathbf{e}_i$ and $\mathbf{f}_i$, of $J_{\mathcal{N}}$ are described in Sect. A.3. The real parts of the five leading eigenvalues are shown in Fig. 12 as functions of the ring length L. The trivial eigenvalue, $\mu_1 = 0$, is independent of the ring length L, with $\mathbf{e}_1 = \partial_x \mathbf{z}_p$. This is a reflection of the translational symmetry of (40): $\mathbf{z}_p$ remains a stationary solution if shifted by an arbitrary distance. The other four are pairs of complex conjugate eigenvalues. For $L > L_c \approx 10.03$ cm, all eigenvalues except for μ_1 have a negative real part, such that $\mathbf{z}_p$ is stable, in agreement with the result presented in Fig. 8. The first complex pair, $\mu_2 = \mu_3^*$ acquires a positive real part for $L < L_c$, indicating that a Hopf bifurcation takes place at L_c, giving rise to an oscillatory solution shown in Fig. 10. The target state $\mathbf{z}_p$ becomes linearly unstable, with small perturbations $\delta\mathbf{z}$ growing until the system reaches the state of fully developed alternans with amplitude saturated by nonlinearities.

In [3], several instabilities producing oscillations of the thickness of the spiral wave (there called "alternans modes") were demonstrated. This supports the notion that studies in a ring geometry can be of relevance to understanding the dynamics in two dimensions.

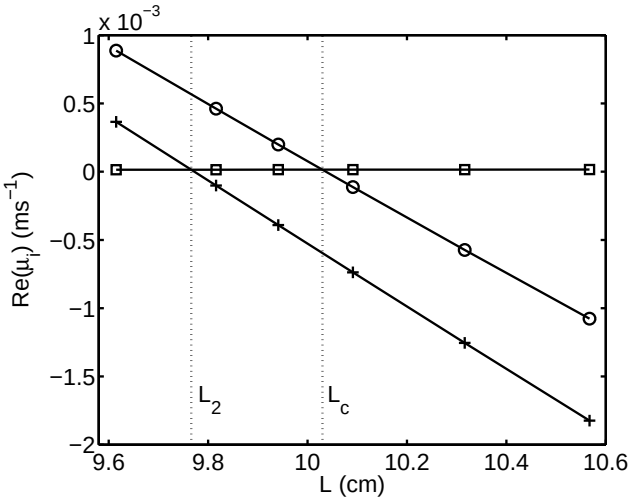

Figure 12: Real part of the five leading eigenvalues of J_N as a function of the ring length L. Zero eigenvalue μ_1 (squares) is associated with translational symmetry. The first pair of complex conjugate eigenvalues $\mu_2 = \mu_3^*$ (circles) becomes unstable at $L = L_c \approx 10.03$ cm ($T = 237$ ms). The second pair of complex conjugate eigenvalues $\mu_4 = \mu_5^*$ (crosses) becomes unstable at $L = L_2 \approx 9.77$ cm ($T = 232$ ms).

We will establish if the Hopf bifurcation is subcritical or supercritical. In order to quantify the oscillation amplitude, we will define the width of the action potential, $W(t)$, as the length of the *spatial* domain for which the transmembrane voltage u is above some threshold u_{th}. In this work we set $u_{\text{th}} = 0.4$ (see Fig. 11). The amplitude of the alternans, $A_W \equiv \max_t W(t) - \min_t W(t)$, shown in Fig. 13 as a function of L is well fitted by a square root law $A_W = b|L - L_c'|^{1/2}$ (solid line), characteristic of a supercritical Hopf bifurcation. The fitting parameters were found to be $b = 6.53$ cm$^{1/2}$ and $L_c' = 10.04$ cm using the method of least squares, in agreement (up to the third significant figure) with the value of the critical ring length L_c found via linear stability analysis.

A theoretical investigation [64] and a clinical one [59] discovered that often the state of alternans possesses memory; that is, the alternans produced by an increase in the pacing rate persist even when the rate is subsequently decreased below the threshold at which it was induced. This hysteretic behavior suggests that for a range of pacing rates a stable state of alternans and a stable normal rhythm state coexist

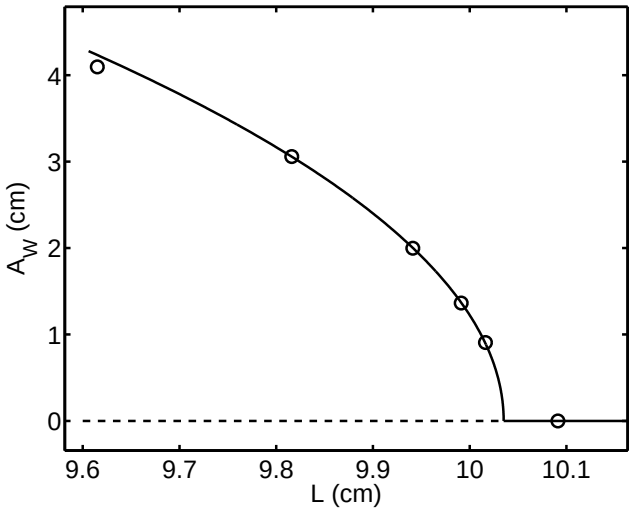

Figure 13: Amplitude of alternans as a function of the ring length L. The solid curved line is the least squares fit, $A_W = b|L - L'_c|^{1/2}$, computed using the four middle points. The horizontal solid (dashed) line corresponds to the stable (unstable) steady state $\mathbf{z}_p$.

(bistability). The *supercritical* Hopf bifurcation found here shows that the Fenton-Karma model on a ring does not possess the memory effect (the latter being consistent with a *subcritical* Hopf bifurcation).

3.4 Bifurcation analysis for the open fiber

The methods for the calculation of the normal rhythm $\mathbf{z}_p$ and the left and right eigenfunctions, $\mathbf{e}_i$ and $\mathbf{f}_i$, of the evolution operator $U(T, 0)$ for the open fiber are described in Sect. A.2. The number of unstable eigenvalues ($|\lambda_i| > 1$) found for a grid of pairs (L, T) is shown in Fig. 14. Fig. 21 (top) shows the regimes approached by advancing an initial condition over many pacing periods (see Sect. 4.2.2 for details) for the same grid of (L, T) points. Note that the transition from zero to one unstable eigenmode in Fig. 14 corresponds point to point to the transition from the normal rhythm to the state of alternans (either concordant or discordant) in Fig. 21 (top). This confirms that alternans develops when the normal rhythm becomes unstable. The instability occurs when the pacing period T becomes smaller than a critical value T_c that is nearly the same (265 ms $< T_c <$ 270 ms) for all L values plotted.

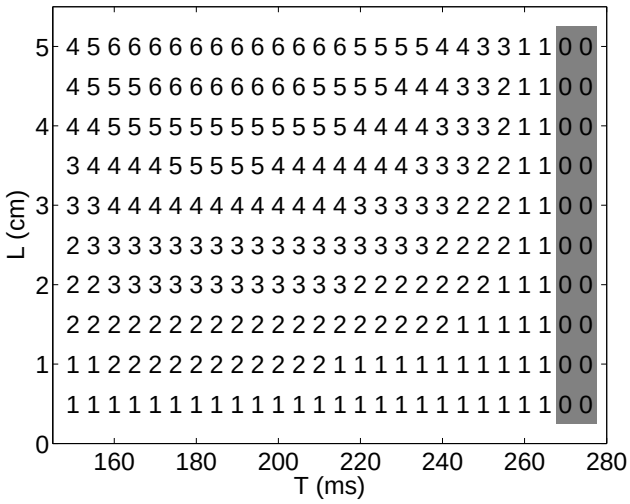

Figure 14: Number of unstable modes for the normal rhythm. The normal rhythm is stable in the shaded region and unstable otherwise.

Fig. 15 shows the effect of perturbations proportional to the leading mode and subleading modes, $\mathbf{e}_1$ and $\mathbf{e}_2$, respectively. We generated this figure by evolving in time the initial conditions $\mathbf{z}_p + \epsilon\mathbf{e}_1$ and $\mathbf{z}_p + \epsilon\mathbf{e}_2$, with ϵ small. Both $\mathbf{e}_1$ and $\mathbf{e}_2$ correspond to $L = 2$ cm and $T = 220$ ms. As shown in Fig. 14, for these L and T values, both $\mathbf{e}_1$ and $\mathbf{e}_2$ are unstable. Hence both eigenmodes grow until saturation due to nonlinearity is reached. Note that $\mathbf{e}_1$ produces concordant alternans, while $\mathbf{e}_2$ produces discordant alternans, from the small perturbations shown in panels (a) and (d) all the way up to the asymptotic states shown in panels (c) and (f), suggesting that two different alternans states can coexist.

One can perform linear stability analysis of the state of alternans by the methods presented in Sect. A.2. For this purpose, one needs only to substitute the normal rhythm $\mathbf{z}_p$ (a periodic orbit with period T) with the state of alternans (a periodic orbit with period $2T$). In this way we find that the states of concordant and discordant alternans reached asymptotically (panels (c) and (f) of Fig 15) are indeed both stable. As far as we know this coexistence of stable discordant alternans and stable concordant alternans for the same L and T values (bistability) has not been shown previously in the literature.

The bistability of concordant and discordant alternans at a point in the L, T parameter space raises the question about the region of parameters inside of which this bistability is present. Fig. 16 shows the leading eigenvalue λ_1 of the state of alternans for $L = 2.5$ cm and different T. Note that for 225 ms $\lesssim T \lesssim$ 240 ms the diagram presents three branches corresponding to three different types of alternans. Two of the branches are stable, $|\lambda_1| < 1$ (solid lines), while the third one is unstable, $|\lambda_1| > 1$ (dashed line). Alternatively, one can regard the λ_1 diagram as a smooth curve that intersects itself at a single point. We labeled seven points on this curve, with letters "a" through "g", in order of increasing arc length starting at point "a". The APD plots corresponding to these points are shown in Fig. 17. One can see that the two APD branches ($\mathrm{APD}_n(x)$ and $\mathrm{APD}_{\mathrm{n+1}}(\mathrm{x})$) of concordant alternans [panel (a)] gradually get closer at the right end until they join forming a node [panel (d)]. This node then moves toward the left giving rise to discordant alternans [panels (e) through (g)].

At the two points of transition from stable to unstable alternans ($|\lambda_1| = 1$), nearby points (b) and (f), the tangent to the λ_1 curve is vertical, which is characteristic of a saddle node bifurcation. Therefore, one can regard the λ_1 plot as two saddle node bifurcation diagrams that share the same unstable branch. Preliminary results suggest a similar λ_1 diagram for other L values, with the difference that the interval where the three branches appear moves toward bigger (lower) T values as L is increased (decreased). These results suggest that the transition from concordant to discordant alternans occurs through a cusp bifurcation in the (L, T) parameter space.

3.5 Conclusion

In both the ring and the open fiber, the onset of the state of alternans occurs when the normal rhythm becomes linearly unstable. For the ring geometry the state of alternans is a stable limit cycle originating at the bifurcation point, $L = L_c$, through

a supercritical Hopf bifurcation. For the open fiber, the destabilization of the normal rhythm is due to a period-doubling (or flip) bifurcation ($\lambda_c = -1$, see Fig 42). Additionally, the transition from concordant to discordant alternans is mediated by a cusp bifurcation. This bifurcation entails a region in the (L, T) parameter space in which three different states of alternans coexist: stable concordant alternans, stable discordant alternans and an unstable state with properties intermediate between those of concordant and discordant alternans.

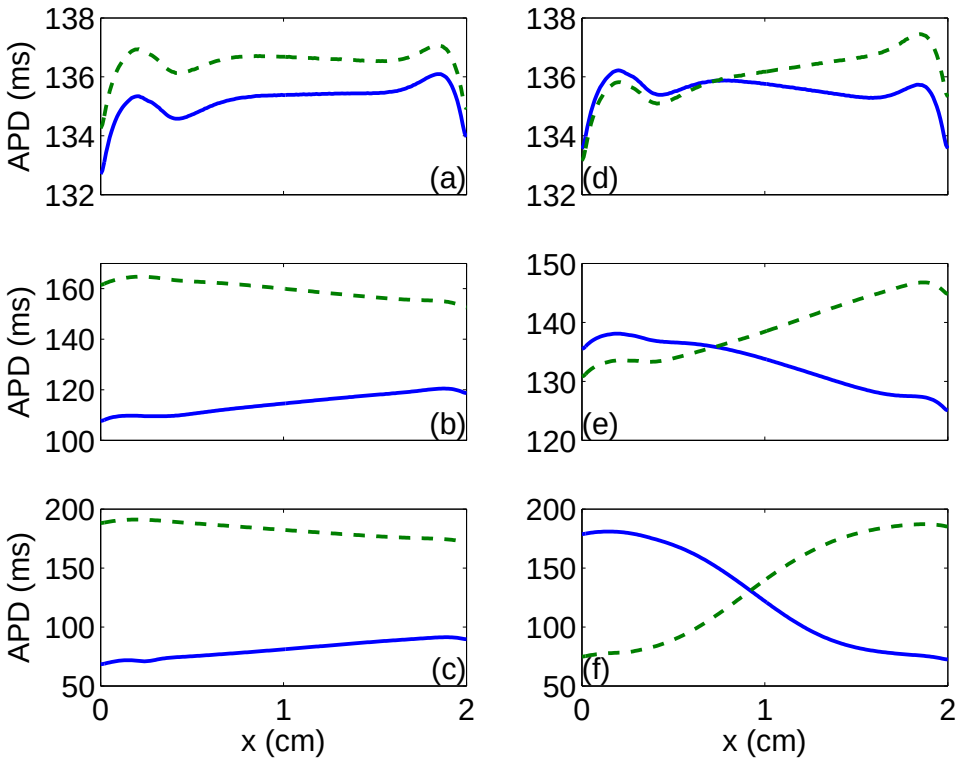

Figure 15: $\mathrm{APD}_n(x)$ during the free evolution of a perturbation proportional to the leading eigenmode, $\delta\mathbf{z} \propto \mathbf{e}_1$, (left side) and another proportional to the subleading eigenmode, $\delta\mathbf{z} \propto \mathbf{e}_2$, (right side). $L = 2$ cm and $T = 220$ ms in both cases. The solid line corresponds to beat number n and the dashed one to $n + 1$. The beat number is as follows: (a) $n = 1$; (b) $n = 15$; (c) $n = 25$; (d) $n = 1$; (e) $n = 15$ and (f) $n = 35$. Note that $\mathbf{e}_1$ produces concordant alternans while $\mathbf{e}_2$ produces discordant alternans, from the small perturbations shown in panels (a) and (d) all the way up to the asymptotic states shown in panels (c) and (f). Linear stability analysis shows that the asymptotic states of concordant and discordant alternans are both stable. This shows that stable concordant and discordant alternans can coexist for the same values of L and T.

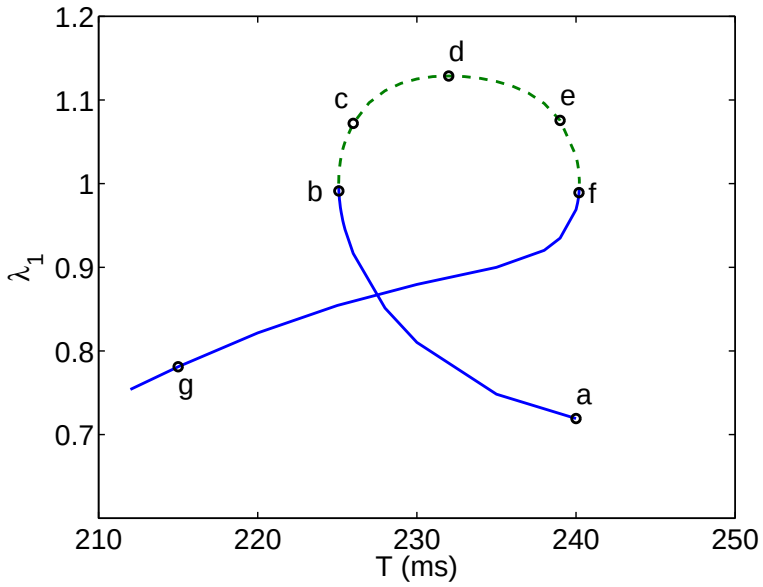

Figure 16: Leading eigenvalue λ_1 of alternans for $L = 2.5$ cm. Note the coexistence of three different states of alternans for 225 ms $< T <$ 240 ms. The APD plots corresponding to the states labeled "a" through "g" are shown in Fig. 17.

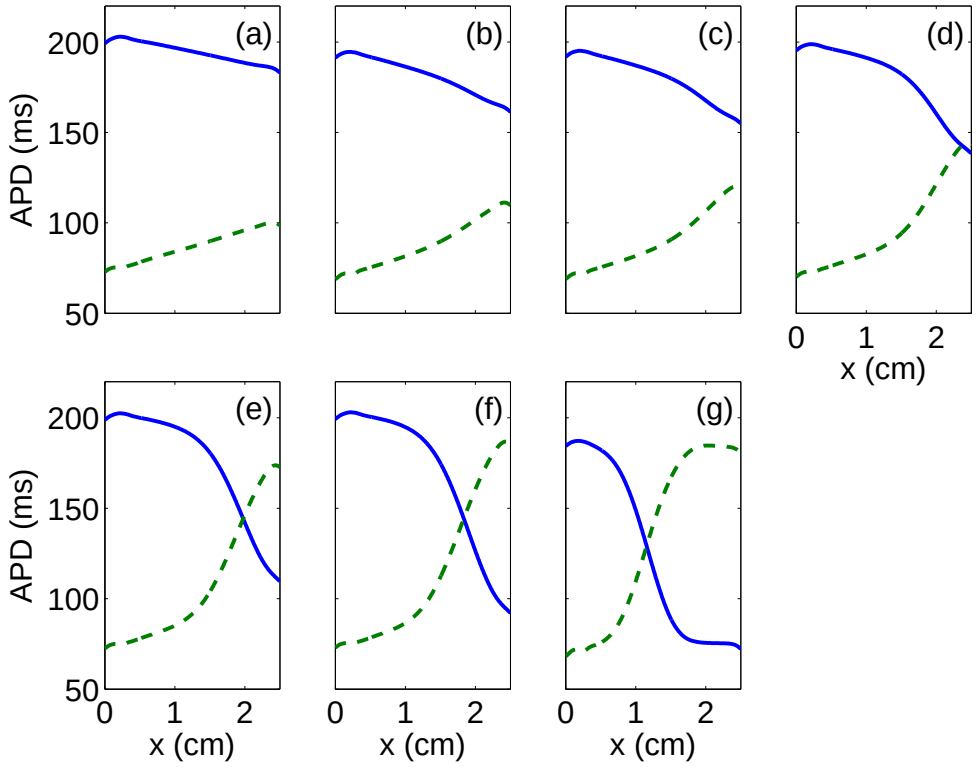

Figure 17: APD plots of the states of alternans labeled "a" through "g" in Fig. 16. The solid (dashed) line corresponds to $\mathrm{APD}_n(x)$ with n odd (even). Note the gradual transition from concordant to discordant alternans from (a) to (g).

CHAPTER IV

CONTROL

4.1 Introduction

For values of the model parameters for which the normal rhythm is unstable ($L < L_c$ for the ring, or $T < T_c$ for the open fiber) the system state will evolve toward the state of alternans. The goal of control is to revert this spontaneous dynamics through application of an external stimulus so that effectively the normal rhythm becomes an attractor. The methods used for achieving this goal are discussed in this chapter.

Rappel et al. [72] studied theoretically the Pyragas control method [69] applied to the suppression of instabilities of reentrant waves in one and two dimensional cardiac tissue. The Pyragas method (also known as time delay auto-synchronization, TDAS) applies a time-continuous control stimulus proportional to the difference between the values of a signal at times separated by a delay. When successful, this method is able to stabilize a periodic orbit with period equal to the time delay. Hall and Gauthier [35], successfully applied a self-referencing scheme, similar in spirit to TDAS, to the suppression of alternans in small patches of paced cardiac tissue. This method adjusts the pacing interval (pacing interval adjustment method, PIA) based on the difference of the two most recent APDs. The performance of PIA in tissue of bigger dimensions, specifically Purkinje fibers a few centimeters long, was studied theoretically by Echebarria and Karma [21] and experimentally by Christini et al. [11]. Both TDAS and PIA have the desirable feature of not requiring a model of the dynamics (we classify them as non-model-based control). However, these methods possess the common limitation of being able to control only a small portion of tissue (per controlling electrode). Rappel et al. estimated that a mesh of electrodes spaced

about 1 cm apart would be required for controlling two dimensional cardiac tissue. Similarly, [21] and [11] both found that PIA fails for fibers longer than 1 cm.

Investigating if control methods that use a model of the dynamics perform better than the non-model-based approaches discussed above is the main motivation of this thesis. We are particularly interested in establishing if model-based approaches can successfully control tissue of larger size than 1 cm. For that purpose, we reduce the model of the dynamics to a linear time invariant system and apply to it standard control methods. For comparison purposes, in Sect. 4.2, we present the results of non-model-based control. The results of model-based control reported in Sect. 4.3, are the main original contribution of this thesis.

4.2 Non model-based control of alternans

4.2.1 Control of the ring

Here we follow Ref. [72]. In particular, we use the 3-variable Fenton-Karma model (Sect. 2.4). The control current $\mathcal{I}_c(t)$ is injected by a single (unipolar) electrode fixed relative to the tissue at x_0:

$$j_c(x,t) = \mathcal{I}_c(t)\, g[s(x - x_0)] \tag{68}$$

(the shift function $s(x)$ was defined in Sect. 2.4). In the calculations reported here, the width of the Gaussian $g(s)$ is $\omega = 0.17$ cm.

The control current was calculated in two ways: using bidirectional feedback

$$\mathcal{I}_c(t) = \gamma \Delta u(t), \tag{69}$$

and using unidirectional feedback

$$\mathcal{I}_c(t) = \gamma\, \Delta u(t) \Theta[\Delta u(t)], \tag{70}$$

where $\Delta u(t) = u(x_0, t) - u(x_0, t - \tau)$, γ is a tunable parameter, and τ is the time delay calculated as in Ref. [72].

TDAS control was tested by simulating the evolution of the system in the stationary reference frame (6) subject to the feedback law (69) or (70) (see Sect. A.1 for the numerical algorithms used).

To assess the performance of time-delay feedback control we investigated the evolution of the system dynamics during bidirectional feedback (69) using the state of fully developed alternans (shown in Fig. 10) as an initial condition, with the ring length $L = 9.94$ cm. This corresponds to $c = 42.3$ cm/s and $T = 235$ ms. The evolution of the action potential (for optimal values of x_0 and γ, as explained below) is shown in Fig. 18. The action potential gradually approaches a stationary state with $W(t) = W_0$. Hence, successful suppression of alternans is achieved.

In order to quantify how quickly alternans is suppressed, we define the control time t_c as the smallest time after control is turned on at $t = 0$ for which the absolute value of the variation of the action potential width, $\delta W(t) = W(t) - W_0$, falls below some threshold, $\delta W_{\rm th}$, to never go above it again. Here we set $\delta W_{\rm th} = 0.05\Delta W$, where ΔW is the maximum value of $|\delta W(t)|$ for the state of fully developed alternans without control. For the value of L used, $\Delta W \approx 0.22 W_0$.

Keeping the gain γ fixed at a value of 34 cm/s, we determined the initial position of the control electrode x_0 giving rise to the lowest value of t_c (this is equivalent to choosing the phase of the oscillation at the instant when the control is turned on). Setting x_0 at that optimal value, we explored the performance of control with different values of γ. As Fig. 19 shows, for TDAS the control time achieves the smallest value $t_c \approx 16.3T = 3.83$ s for $\gamma \approx 34$ cm/s. It should be pointed out that this γ value is close to the pulse speed $c = 42$ cm/s. This similarity is hardly coincidental. However, explaining it will be the topic of future research.

As the system approaches the asymptotic state, $\Delta u(t)$ and, as a result, the control current $\mathcal{I}_c(t)$ vanishes. This indicates that the asymptotic state becomes a steady

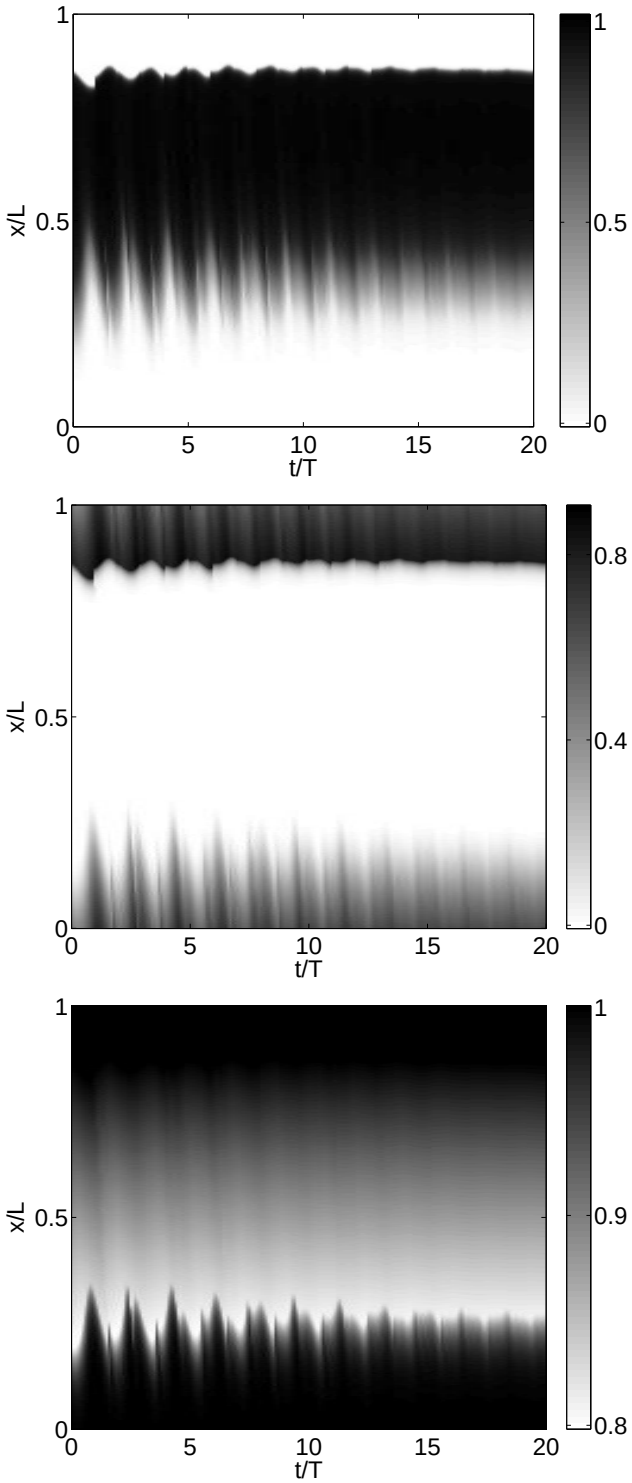

Figure 18: Evolution of the transmembrane voltage u and the gate variables v and w under TDAS control for the ring of length $L = 9.94$ cm. Parameters γ and x_0 were set to the optimal values as described in the text. The initial condition is the state of fully developed alternans shown in Fig. 10.

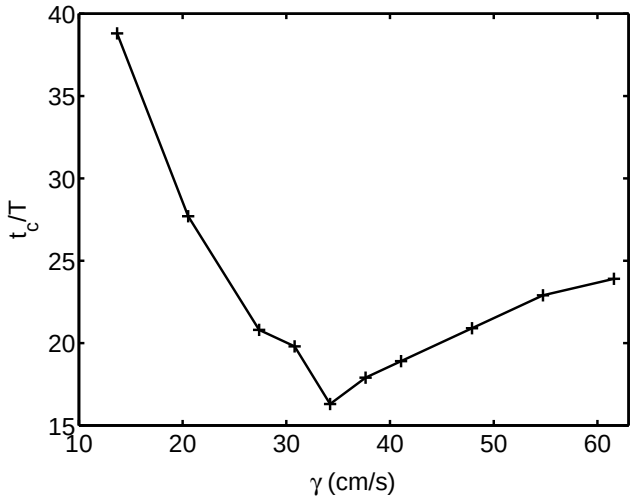

Figure 19: Control time as a function of the control parameter γ for TDAS.

solution (in the absence of control current) of the evolution equation (6), when transformed to the co-moving reference frame (see Sect. 3.3) which corresponds to the target state (36). As we saw in Sect. 3.3, this state is unstable for $L < L_c$, and hence the dynamics spontaneously revert to alternans in the absence of control.

It was argued in Ref. [72] that unidirectional feedback (70) effectively restricts the application of the control current to times during which the cells are passing through the repolarization phase of the action potential, eliminating conduction block. This effect was not observed in the model considered here. In particular, the unidirectional feedback (70) produced non-zero control current in both the repolarization and depolarization phases. Furthermore, we found no relation between the phase of the action potential and the sign of Δu. In some cases, while using the bidirectional feedback (69), the sign of Δu alternated from positive to negative from one period to the next in both the depolarization and repolarization phases. This behavior is partially illustrated by Fig. 20, which shows the control current calculated via (69). Notice the alternating sign of the narrow spikes corresponding to the depolarization phase. Also, notice how the small bumps associated with the repolarization phase are initially negative but become positive in later stages. Bidirectional feedback was

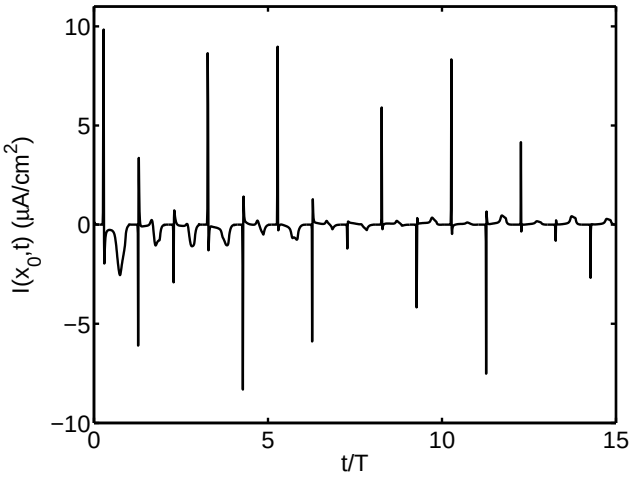

Figure 20: Control current density at the location of the control electrode ($I(x_0, t)$ as seen in the stationary reference frame) as a function of time for TDAS.

generally found to perform better than unidirectional which explains why it is chosen as the reference for comparison with model-based control.

There are many potential reasons why our findings differ from those of the earlier study [72]. Here only one control electrode is used, while Rappel *et al.* simulated the action of multiple electrodes. Moreover, the earlier study also used a different ionic model. Our results suggest that the effect of bi- and uni-directional feedback currents on the emergence of conduction block requires further investigation.

Although TDAS is able to achieve the main control goal (suppression of alternans) when other factors are considered, namely, control speed and minimization of possible tissue damage, a model-based approach produces more satisfactory results, as we will see in Sect. 4.3.3.2.

4.2.2 Control of the open fiber

Echebarria and Karma [21] achieved limited success in the suppression of alternans in an open fiber with a method that adjusted the pacing interval $T_n = t_{n+1} - t_n$, where t_n is the time of the n^{th} pacing stimulus, based on the difference between the two

most recent APD values,

$$T_n = T + \Delta T_n, \tag{71}$$

with

$$\Delta T_n = \frac{\gamma}{2}[\mathrm{APD}_n(x_p) - \mathrm{APD}_{n-1}(x_p)] \tag{72}$$

where γ is a tunable constant and x_p is the location of the pacing electrode. Throughout this work we will call this control procedure the pacing interval adjustment (PIA) method.

The results reported in [21] set the benchmark against which the control procedures for the open fiber that we propose in this work are measured. As a validation for our numerical algorithms we reproduced the results of Echebarria and Karma using the same ionic current model (Sect. 2.3). We explored the performance of PIA for different T values using the protocol from [21]: for a given length, we decreased T in steps of 5 ms starting from a value where alternans were absent and applied 200 stimuli for each value of T. We repeated this procedure for different lengths. We emphasize again that while in Ref. [21] the pacing electrode is located at the left end of the fiber ($x_p = 0$), we used $x_p = 0.25$ cm, for the reason explained in Sect. 2.3. As we show below, this difference in x_p does not introduce any significant discrepancy between our results and those of Ref. [21]. The width ω of the spatial profile of the pacing current [see equations (13) and (9)] was set to 0.1 cm.

Fig. 21 (bottom) shows the dynamical regimes the fiber is driven to by PIA control with $\gamma = 1/2$ (this γ value is the same as in [21]). For comparison purposes, we also studied the uncontrolled case [Fig. 21 (top)]. We did this by setting $\gamma = 0$ in the control procedure. This means that the pacing period was decreased by 5 ms every time a sequence of 200 pacing stimuli with *fixed* pacing period was completed. As we saw in Sect. 3.4, in some regions in the (L, T) parameter space, two stable states of alternans coexist. 200 pacing stimuli is in most cases a long enough time for the dynamics to approach one of these stable states. Which of these two states

is selected depends on the initial conditions, which in turn, are determined by the pacing protocol used. Therefore, the phase diagram does not reveal the regions of bistability.

To assess the effectiveness of control, one should compare the extent of the region where the normal rhythm is the asymptotic state in the controlled and uncontrolled cases. As Fig. 21 (top) shows, in the absence of control, the onset of alternans occurs at roughly the same pacing period ($T \approx 265$ ms) for all L values in the range shown. PIA is able to suppress alternans (solid circles) for either short fibers or (in general) low pacing rates. For longer fibers and higher pacing rates the alternations of the APD are greatly reduced at the pacing location but not away from it. A state in which the amplitude of APD oscillations increases monotonously with the distance from the pacing site develops. Following [21] we label this state "first harmonic standing wave" (Fig. 22). Further increase of the pacing rate or fiber length produces traveling discordant alternans illustrated in Fig. 23 . At even faster pacing rates and greater fiber lengths the pacing current fails to produce a traveling action potential. This regime is known as conduction block.

Note that Fig. 21 is qualitatively similar to Fig. 3 of Ref. [21]. This supports our statement above in the sense that the change of the pacing electrode location from $x_p = 0$ to $x_p = 0.25$ cm does not change the results in any significant way. Besides the position of the pacing electrode, another factor that could explain the differences between our results and those of Ref. [21] is the time step Δt used for the integration of the evolution equation. Ref. [21] uses $\Delta t = 0.05$ ms while we use a shorter time step $\Delta t = 0.01$ ms (leading to numerically more accurate results). In either case, PIA is incapable of suppressing alternans in a wide range of pacing rates for fibers longer than about 1 cm. This is the major limitation that we intend to overcome and explain here.

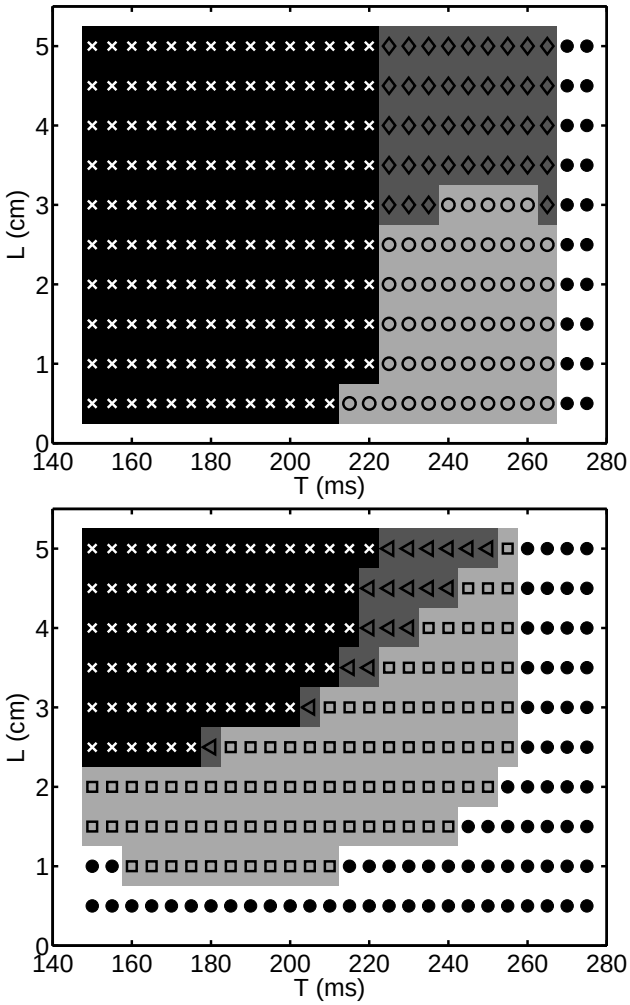

Figure 21: Top: dynamical regimes approached in the absence of control ($\gamma = 0$). Bottom: dynamical regimes approached during PIA control with $\gamma = 1/2$. Solid circles: normal rhythm. Open circles: concordant alternans (a typical APD diagram of this regime is shown in Fig. 4). Diamonds: discordant stationary alternans (Fig. 5). Open squares: first harmonic standing waves (Fig. 22). Triangles: traveling discordant alternans (Fig. 23). Crosses: conduction block. Levels of gray added to aid visualization.

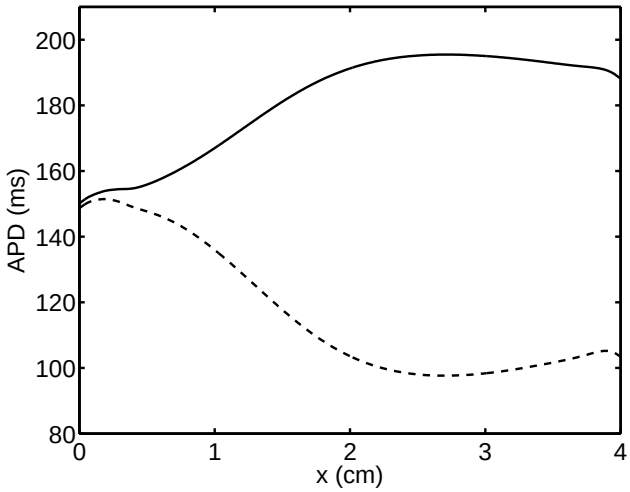

Figure 22: First harmonic standing wave: $\mathrm{APD}_n(x)$ following odd (solid line) and even (dashed line) pacing stimuli. The parameters are $L = 4$ cm and $T = 250$ ms.

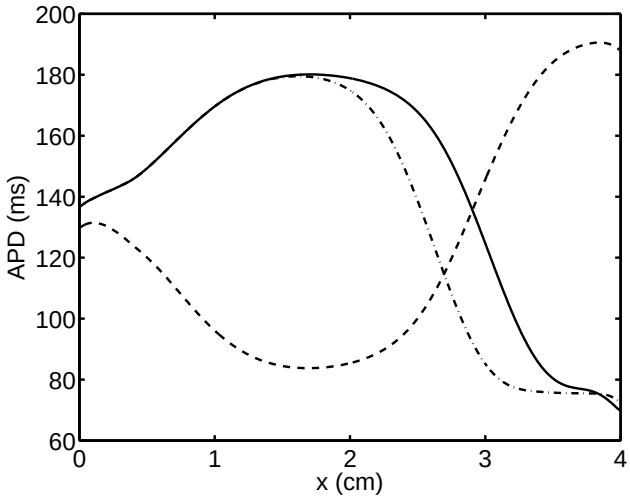

Figure 23: Traveling discordant alternans: $\mathrm{APD}_n(x)$ [solid line], $\mathrm{APD}_{n+1}(x)$ [dashed line] and APD_{n+10} [dashed-dotted line] for a particular beat number n. The parameters are $L = 4$ cm and $T = 220$ ms.

4.3 Model-based control of alternans

In experiments one has to rely on electrodes to both perform measurements and apply control. Hence, control methods should be designed with this restriction in mind.

The control method presented for the ring geometry uses a time-continuous control current applied by a single electrode and relies on the assumption that the state variables are known at all points on the ring. Although measurement of all state variables at all points in the tissue is not possible in practice, there is a way of circumventing this difficulty, as we will see in the treatment of the open fiber.

For the open fiber, model-based control employs a single electrode that injects a short pulse of current on each pacing interval. The control current is calculated based on the system state which is estimated from measurements of the transmembrane voltage recorded by a single electrode.

In Sect. 4.3.1 we derive a discrete-time description (stroboscopic map) of the dynamics of the modal amplitudes at times $t_n = nT$, $n = 1, 2, ...$, where T is either the pacing period (open fiber) or the circulation period (ring). The techniques for controlling this map are presented in in Sect. 4.3.2. Sects. 4.3.3 and 4.3.4 report the results of control for the ring and the open fiber respectively.

4.3.1 Stroboscopic map for the modal amplitudes

4.3.1.1 Ring geometry

For a single electrode located at x_c, the control current density $\mathbf{j}_c(t)$ has the form,

$$\mathbf{j}_c(t) = \mathcal{I}_c(t)\mathbf{g}[s(x - x_c)]. \tag{73}$$

To facilitate direct comparison, we assume that the Gaussian width is the same as that used for TDAS, $\omega = 0.17$ cm. An electrode fixed with respect to the tissue will appear moving in the co-moving reference frame with position given by $x_c = (x_0 - ct)$ mod L. Substituting (73) into (54) we obtain

$$\dot{\xi}_i = \mu_i \xi_i - \mathcal{I}_c(t)\eta_i(x_0 - ct), \tag{74}$$

where

$$\eta_i(x_0 - ct) = \langle \mathbf{f}_i, \mathbf{g}\{s[x - x_c(x_0 - ct)]\}\rangle \,. \tag{75}$$

The time integrated form of (74) is

$$\xi_i(t_f) = \exp[\mu_i(t_f - t_0)]\xi(t_0) - \int_{t_0}^{t_f} \exp[\mu_i(t_f - t)]\mathcal{I}_c(t)\eta_i(x_0 - ct), \tag{76}$$

$\eta_i(x_0 - ct)$ is a periodic function of time with period $T = L/c$. Therefore it is natural to introduce the stroboscopic section of the dynamics $\xi(t_n)$ with $t_n = nT$. From (76) we obtain

$$\xi_i(t_{n+1}) = \exp(\mu_i T)\xi_i(t_n) + \int_0^T \exp[\mu_i(T - t)]\mathcal{I}_c^n(t)\eta_i(x_0 - ct)dt, \tag{77}$$

where $\mathcal{I}_c^n(t) = \mathcal{I}_c(t_n + t)$, $t \in [0, T)$. We represent $\mathcal{I}_c^n(t)$ by a superposition of l independent of n functions $\beta_k(t)$,

$$\mathcal{I}_c^n(t) = \sum_{k=1}^{l} \nu_k^n \beta_k(t). \tag{78}$$

The physical meaning of the coefficients ν_k^n depends on the shape of the functions $\beta_k(t)$, as illustrated in Sects. 4.3.3.2 and 4.3.4. Using (78), (77) can be reduced to

$$\xi_i^n = \lambda_i \xi_i^n + \sum_{i=1}^{l} B_{ik}\nu_k^n, \tag{79}$$

where $\xi_i^n = \xi_i(t_n)$, $\lambda_i = \exp(\mu_i T)$ and

$$B_{ik} = \lambda_i \int_0^T \exp(-\mu_i t)\beta_k(t)\eta_i(x_0 - ct)dt. \tag{80}$$

Modes with $|\lambda_i| \ll 1$ decay quickly and need not be considered. In order to identify this set of quickly decaying modes, let us consider the form of $J_{\mathcal{N}}$. The first two terms in (46) are spatial derivatives that attain large values for functions that vary quickly in space. These are unbounded operators. The third term on the other hand is a local matrix-vector product and hence is bounded. Consequently, when acting on quickly varying functions of space, $J_{\mathcal{N}}$ can be approximated by the

first two terms only, in which case it possesses eigenmodes $[\exp(jq_i x), 0, ..., 0]$, where $j = \sqrt{-1}$ and q_i is quantized by the periodic boundary conditions, $q_i = 2\pi i/L$ with i an integer number. The corresponding eigenvalues are $\mu_i = -Dq_i^2 + jcq_i$. We can see then that modes that oscillate quickly in space, $|i| \gg 1$, show fast decay in time, $|\lambda_i| = \exp[\mathrm{Re}(\mu_i)T] \ll 1$, due to the diffusive coupling represented by the term $\widetilde{D}\partial_x^2$ and hence can be discarded.

The evolution equations (79) of the retained (unstable or slowly decaying) m modal amplitudes ξ_i^n can be gathered into a single matrix equation,

$$\boldsymbol{\xi}^{n+1} = A\boldsymbol{\xi}^n + B\boldsymbol{\nu}^n, \tag{81}$$

where $\boldsymbol{\xi}^n = [\xi_1^n, \xi_2^n, ..., \xi_m^n]^{\mathcal{T}}$, A is a diagonal matrix with elements $A_{ii} = \lambda_i$ and $\boldsymbol{\nu}^n = [\nu_1^n, \nu_2^n, ..., \nu_l^n]^{\mathcal{T}}$. The map (81) is known as a linear time-invariant system. The qualifier *time-invariant* refers to the fact that the matrices A and B are independent of the beat number n.

One can also arrive at a map of the same form (81) by assuming that feedback current is applied by several electrodes placed at locations x_c^k,

$$\mathbf{j}_c^n = \beta(t) \sum_{k=1}^{l} \mathcal{I}_k^n \mathbf{g}[s(x - x_c^k)], \tag{82}$$

where $\beta(t)$ is a common time profile weighted in a different way for each electrode by the prefactor $\mathcal{I}_k^n$. In this case $\nu_k^n = \mathcal{I}_k^n$ and

$$B_{ik} = \lambda_i \int_0^T \exp(-\mu_i t)\beta(t)\eta_{ik}(x_0^k - ct)dt, \tag{83}$$

where

$$\eta_{ik}(x_0^k - ct) = \left\langle \mathbf{f}_i, \mathbf{g}\{s[x - x_c^k(x_0^k - ct)]\}\right\rangle. \tag{84}$$

4.3.1.2 Open fiber

For the open fiber, the control current applied by a single electrode located at x_c, $\mathbf{j}_c^n(t)$ [defined in Eq.(62)], has the form,

$$\mathbf{j}_c^n(t) = \mathcal{I}_c^n(t)\mathbf{g}(x - x_c). \tag{85}$$

As for the ring geometry, we assume $\mathcal{I}_c^n(t)$ to be a superposition of l functions $\beta_k(t)$,

$$\mathcal{I}_c^n(t) = \sum_{k=1}^{l} \nu_k^n \beta_k(t). \tag{86}$$

Using (85) and (86), (66) becomes

$$\xi_i^{n+1} = \lambda_i \xi_i^n + \sum_{i=1}^{l} B_{ik} \nu_k^n, \tag{87}$$

where

$$B_{ik} = \left\langle \mathbf{f}_i, \int_0^T \beta_k(t) U(T,t) \mathbf{g}(x - x_c) dt \right\rangle. \tag{88}$$

Discarding quickly decaying modes ($|\lambda_i| \ll 1$), we obtain the evolution equation for the remaining m modal amplitudes ξ_i^n in the form (81) again.

4.3.2 Control of linear time-invariant systems

Our control goal is to choose the control stimuli $\boldsymbol{\nu}^n$, in such a way that $\boldsymbol{\xi}^n$ approaches zero asymptotically, so that $\delta\mathbf{z}$ vanishes and the normal rhythm $\mathbf{z}_p$ is stabilized.

The control methods discussed below use the feedback law

$$\boldsymbol{\nu}^n = -K\boldsymbol{\xi}^n, \tag{89}$$

where K is a matrix of feedback gain. Substitution of (89) into (81) gives the closed loop map

$$\boldsymbol{\xi}^{n+1} = (A - BK)\boldsymbol{\xi}^n. \tag{90}$$

Therefore, a necessary condition for successful control is that the matrix K be chosen so that $A-BK$ is stable (have all its eigenvalues inside the unit circle). If the dynamics were described exactly by the linear map (81) this would also be a sufficient condition. However, (81) is an approximation to the actual dynamics (44) that breaks down if the perturbation $\delta\mathbf{z}$ becomes large enough. Hence, the control method not only has to suppress the perturbation asymptotically but also needs to keep it bounded away from the nonlinear regime at all times.

The method of *pole placement* [91] yields a matrix K such that the eigenvalues (poles) of the matrix $A - BK$ belong to a set Ω_i, $i = 1, 2, ..., m$, chosen beforehand. K can be computed using the Matlab function **place**. Successful control is achieved by finding a set Ω_i such that the two conditions discussed above are met. The first condition (stability of $A - BK$) is satisfied if $|\Omega_i| < 1$. The way to satisfy the second condition (preventing the perturbation from reaching the nonlinear regime) is less obvious. One can develop some intuition by considering two extremes in which this condition is not satisfied. Fast control, $|\Omega_i| \ll 1$, could only be achieved by applying large control stimuli which would generically excite modes discarded in (81). Nonlinear coupling of these modes with the m retained modes would lead to significant deviations of the dynamics from (81) (an effect similar to this will be considered in Sect. 4.3.3.1). On the other hand, slow control, $1 - |\Omega_i| \ll 1$ could allow the perturbation to grow transiently and reach the nonlinear regime. Suitable values of Ω_i can be obtained by a trial-and-error search between these two extremes. This search could be performed for instance, by exploring points on an m-dimensional grid. However, if m is large the grid will possess too many points and the trial-and-error search will be rendered impractical.

A technique that allows one to sidestep this difficulty is *linear quadratic regulator* (LQR) control [17]. It is based on choosing K so as to minimize the quadratic cost function

$$\mathcal{G} = \sum_{n=1}^{\infty} \left[(\boldsymbol{\xi}^n)^\dagger \, Q \, \boldsymbol{\xi}^n + (\boldsymbol{\nu}^n)^\dagger \, R \, \boldsymbol{\nu}^n \right], \tag{91}$$

where Q and R are arbitrary positive-definite constant matrices that can be chosen to achieve a particular optimization goal. In particular, setting $Q_{ik} = \langle \mathbf{e}_i, \mathbf{e}_k \rangle / L^2$ and $R = r_0 \widetilde{1}$, where $\widetilde{1}$ is the $l \times l$ unit matrix and r_0 is a scalar, reduces (91) to the form

$$\mathcal{G} = \sum_{n=1}^{\infty} \frac{1}{L^2} \|\delta \mathbf{z}(t_n)\|^2 + r_0 \sum_{n=1}^{\infty} \frac{1}{l} \|\boldsymbol{\nu}^n\|^2, \tag{92}$$

where $\|\delta \mathbf{z}\|^2 = \langle \delta \mathbf{z}, \delta \mathbf{z} \rangle$ and $\|\boldsymbol{\nu}^n\|^2 = \boldsymbol{\nu}^n \cdot \boldsymbol{\nu}^n = \sum_{k=1}^{l} (\nu_k^n)^2$. The expression (92)

does not favor any position x in space or any particular beat number n. Hence, it is consistent with the assumed spatial homogeneity of the tissue and the temporal periodicity of the pacing current. The first sum in (92) quantifies the deviation from the target state and therefore minimizing this sum increases the speed of convergence. In this way we avoid a large transient growth of the perturbation that could drive the system into the nonlinear regime. This is a desirable behavior given that transient growth is a generic feature of spatially localized control [36]. By minimizing the second sum one reduces the control current thereby avoiding conduction block and the excitation of the modes discarded in (81). Minimization of the first and second sum in (92) are mutually exclusive goals. Therefore, one must aim at a trade off between the two, determined by the value of r_0.

The feedback gain matrix K is related to the solution of a matrix Riccati equation which incorporates matrices A, B, Q, and R. We computed it using the function `dlqr` of MATLAB.

4.3.3 Control of alternans in the ring geometry

4.3.3.1 Quasi-instantaneous suppression of unstable modes (QISUM)

Otani and collaborators [51, 3] have also proposed a control method that uses a projection of the dynamics onto the eigenmodes. This method is simpler than the feedback control of the stroboscopic map discussed above. Here we study its performance for the suppression of alternans on the ring.

The idea of the method is to eliminate the unstable modes by applying a short current stimulus. We should point out that this is essentially a particular implementation of dead beat control [46]. Suppression of alternans using this method was investigated both for single cells and for 2D tissue. In the latter case the target state was a spiral wave that appears stationary when observed in a rotating reference frame. In this sense the spiral wave is analogous to the traveling wave solution on the ring considered here.

The effect on individual modes of a constant control current $\mathcal{I}_c(t) = \mathcal{I}_c^n$ acting during a brief time interval $[t_n, t_n + \Delta t]$ can be calculated by integrating (74) over that interval:

$$\begin{aligned} \xi_i(t_n + \Delta t) &= \xi_i(t_n) + \lambda_i \int_{t_n}^{t_n+\Delta t} \xi_i(t) dt \\ &- \mathcal{I}_c^n \int_{t_n}^{t_n+\Delta t} \eta_i(x_0 - ct) dt. \end{aligned} \tag{93}$$

Assuming the interval is short enough ($\lambda_i \Delta t \ll 1$), (93) can be approximated by

$$\xi_i(t_n + \Delta t) - \xi(t_n) = -\mathcal{I}_c^n \Delta t \; \eta_i(x_0 - ct_n). \tag{94}$$

The method requires the feedback current to be chosen such that

$$\xi_i(t_n + \Delta t) = 0 \tag{95}$$

for all unstable modes i.

It is clear that at most one pair of unstable modes can be eliminated by an appropriate choice of $\mathcal{I}_c^n$. Therefore, the method may only work for ring lengths $L_2 < L < L_c$ (see Fig. 12). Therefore, we set the ring length to be the same as that used previously in TDAS control, $L = 9.94$ cm. For the complex conjugate unstable modes, $\mathbf{e}_2 = \mathbf{e}_3^*$ and $\mathbf{f}_2 = \mathbf{f}_3^*$ (recall that the real mode 1 has a zero growth rate). Since $\delta\mathbf{z}$ is real, we should have $\xi_2 = \xi_3^*$ at all times. Therefore, for the feedback current

$$\mathcal{I}_c^n \Delta t = \frac{\xi_2(t_n)}{\eta_2(x_0 - ct_n)} = \frac{|\xi_2(t_n)|}{|\eta_2(x_0 - ct_n)|} e^{i\phi(x_0, t_n)}, \tag{96}$$

where ϕ is the complex phase difference

$$\phi(x, t) = \arg(\xi_2(t)) - \arg(\eta_2(x - ct)), \tag{97}$$

eliminating mode 2 automatically eliminates mode 3 as well. One finds that ξ_2 and η_2 rotate in the complex plane with different angular speeds and in general have different complex phases (see Fig. 24a). Hence, the right-hand side of (96) is generally complex,

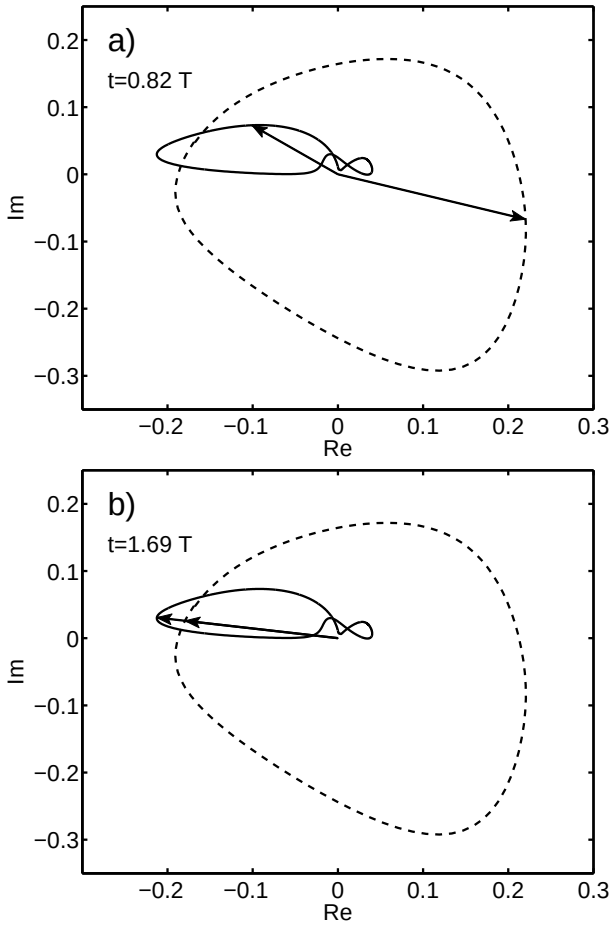

Figure 24: Trajectories followed in the complex plane by ξ_2 (dashed line) in the state of alternans and η_2 (solid line) over the time interval $[0, T_A]$, where $T_A \approx 1.72T$ is the period of alternans. Arrows are drawn to help identify the angles of ξ_2 and η_2 at a particular time instance. (a) Generically $\phi(x_0, t_0) \bmod \pi \neq 0$. (b) By an appropriate choice of x_0 and t_0 both (98) and (99) can be satisfied. Note that η_2 is shown rescaled by a factor of 2 to aid visualization.

while the left-hand side is always real. We must, therefore, choose x_0 and/or t_n such that the right-hand side is real; i.e.,

$$\phi(x_0, t_n) \bmod \pi = 0. \tag{98}$$

Equation (98) has an infinite number of solutions. This freedom can be used to perform some limited optimization [51]. In particular, we find that over one period of the oscillation, $|\xi_2|$ varies much less than $|\eta_2|$. Therefore, for the initial control stimulus, $n = 0$, the control current can be minimized by choosing x_0 and t_0 such

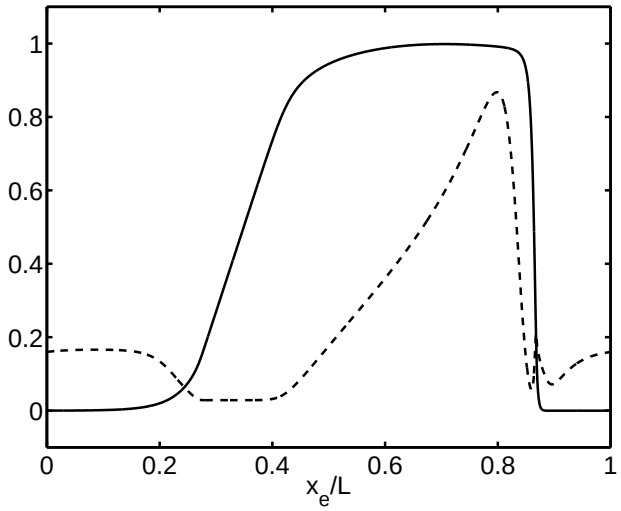

Figure 25: Transmembrane voltage u of the target state $\mathbf{z}_p$ (solid line) and $|f_2^u|$ (dashed line). Notice that the maximum of $|f_2^u|$ corresponds to the early part of the action potential plateau following depolarization.

that $|\eta_2(x_0 - ct_0)|$ achieves its largest value. Since $g(s)$ is a narrow Gaussian ($\omega \ll L$), $|\eta_2(x)| \approx |f_2^u(x)|$, where $f_i^u(x)$ is the voltage component of $\mathbf{f}_i$. We can, therefore, choose

$$(x_0 - ct_0) \bmod L = x_{\max}, \tag{99}$$

where $x_{\max} \approx 0.8L$ is the location at which $|f_2^u|$ achieves its maximum value (see Fig. 25). Similar arguments were used in Ref. [3] to determine where the current should be injected to suppress alternans-like dynamics of a spiral wave. From (98) we see that t_0 is a solution of $\arg(\xi_2(t_0)) = \arg(\eta_2(x_{\max})) + \pi k$ with some integer k and $x_0 = (x_{\max} + ct_0) \bmod L$. The solution corresponding to $k = 0$ is shown in Fig. 24b. At $t = t_0$ we have $x_e = x_0 - ct_0 = x_{\max}$, which means that it is optimal to apply the control current at the early plateau phase (see Fig. 25). This conclusion is consistent with the results of Ref. [51].

Fig. 26 shows the evolution of $\xi_2(t)$ leading to and following the initial control stimulus at $t_0 = 0.78T$. The effect of the feedback current was simulated by instantaneously changing $u(x, t_0)$ by $-j_0 \Delta t\, g(s(x - x_e(x_0 - ct_0)))$ with j_0 computed from (96), which corresponds to the limit $\Delta t \to 0$. One discovers that although $\xi_2 = \xi_3 = 0$ (to

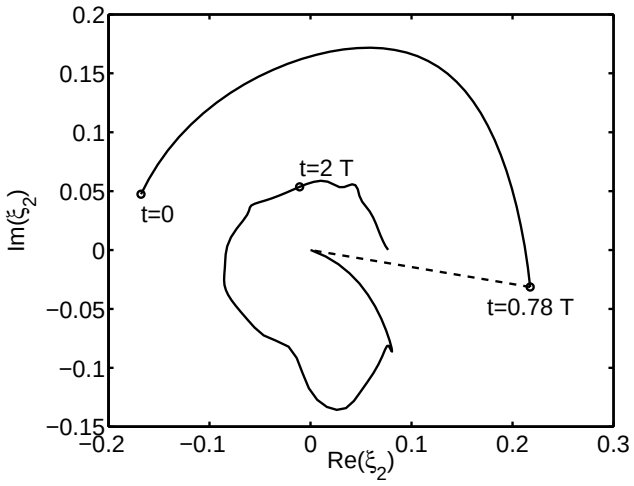

Figure 26: Trajectory followed by $\xi_2(t)$ in the complex plane before and after the application of a control stimulus $j_0 \Delta t$ at $t = 0.87T$. The dashed line indicates the instantaneous cancellation of ξ_2. The state at $t = 0$ is that of fully developed alternans (see Fig. 10).

numerical precision) following the control stimulus, both unstable modes quickly grow to a magnitude comparable to that preceding the current injection. This is due to the so-called control spillover effect [34]: the feedback that is aimed at suppressing the unstable modes will generically excite the modes that would be stable in the absence of feedback (e.g., modes 4, 5, etc.). The nonlinearities contained in the ionic model couple the dynamics of different modes, leading to a relatively quick regrowth of the unstable modes and re-emergence of the alternans.

One way to address this problem is by iterating the control current injections indefinitely. However, for the application of the second (and subsequent) control stimulus there is no longer the freedom to chose x_0 as it is impractical to move the electrode relative to the tissue. The feedback current should be injected through the electrode located at x_0 at time t_n satisfying (98). In general we will have $x_e(t_n) = (x_0 - ct_n) \bmod L \neq x_{\max}$ and hence $|\eta_2|$ may be significantly reduced compared to its maximum value. In particular, when the control electrode is located near a minimum of $|f_2^u|$ (the extreme case being $x \approx 0.35L$, as Fig. 25 shows) the control current magnitude will have to be increased by two orders of magnitude compared with the

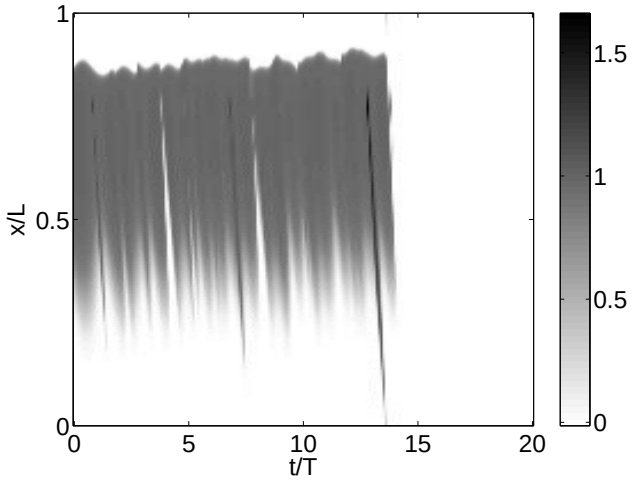

Figure 27: Evolution of the transmembrane voltage u under QISUM control for the ring of length $L = 9.94$ cm. The initial condition is the state of fully developed alternans shown in Fig. 10. The control method was turned off after the occurrence of conduction block.

optimal choice described previously. The need for an increased control stimulus is a signature of loss of controllability, a concept that we will discuss in more detail in Sect. 4.3.4. A large control current can alter the traveling wave up to a point where it looses its ability to propagate and vanishes (conduction block). This is indeed what we observed. We applied several control stimuli separated by a minimum time of T. This delay was introduced to allow the stable modes to relax following the previous control stimulus. Regardless of the choice of the phase difference (0 or π), conduction block was observed after the application of fewer than 10 control stimuli. Fig. 27 shows results obtained for the case in which the shortest interval $|t_n - t_{n-1}|$ between the control stimuli was chosen. Conduction block was observed at $t \approx 14T = 3.29$ s.

4.3.3.2 LQR control

The limitations of QISUM can be overcome by feedback control of the map (81). On each interval $[t_n, t_{n+1})$, $t_n \equiv nT$, $n = 0, 1, 2, ...$ we will assume the control current $\mathcal{I}_c(t)$, or, alternatively, $\mathcal{I}_c^n(t) = \mathcal{I}_c(t_n + t)$, $t \in [0, T)$, to be piecewise constant. Specifically, the interval $[0, T)$ is subdivided into l subintervals $S_k = [(k-1)\Delta T, k\Delta T]$, $k = 1, ..., l$,

of equal duration $\Delta T = T/l$, so that

$$\mathcal{I}_c^n(t) = \mathcal{I}^{n,k},\ t \in S_k. \tag{100}$$

Comparison of (100) with (86) indicates that in this case

$$\beta_k(t) = \begin{cases} 1, & t \in S_k \\ 0, & \text{otherwise,} \end{cases} \tag{101}$$

and $\nu_k^n = \mathcal{I}^{n,k}$ is the current during subinterval S_k. Substitution of (101) into (80) gives the corresponding expression for the matrix elements $B_{i,k}$. We will calculate the control input using the feedback law (89). The matrix K was calculated by the LQR method applied to the cost functional (92), which with the identification $\nu_k^n = \mathcal{I}^{n,k}$, becomes

$$\mathcal{G} = \sum_{n=1}^{\infty} \frac{1}{L^2} \|\delta \mathbf{z}(t_n)\|^2 + r_0 \sum_{n=1}^{\infty} \frac{1}{l} \sum_{k=1}^{l} (\mathcal{I}^{n,k})^2. \tag{102}$$

The LQR control scheme was verified by numerically integrating the evolution equation (40) using the same method, spatial mesh and time step as those used for QISUM control. We found LQR to to be capable of quickly suppressing alternans for an appropriate choice of parameters (m, l, x_0, and r_0). The evolution of the system in the co-moving reference frame is shown in Fig. 28. One finds that the feedback current computed using LQR successfully suppresses fully developed alternans (initial condition shown in Fig. 10) with the system dynamics approaching the target state.

In implementing LQR control we used $m = 9$ mode truncation. Increasing m had little effect on the performance. However, we did find that the performance depended noticeably on the position of the control electrode (relative to the position of the traveling pulse at times $t_n = nT$). For some values of x_0 conduction block took place, and the method therefore failed to drive the system to the target state. In the cases in which LQR was successful, the control time was found to depend significantly on the choice of x_0. In the end we selected x_0 to minimize the control time t_c. This value was chosen for all the calculations presented here.

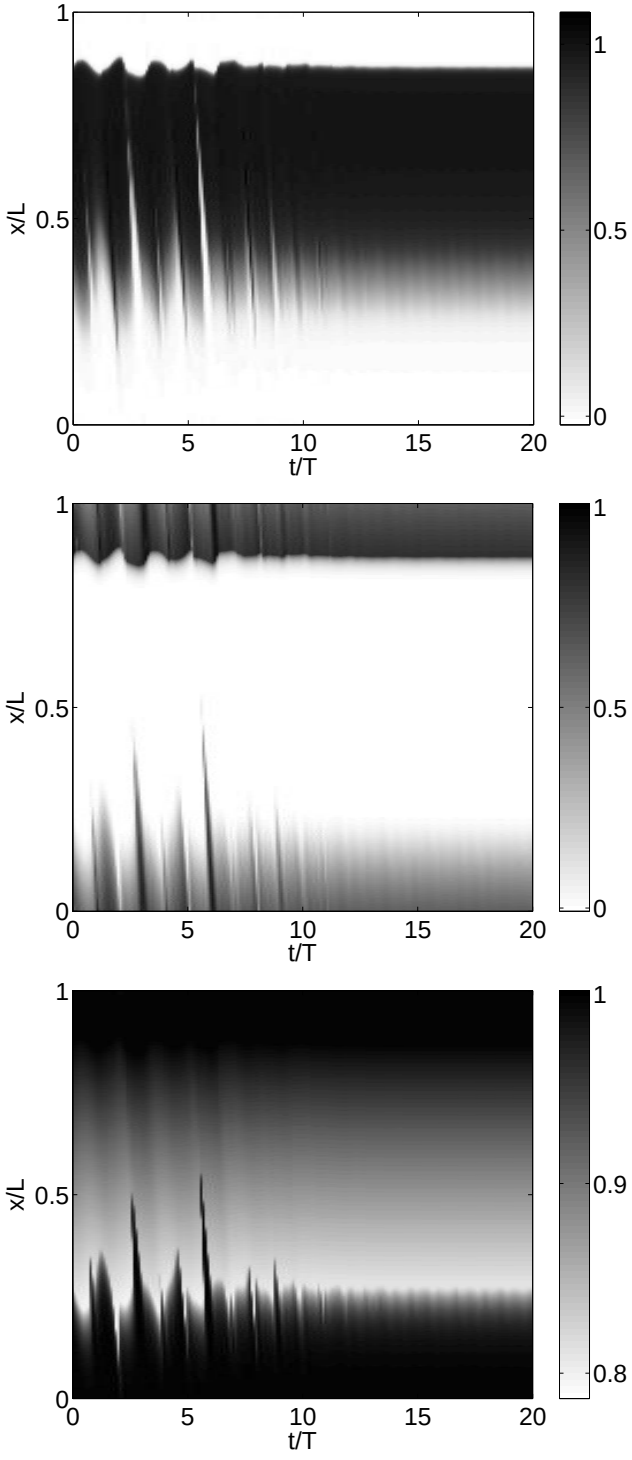

Figure 28: Evolution of the transmembrane voltage u under LQR control for the ring of length $L = 9.94$ cm. We used $l = 4$, with r_0 and x_0 set to the optimal values as described in the text. The initial condition is the state of fully developed alternans shown in Fig. 10.

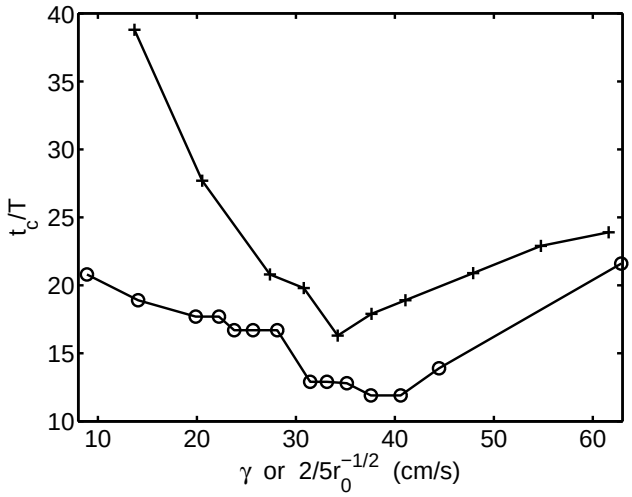

Figure 29: Control time as a function of the control parameters γ for TDAS (crosses) and $2/5r_0^{-1/2}$ for LQR (circles) with $l = 4$ subintervals.

To investigate the constraints on the number of subintervals l, we fixed $r_0 = 405$ ms^{2}cm^{-2} and subdivided each time interval $[t_n, t_{n+1}]$ into $l = 2^k$ subintervals with $k = 1, \cdots, 7$. For $l \leq 2$ the control current was found to produce conduction block. The control was successful for $l \geq 4$, so we set $l = 4$ in the rest of the calculations reported here. This corresponds to the "worst case scenario"; increasing l should further optimize control, thereby decreasing the control time and the control current magnitude and further reducing the likelihood of conduction block.

In order to explore how the LQR control performs depending on the weight given to the magnitude of control current vs. the convergence speed, we computed the control time t_c as a function of r_0. As Fig. 29 shows, the control time achieves its minimum value of $t_c \approx 11.9T = 2.80$ s for $r_0 \approx 111$ ms^{2}cm^{-2} and increases slightly for values of r_0 either greater or less than the optimal value. This time is shorter than that for TDAS. This is the first clear indication that by using more extensive information about the system state and dynamics it is possible to design a control scheme with superior performance.

Fig. 30 shows the control current as a function of time for LQR and TDAS

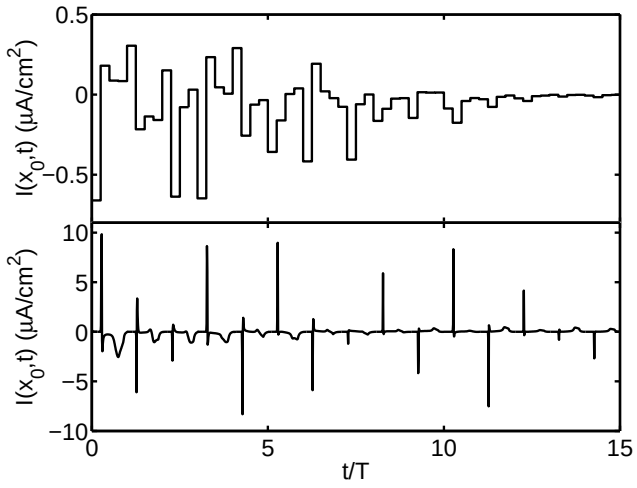

Figure 30: Control current density at the location of the control electrode ($I(x_0, t)$ as seen in the stationary reference frame) as a function of time for TDAS.

for the values of r_0 and γ producing the smallest t_c. For TDAS the current shows pronounced spikes whose absolute values are about an order of magnitude bigger than the maximum absolute value of the current for LQR. Large currents, such as those applied during the initial stages of control, can lead to electroporation of the tissue surrounding the electrode. Electroporation is characterized by rupture of cell membranes as a result of induced high transmembrane voltage [2, 61]. Besides the tissue damage, the associated changes in the local dynamics can render any feedback control ineffective.

It should be noted that the convergence of the alternans amplitude $\delta W(t)$ to zero is non-monotonic, but rather is characterized by strong initial fluctuations. The changes in the action potential shape produced by LQR control during this initial stage (shown in Fig. 31) could be interpreted as induced dispersion of repolarization. For a longer (shorter) pulse, the feedback current repolarizes (depolarizes) the tissue, effectively shortening (lengthening) the pulse.

Several studies of uncontrolled cardiac dynamics have found that dispersion of repolarization is a condition that can lead to conduction block [83, 67, 29]. As we

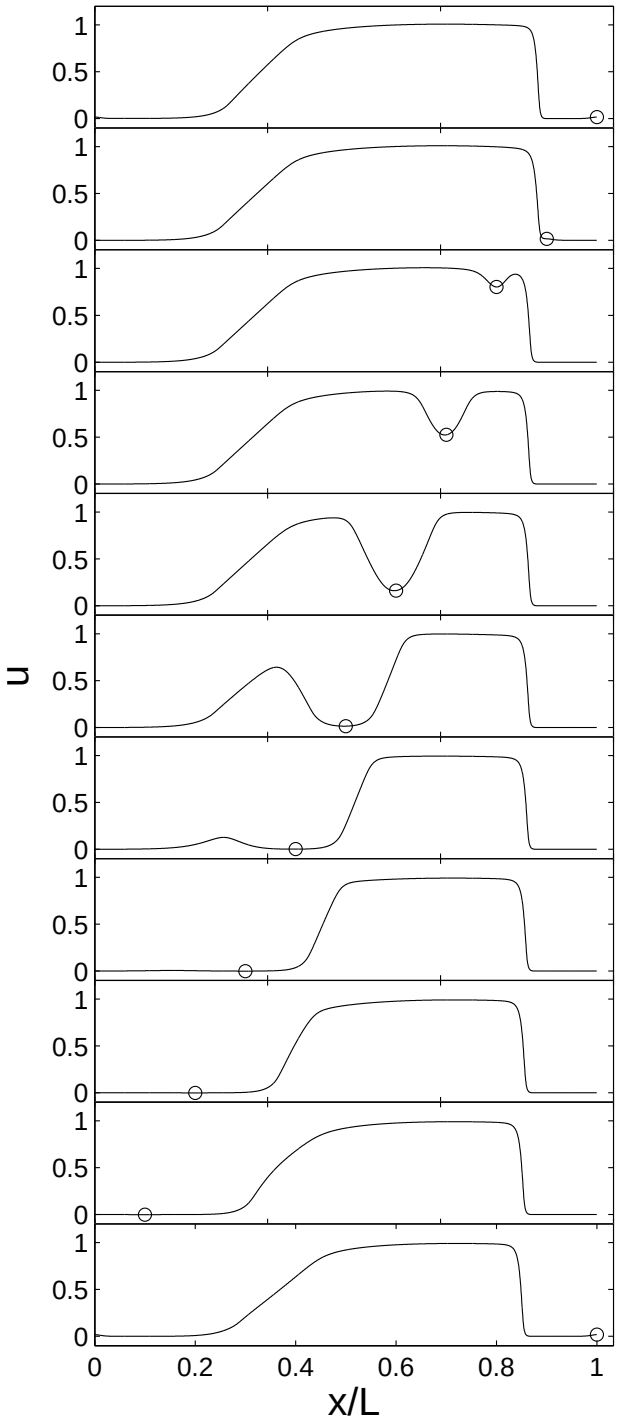

Figure 31: Transmembrane voltage u during LQR control (same data as for Fig. 28) for t from $5.1T$ (top panel) up to $6.1T$ (bottom panel) with increments of $0.1T$. The circle on each panel indicates the value of u at the location of the control electrode (it moves backward in the co-moving reference frame).

have shown previously, for $l \leq 2$ (when the control current is not allowed to vary sufficiently frequently) LQR does indeed fail by inducing conduction block. However, when the control current profile is sufficiently optimized (for $l \geq 4$), LQR succeeds in suppressing alternans without inducing conduction block. This fact indicates there is no direct link between the alterations of the action potential shape presented in Fig. 31 and conduction block. In other words, the intuition gained in studies of open-loop (uncontrolled) systems cannot be generalized in a straightforward manner to closed-loop (controlled) systems.

4.3.3.3 Robustness of LQR under parameter uncertainty

A source of concern in implementing model-based control is the unavoidable mismatch between the true dynamics and the predictions of a model. A controller that is able to achieve its goal even when the model is imperfect or when the model parameters are not known exactly is said to be robust under model uncertainty. The robustness of LQR control can be tested, for instance, by assuming that although the Fenton-Karma model provides an accurate representation of the real dynamics, the values of its parameters are not known precisely (parameter uncertainty). An example of such situation is when some parameters fluctuate in time. For instance, it is well known that the interbeat interval in isolated pacemaker cells can vary as much as 2% as a result of the stochastic behavior of the membrane ionic channels [89]. This stochastic behavior will also affect various parameters of the model. We tested the performance of LQR in a hypothetical situation in which the "estimated" values of parameters used for computing the feedback were different from the "true" values used to evolve the system state.

In practice the model parameters are estimated by fitting the model predictions to experimental measurements. One of the most easily accessible measurements is the wave speed c of the target state (36). Therefore, we choose the estimated values

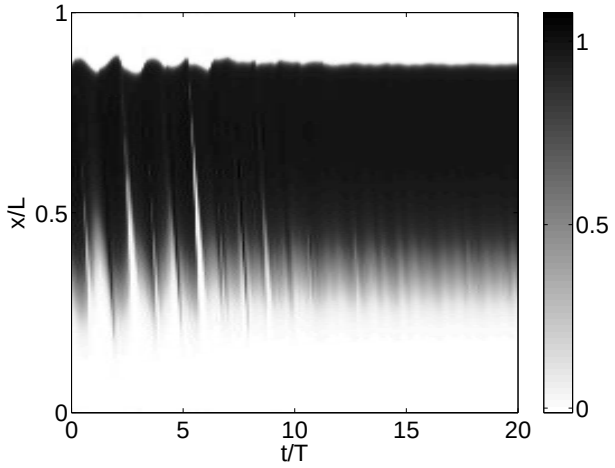

Figure 32: Evolution of the transmembrane voltage u under LQR control computed using estimated parameters for the ring of length $L = 9.94$ cm. Parameters l, r_0 and x_0 are as in Fig. 28. The initial condition is the state of fully developed alternans (see Fig. 10).

in such a way that the speed c was the same (up to six significant figures) for the estimated set and the true set of parameters. Specifically, we chose $\tau_r = 55.53$ (all times are in milliseconds) and $\tau_{\rm si} = 50$ for the estimated set of values, compared with $\tau_r = 50$ and $\tau_{\rm si} = 44.84$ for the true set of values, with the rest of the parameters chosen to be the same as in Sect. 2.4. That corresponds to a mismatch of about 10% between the estimated and true values of both parameters.

Fig. 32 illustrates the performance of feedback control computed using the estimated values of parameters. Of course, complete suppression of the perturbation $\delta\mathbf{z}$ cannot be attained, since the target state calculated from the estimated set of parameter values is not the true target state. Nonetheless, after 30 periods control reduces the amplitude of alternans to 5% of the amplitude of fully-developed alternans, thereby illustrating that LQR is robust under parameter uncertainty for the model considered.

4.3.4 Control of alternans in the open fiber

Here we consider a stroboscopic section $t_n = \tau + nT$, that does not necessarily coincide with the pacing stimulus ($\tau = 0$). This will allows us to explore the effect of control stimuli applied at arbitrary times. Therefore we need to generalized the results obtained in Sects. 3.2.2 and 4.3.1.2 to this case. By a line of reasoning similar to that presented in Sect. 3.2.2 one can show that, in the absence of control current, the perturbation evolves according to

$$\delta\mathbf{z}(t_{n+1}) = U(\tau + T, \tau)\delta\mathbf{z}(t_n), \tag{103}$$

where $U(\cdot, \cdot)$ is the time evolution operator of the linearized dynamics defined in Sect. 3.2.2.

The stability of $\mathbf{z}_p$ is determined by the eigenvalues λ_i of $U(\tau + T, \tau)$,

$$U(\tau + T, \tau)\mathbf{e}_i(\tau) = \lambda_i \mathbf{e}_i(\tau), \tag{104}$$

where $\mathbf{e}_i(\tau)$ is the corresponding eigenfunction. It can be shown that λ_i are independent of τ and that the eigenvectors of $U(\tau + T, \tau)$ for arbitrary τ can be computed as $\mathbf{e}_i(\tau) = U(\tau, 0)\mathbf{e}_i(0)$ using the eigenvectors for $\tau = 0$.

By reviewing the steps followed in the derivation of (88) we see that for $\tau \neq 0$,

$$B_{ik} = \left\langle \mathbf{f}_i(\tau), \int_\tau^{\tau+T} \beta_k(t) U(\tau + T, t)\mathbf{g}(x - x_c)dt \right\rangle \tag{105}$$

For simplicity we will assume that the control current consists of a brief pulse of duration $\Delta \ll T$ applied at the beginning of the interval $[\tau, \tau + T]$. This current corresponds to a single, Dirac-delta-like function $\beta_k(t)$,

$$\beta_1(t) = \delta_\Delta(t - \tau), \tag{106}$$

$$\delta_\Delta(t) = \begin{cases} 1/\Delta, & t \in [-\Delta/2, \Delta/2], \\ 0, & \text{otherwise} \end{cases} \tag{107}$$

In this case the single control parameter ν_1^n corresponds to the total charge q^n injected by the electrode. Substituting (106) into (105), and taking the limit $\Delta \to 0$, gives

$$B_{i1} = \langle\, \mathbf{f}_i(\tau),\, U(\tau + T, \tau)\mathbf{g}(x - x_c)\,\rangle \tag{108}$$

$$= \lambda_i \,\langle\, \mathbf{f}_i(\tau),\, \mathbf{g}(x - x_c)\,\rangle \tag{109}$$

$$\approx \lambda_i \, f_i^u(x_c, \tau). \tag{110}$$

where in the last step we used the fact that $g(x)$ is a narrow Gaussian.

The evolution equation of a single modal amplitude,

$$\xi_i^{n+1} = \lambda_i \xi_i^n - B_i q^n \tag{111}$$

(we use the notation $B_i = B_{i1}$ for simplicity), suggests an interesting interpretation for the adjoint eigenfunctions. When $B_i \approx -\lambda_i f_i^u(x_c, \tau) = 0$ for an unstable mode i, the control current has no effect on the dynamics of that mode (mode i becomes *uncontrollable*). Hence the instability cannot be suppressed, regardless of how the control current is chosen. Conversely, the larger $|f_i^u(x_c, \tau)|$ is, the smaller the control current should be. The structure of the adjoint eigenfunctions therefore determines where the control electrode(s) should be placed and how the timing of the control impulse(s) should be chosen. A similar result was obtained for the ring geometry (Sect. 4.3.3.1).

For instance, Fig. 33 shows the absolute value of the adjoint eigenfunctions for the four leading modes. Modes $i = 1, 2$ are unstable. All other modes, in particular $i = 3, 4$, are stable. PIA control corresponds to colocated pacing and controlling electrodes, $x_c = x_p$, and $\tau = 0$ and while $|f_1^u(x_p, 0)|$ is moderately large (the leading unstable mode is controllable), $|f_2^u(x_p, 0)|$ is very small, indicating that PIA control has virtually no effect on the dynamics of the second unstable mode (the subleading unstable mode is essentially uncontrollable). In this situation, control is expected to fail regardless of how the control current is chosen. Although we have not verified this

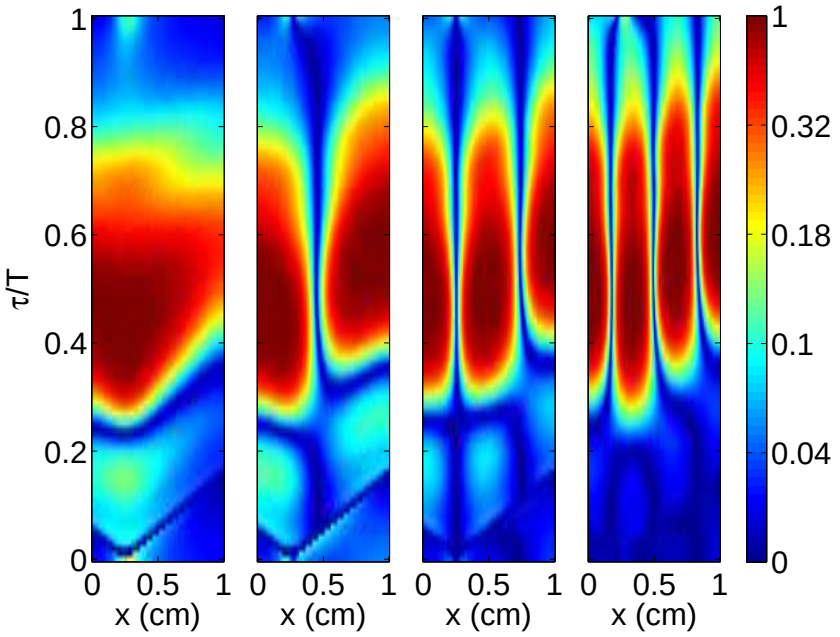

Figure 33: $|f_i^u(x,\tau)|$ for the four leading modes. From left to right, $i = 1, 2, 3, 4$. $L = 1$ cm and $T = 210$ ms.

for all values of L and T, this observation likely explains the fact that PIA control breaks down whenever the second unstable mode appears, as a quick comparison of our Fig. 14 with Fig. 21 illustrates.

While it is tempting to choose $x_c = x_p$, so that the same electrode can be used for both pacing and control (the choice we follow in the remainder of this study), this requires that the control impulse be delivered much later than the pacing impulse. For instance, Fig. 33 suggests that the optimal interval is $0.3T < \tau < 0.7T$, where both $|f_1^u(x_p,\tau)|$ and $|f_2^u(x_p,\tau)|$ take nearly maximal values.

Once x_c and τ have been selected, the feedback stabilizing the target state can be computed using any one of a number of standard control-theoretic methods. By writing (111) as

$$\xi_i^{n+1} = \lambda_i \left[\xi_i^n + \langle \mathbf{f}_i(\tau), \mathbf{g}(x - x_c)\rangle \; q^n\right], \tag{112}$$

it becomes evident that modes such that $|\lambda_i| \ll 1$ will decay quickly regardless of how the control stimulus q^n is chosen. Hence, these quickly decaying modes, which

constitute an infinite set, need not be considered for the feedback control problem. For the remaining m modes, the maps (111) can be gathered in a single matrix equation as

$$\boldsymbol{\xi}^{n+1} = A\boldsymbol{\xi}^n + Bq^n, \tag{113}$$

where $\boldsymbol{\xi}^n = [\xi_1^n, \xi_2^n, ..., \xi_m^n]^{\mathcal{T}}$, A is a diagonal matrix with elements $A_{ii} = \lambda_i$ and B is a vector with elements B_i. The set of m retained modes must contain at least the unstable modes. The number of additional, stable modes that is necessary to include depends on other considerations such as state reconstruction, as discussed below. We calculated the control current using the feedback law (89). However, in order to illustrate that the method works even when the control objective is not optimal, we used pole placement for the calculation of the feedback gain K, instead of LQR.

4.3.4.1 State reconstruction

In experiment, the mode amplitudes ξ_i^n will not be directly accessible. However, it is possible to determine them from recordings of the transmembrane voltage by a few electrodes using an auxiliary dynamical system known as an *observer* or *estimator* in control theory. Similar to the PIA implementation in Ref. [21], we will use a single electrode to record the voltage, but will use one measurement per pacing interval in contrast with PIA, which requires continuous measurement of u to determine the APD. An electrode of finite spatial extent and centered at x_o can be modeled by writing the recorded voltage as

$$v^n = \int g(x - x_o)u(x, t_n)dx. \tag{114}$$

We also assume that the voltage describing the normal rhythm

$$v_0 = \int g(x - x_o)u_p(x, \tau)dx \tag{115}$$

is unknown and needs to be determined.

From the definition of $\delta\mathbf{z}$ and (64) we have

$$v^n = v_0 + \sum_{i=1}^{\infty} \xi_i^n C_i, \tag{116}$$

where $C_i = \langle \mathbf{e}_i(\tau), \mathbf{g}(x - x_o) \rangle \approx e_i^u(x_o, \tau)$. Truncating (116) to m modes and rewriting it in matrix form yields

$$v^n = C^\dagger \mathbf{r}^n, \tag{117}$$

where $C = [C_1, \cdots, C_m, 1]$ and $\mathbf{r}^n = [\xi_1^n, \cdots, \xi_m^n, v_0]$ is the vector of unknowns to be determined. Once again, (116) allows an intuitive interpretation. Whenever $C_i \approx e_i^u(x_o, \tau) = 0$, the measured voltage becomes independent of the mode amplitude ξ_i^n (mode i becomes *unobservable*). This means that ξ_i^n cannot be determined regardless of the procedure used to extract it. If the unobservable mode is unstable, we cannot expect the feedback to suppress it either, so that observability of unstable modes imposes additional restrictions on the timing τ of voltage recordings and the position x_o of the recording electrode. (In principle, τ can be chosen independently for observation and control; in this study we choose τ to be the same for simplicity.)

As Fig. 34 illustrates, we can also use the pacing electrode to record the voltage, $x_o = x_p$. With this choice, $\tau = 0$ makes the subleading unstable mode both essentially uncontrollable *and* unobservable. From the observability standpoint, the optimal choice of τ in this case corresponds to the range $0.5T < \tau < 0.9T$, where both $|e_1^u(x_p, \tau)|$ and $|e_2^u(x_p, \tau)|$ take nearly maximal values. On the other hand, the middle of the fiber is arguably the worst location for the recording electrode. Setting $x_o \approx 0.48$ makes mode 2 essentially unobservable regardless of the choice of τ. Similarly, Fig. 33 shows that choosing $x_c \approx 0.48$ makes mode 2 essentially uncontrollable for almost any τ. In this study we chose $\tau = 0.54T$, which falls in the optimal range with respect to both observability and controllability of the two unstable modes for almost any choice of x_c and x_o. We set $x_o = 0.9$ cm, since this position minimizes the effect of nonlinearities on the observer as discussed below.

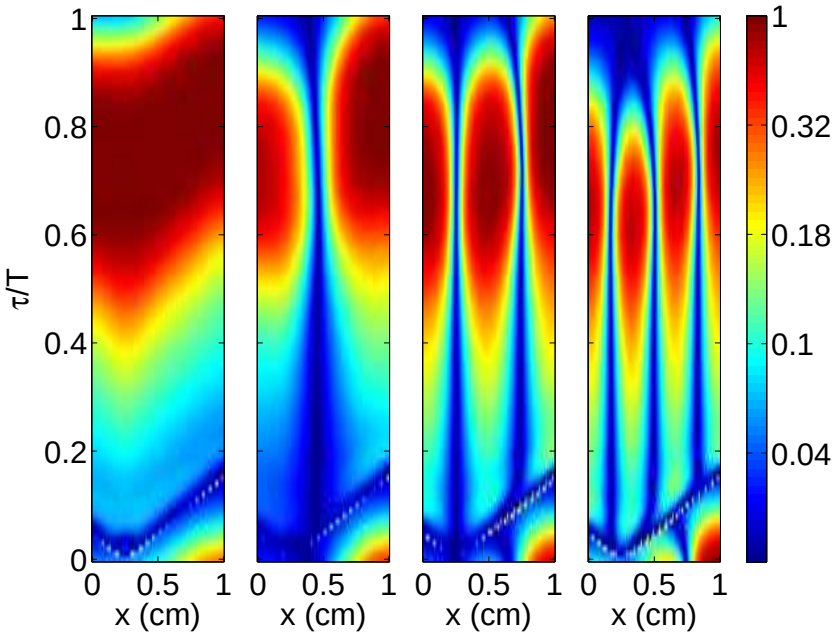

Figure 34: $|e_i^u(x,\tau)|$ for the four leading modes. From left to right $i = 1, 2, 3, 4$. $L = 1$ cm and $T = 210$ ms.

We used the Luenberger observer [91] to reconstruct the mode amplitudes ξ_i^n from the voltage recordings $v^n, v^{n-1}, \cdots$. Let us define

$$\tilde{\mathbf{r}}^{n+1} = \widetilde{A}\tilde{\mathbf{r}}^n + \widetilde{B}q^n + H\left[v^n - C^\dagger \tilde{\mathbf{r}}^n\right], \tag{118}$$

where $\widetilde{A}$ is a diagonal matrix with $\widetilde{A}_{ii} = \lambda_i$ for $i = 1, \cdots, m$ and $\widetilde{A}_{ii} = 1$ for $i = m+1$ while $\widetilde{B}_i = B_i$ for $i = 1, \cdots, m$ and $\widetilde{B}_i = 0$ for $i = m+1$. Then $\tilde{\mathbf{r}}^n = [\tilde{\xi}_1^n, \cdots, \tilde{\xi}_m^n, \tilde{v}_0^n]$ is an estimate of $\mathbf{r}^n$ in the sense that the difference $\tilde{\mathbf{r}}^n - \mathbf{r}^n$ converges to zero asymptotically provided H is chosen such that $\widetilde{A} - HC$ is stable. This is also done using pole placement here.

As an example, Table 1 shows the controller poles, Ω_i^c, and observer poles, Ω_i^o, used for the compensator control displayed in Fig. 36, as well as the eigenvalues λ_i of matrix A, and the eigenvalues of matrix $\widetilde{A}$ (diagonal elements $\widetilde{A}_{ii}$), included for reference purposes.

We also need to choose the initial estimate, $\tilde{\mathbf{r}}_1$. It was found that, for the control protocol used (discussed below), the leading modal amplitude was initially

Table 1: Controller poles, Ω_i^c, and observer poles, Ω_i^o, for the compensator control shown in Fig. 36. The eigenvalues of matrices A and $\widetilde{A}$, λ_i and $\widetilde{A}_{ii}$ respectively, are included for reference purposes.

i	λ_i	Ω_i^c	$\widetilde{A}_{ii}$	Ω_i^o
1	-1.38	-0.8	-1.38	-0.6
2	-1.04	-0.79	-1.04	-0.59
3	–	–	1	0.6

dominant over the remaining ones, $|\xi_1^1| \gg |\xi_i^1|,\ i = 2, 3, ...$ Based on this, we set $\tilde{\xi}_i^1 = 0,\ i = 2, 3, ...$ With the goal of finding approximate values of ξ_1^1 and v_0, we avoided applying control during the first period. From (116) and (111), we see that under these conditions

$$v^1 \approx v_0 + \xi_1^1 C_1, \tag{119a}$$

$$v^2 \approx v_0 + \lambda_1 \xi_1^1 C_1. \tag{119b}$$

Hence, we choose $\tilde{\xi}_1^1$ and $\tilde{v}_0^1$ such that the linear system (119) is satisfied.

Combining the controller (113) with the observer (118) yields a single-input single-output (SISO) control procedure (known as a *compensator*) that could easily be applied in an experimental setting. To illustrate its performance we implemented control of the full nonlinear equation (6).

In order to directly compare the performance of the compensator with PIA control we used the same electrode for pacing and feedback and followed the protocol outlined in [21]. Starting with $T = 280$ ms where the normal rhythm is stable, T was decreased by 5 ms followed by 200 pacing impulses (with the feedback turned on) after which the cycle was repeated. We find that, for a fiber of length $L = 1$ cm, PIA control is able to suppress alternans only for the values of T characterized by one unstable mode (see Fig. 14). As we have explained previously, this is likely due to the fact that the second unstable mode becomes uncontrollable when the current impulse is localized near $\tau = 0$, as is the case for PIA.

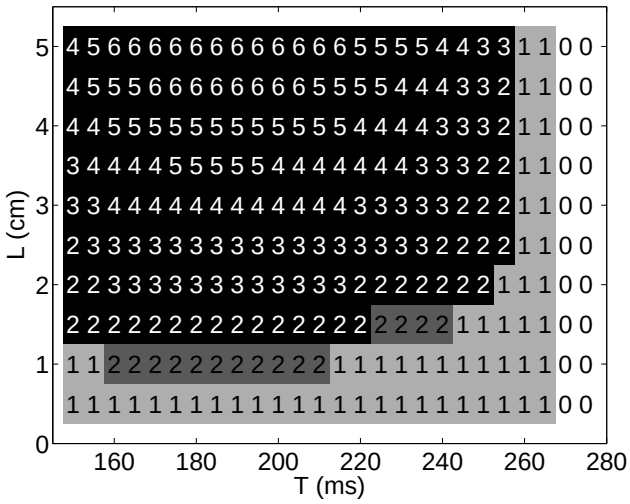

Figure 35: Comparison of the regions in the (L, T) parameter space where PIA and model-based control successfully suppress alternans. Light gray: PIA and model-based control both succeed. Dark gray: PIA control fails but model-based control succeeds. Black: PIA control fails and the model-based control has not been verified. The number of unstable eigenmodes is displayed at each grid point.

In contrast, the choice $\tau = 0.54T$ yielding controllable and observable dynamics enabled the compensator to successfully suppress alternans, for the same fiber length, in the whole range of T values, regardless of the number of unstable modes (see Fig. 35). When the recording electrode was located at $x_o = 0.9L = 0.9$ cm, the truncation to two unstable modes ($m = 2$) was sufficient for successful control. For $x_o = x_p = 0.25$ cm, two additional (stable) modes had to be included for a total of $m = 4$ modes. Fig. 36 shows the max-norm of the difference in successive APDs, $P_n = \max_x |\mathrm{APD}_n(x) - \mathrm{APD}_{n-1}(x)|$, for a particular value of T. P_n approaches zero after about 50 pacing intervals, indicating convergence to the normal rhythm. The compensator with also successfully suppressed alternans for a longer fiber with $L = 1.5$ cm and T from 225 to 240 ms, when the observing electrode was placed at $x_o = 0.9L = 1.35$ cm (see Fig. 35).

When m is chosen too low, control with colocated controlling and observing electrodes fails. This lead us to explore the effect of different positions of the observing

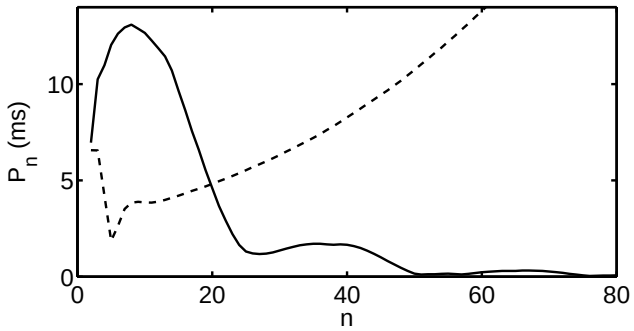

Figure 36: Evolution of P_n (see text) with compensator control (solid line) and PIA control (dashed line) for $L = 1$ cm, $T = 205$ ms, $m = 2$, and $x_o = 0.9$ cm.

electrode x_o and different number of modes m on the compensator performance. From (64) and (53) we see that

$$\xi_i = \langle \mathbf{f}_i, \delta\mathbf{z} \rangle \,. \tag{120}$$

Note that (120) is a purely geometrical relation and therefore is valid independently of any assumptions on the dynamics of $\delta\mathbf{z}$. In particular, (120) holds even in the nonlinear regime. Fig. 37 shows the actual modal amplitudes, ξ_i^n (calculated with (120)), and the estimated ones, $\tilde{\xi}_i^n$, for $L = 1$ cm, $T = 210$ ms, $m = 2$ and the observing electrode close to the right end of the fiber, $x_o = 0.9$ cm. We can see that, except for the first mode around $n = 5$, the estimated modal amplitudes follow closely the actual ones indicating effective state estimation. In contrast, when the observing electrode is colocated with the pacing one, $x_o = x_p = 0.25$ cm (Fig. 38), significant differences are observed between ξ_i^n and $\tilde{\xi}_i^n$. This mismatch diminishes the efficiency of control: while for $x_o = 0.9$ cm the perturbation has been decreased considerably at $n = 25$, for $x_o = 0.25$ cm it is still significant at that time. Moreover, ξ_i^n and $\tilde{\xi}_i^n$ both follow irregular paths that suggests an important discrepancy between the actual dynamics and the one assumed by the compensator. However, as Fig. 39 shows when the number of modes is increased from $m = 2$ to $m = 4$, efficient control is attained again. This proves that the loss of accuracy in the description of the dynamics for $x_o = 0.25$ cm is due at least partially to truncation effects. Additionally, in order

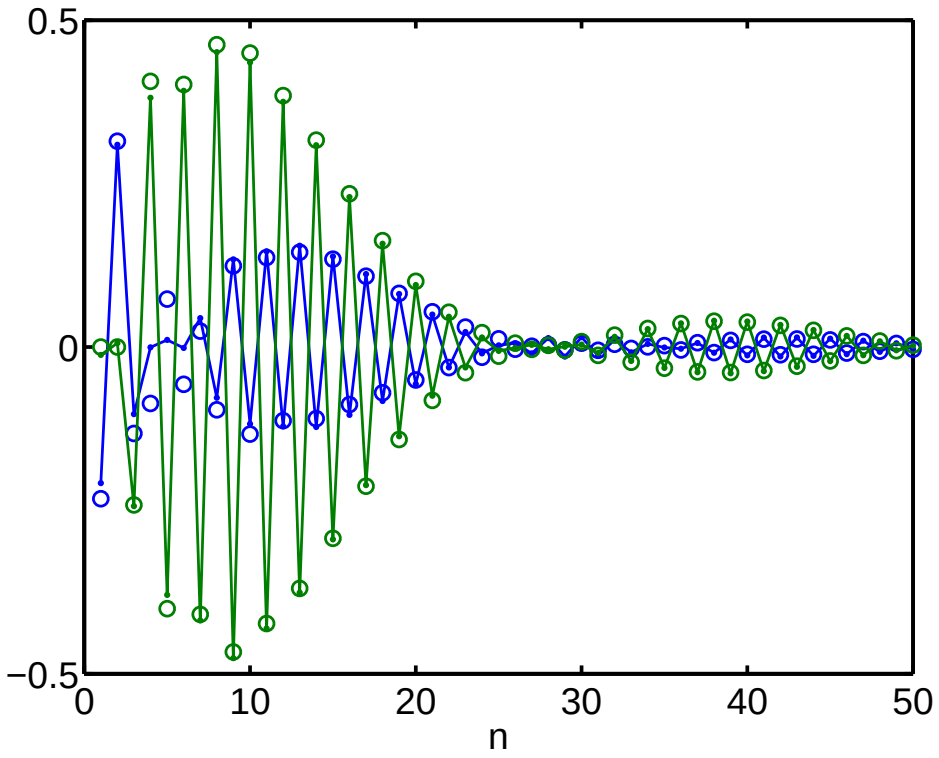

Figure 37: Actual and estimated modal amplitudes (ξ_i^n and $\tilde{\xi}_i^n$, respectively) during compensator control for $L = 1$ cm, $T = 210$ ms, $x_o = 0.9$ cm and $m = 2$. The dots joined by solid lines correspond to the actual amplitudes while the open circles correspond to the estimated ones. The color code is $i = 1$ (blue) and $i = 2$ (green).

to probe the effect of nonlinearities, we tested the compensator for $m = 2$, but with the perturbation manually decreased by a factor of 10 (Fig. 40). More exactly, if $\mathbf{z}_{\text{in}}$ denotes the initial condition used in Figs. 37 to 39, then the initial condition used in Fig. 40 is $\mathbf{z}_p + (\mathbf{z}_{\text{in}} - \mathbf{z}_p)/10$. For the decreased perturbation (Fig. 40), a better agreement between ξ_i^n and $\tilde{\xi}_i^n$ and a more regular dynamics are observed compared with Fig. 38. This shows that nonlinear effects also contribute to the discrepancy between the assumed and actual dynamics.

Similar analysis can be used to understand the failure of PIA control illustrated in Fig. 36. Fig. 41 shows the evolution of the modal amplitudes during PIA control for $T = 205$ ms and $L = 1$ cm, with the normal rhythm for $T = 210$ ms taken as the initial condition. Note that PIA initially produces a considerable reduction of ξ_1^n. In

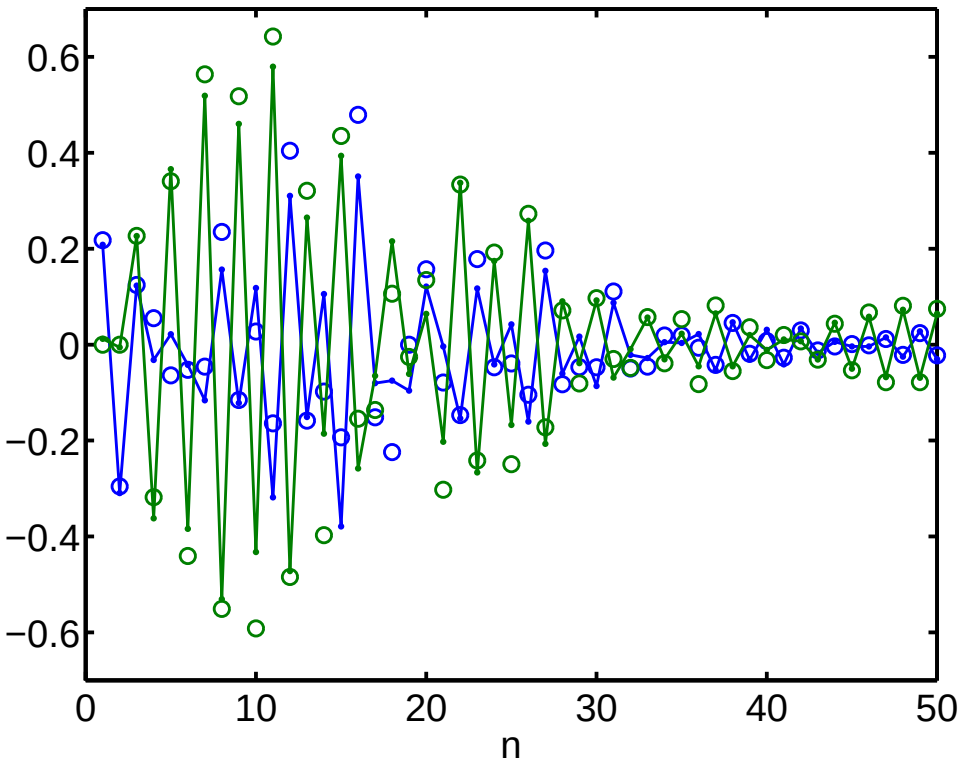

Figure 38: Actual and estimated modal amplitudes (ξ_i^n and $\tilde{\xi}_i^n$, respectively) during compensator control for $L = 1$ cm, $T = 210$ ms, $x_o = 0.25$ cm and $m = 2$. The dots joined by solid lines correspond to the actual amplitudes while the open circles correspond to the estimated ones. The color code is $i = 1$ (blue) and $i = 2$ (green).

contrast, after a few initial periods, the evolution of ξ_2^n follows closely that expected in the perfectly linear regime and in the absence of control (red circles). This suggest that the type of control stimuli applied by PIA does not affect the second modal amplitude. This supports our previous conclusion in the sense that with respect to PIA control the second mode is uncontrollable. Also note that, after $n = 15$, the growth of the second modal amplitude is accompanied by the growth of the first one. This correspondence is possibly due to nonlinear coupling between these two modal amplitudes, with mode 1 slaved by mode 2.

The compensator control method presented here can be generalized to longer fibers. Fig. 42 compares the spectra corresponding to $L = 1$ cm and $L = 3$ cm ($T = 185$ ms in both cases). Note that the leading eigenvalue is nearly the same

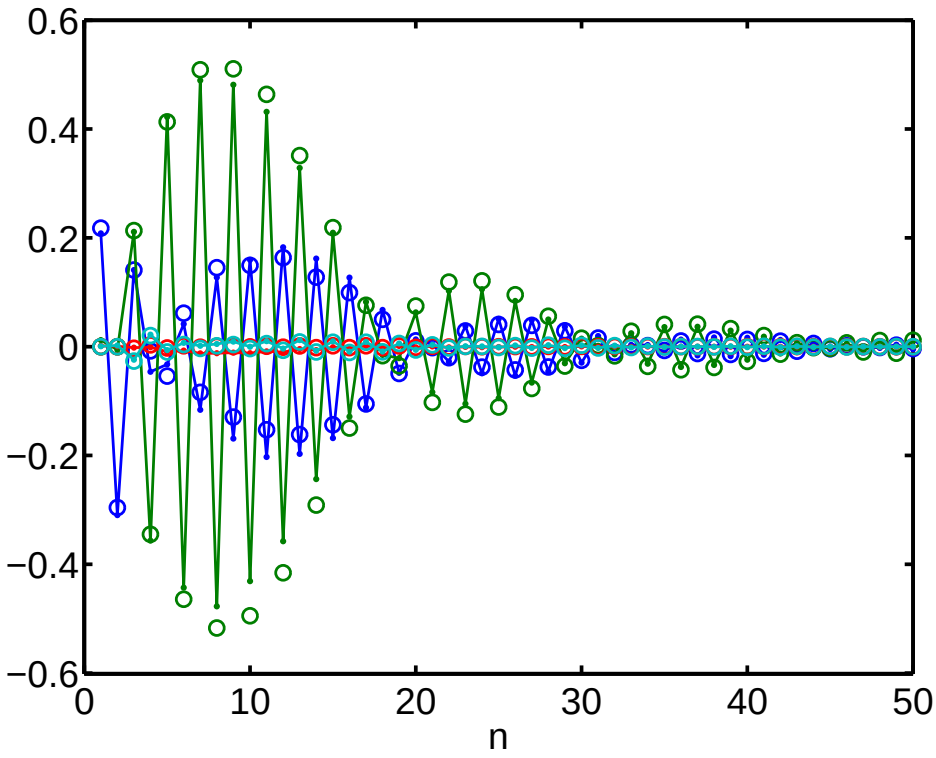

Figure 39: Actual and estimated modal amplitudes (ξ_i^n and $\tilde{\xi}_i^n$, respectively) during compensator control for $L = 1$ cm, $T = 210$ ms, $x_o = 0.25$ cm and $m = 4$. The dots joined by solid lines correspond to the actual amplitudes while the open circles correspond to the estimated ones. The color code is $i = 1$ (blue), $i = 2$ (green), $i = 3$ (red) and $i = 4$ (cyan).

for both lengths and that the density of eigenvalues (number of eigenvalues per unit length of the real axis) is directly proportional to the length. This behavior was observed for other fiber lengths as well when the pacing period was kept constant. This indicates that the leading eigenvalue is determined mainly by the pacing period. One can set as a rule of thumb that only eigenvalues with $|\lambda_i| > 0.1$ (precisely those plotted) need to be considered in the compensator (the remaining ones decay quickly). According to this rule we would need to retain 10 modes for the 3 cm fiber, while only 4 modes would be required for the 1 cm fiber. This is consistent with the results presented above concerning control of the 1 cm fiber (Figs. 37 to 40).

Fig. 43 shows $|f_i^u(x,\tau)|$ for the 8 leading modes for $L = 3$ cm. For all of them, $|f_i^u(x,\tau)|$ has a maximum close to the left end ($x = 0$) at $\tau \approx 0.5T$. These are the

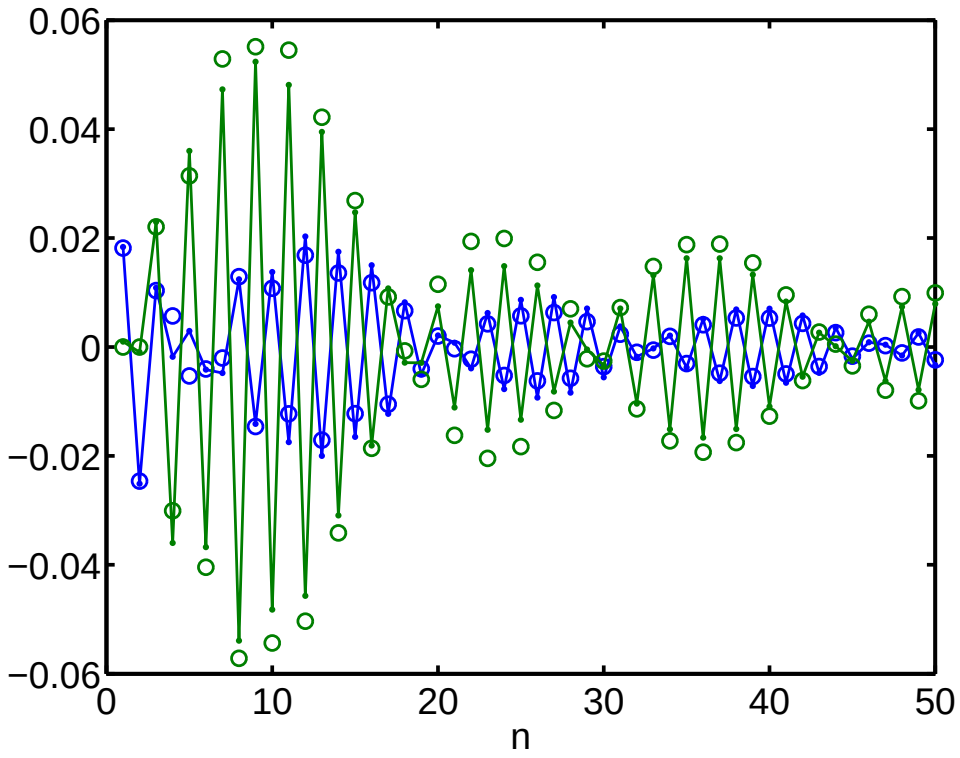

Figure 40: Actual and estimated modal amplitudes (ξ_i^n and $\tilde{\xi}_i^n$, respectively) during compensator control for $L = 1$ cm, $T = 210$ ms. $x_o = 0.25$ cm and $m = 2$. The initial perturbation was decreased by a factor of 10 compared with Fig. 38. The dots joined by solid lines correspond to the actual amplitudes while the open circles correspond to the estimated ones. The color code is $i = 1$ (blue) and $i = 2$ (green).

optimal location and time for the control stimulus. The optimal location for control at the left end is an expected result given that the information flows along the fiber in the same direction as the action potential, away from the pacing electrode, that is, from left to right. The optimal time for control corresponds to the repolarization phase of the action potential, in agreement with the results for single cells reported in [51].

Fig. 44 shows $|e_i^u(x,\tau)|$ for the 8 leading modes for $L = 3$ cm. For $i = 1$, the maximum of $|e_i^u(x,\tau)|$ occurs at $x = 0$ and $\tau \approx 0.7T$. However, for the remaining modes, $i = 2, 3, ..., 8$, the maximum is found at $x = L$ (the right end of the fiber) and $\tau \approx 0.3T$. These are the optimal times and locations for observation of the respective modes. The fact that, except for the first mode, the optimal location for observation

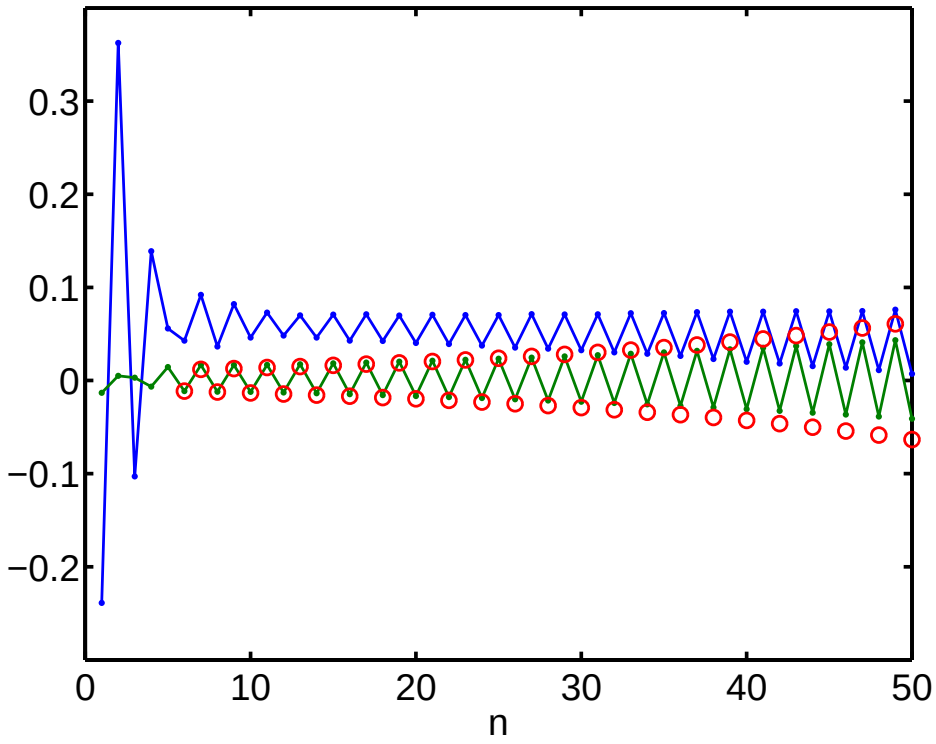

Figure 41: Modal amplitudes ξ_1^n (blue) and ξ_2^n (green) during PIA control for $L = 1$ cm and $T = 205$ ms. The initial condition is the normal rhythm for $T = 210$ ms. The red circles correspond to $\lambda_2^{(n-6)}\xi_2^6$, which is the evolution that the second modal amplitude would follow in the absence of control and in the perfectly linear regime.

is the at right end is again a consequence of the flow of information from left to right. Although $|e_1^u(x,\tau)|$ is not maximal at this time and location, it is substantially different from zero which suggest that it might be possible to observe mode $i = 1$ too if the voltage is recorded at this time and location. However, when implementing control in the evolution equation (6) (which we have not done for $L = 3$ cm yet) nonlinear effects and noise might render mode $i = 1$ unobservable. Hence, we would be facing a more difficult control problem than the one dealt with for the 1 cm fiber, in the sense that not all modes would be observable with a single electrode. This difficulty could be overcome by using two observing electrodes: one for the optimal time and location (x_o^1, τ_1) for mode $i = 1$, and another one for the optimal time and location (x_o^2, τ_2) for modes $i = 2, 3, ..., 8$. In this case Eq. (117) would preserve the

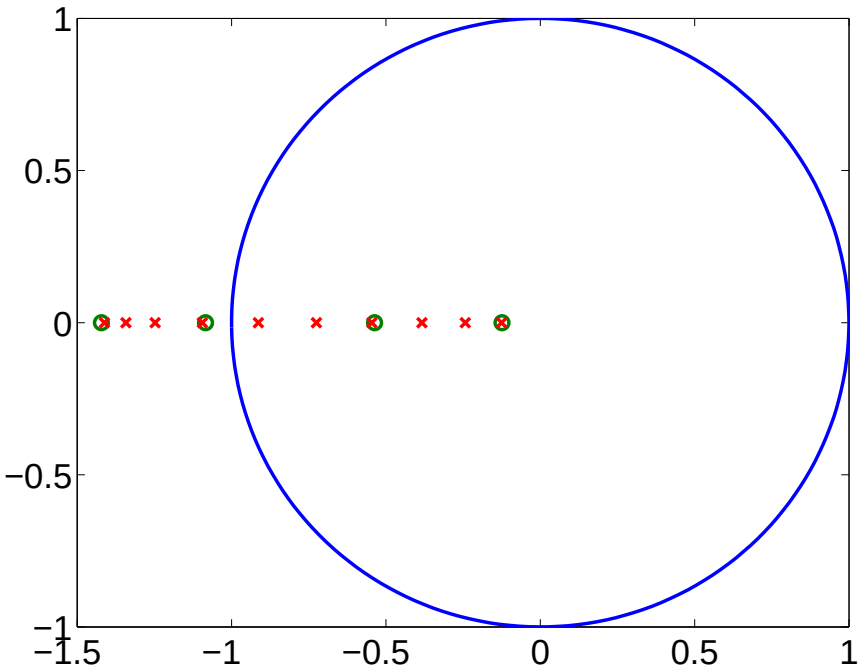

Figure 42: Spectrum of $U(T,0)$ for $L = 1$ cm (green circles) and $L = 3$ cm (red crosses). In both cases $T = 185$ ms. Only eigenvalues with $|\lambda_i| > 0.1$ are displayed. The unstable eigenvalues lay outside the unit circle (blue line).

same form but with all quantities redefined as $v^n = [v_1^n, v_2^n]^{\mathcal{T}}$ where $v_k^n = u(x_o^k, t_n^k)$ with $t_n^k = \tau_k + nT$, $k = 1, 2$,

$$C = \begin{bmatrix} C_{11} & C_{12} \\ C_{21} & C_{22} \\ \vdots & \vdots \\ C_{m1} & C_{m2} \\ 1 & 0 \\ 0 & 1 \end{bmatrix},$$

where $C_{ik} = e_i^u(x_o^k, \tau_k)$, $k = 1, 2$ and

$$\mathbf{r}^n = [\xi_1^n, \xi_2^n, ..., \xi_m^n, v_1^n, v_2^n]^{\mathcal{T}}. \tag{121}$$

Similarly, the control method can be generalized to use a control time τ_c different from the observing times τ_1 and τ_2.

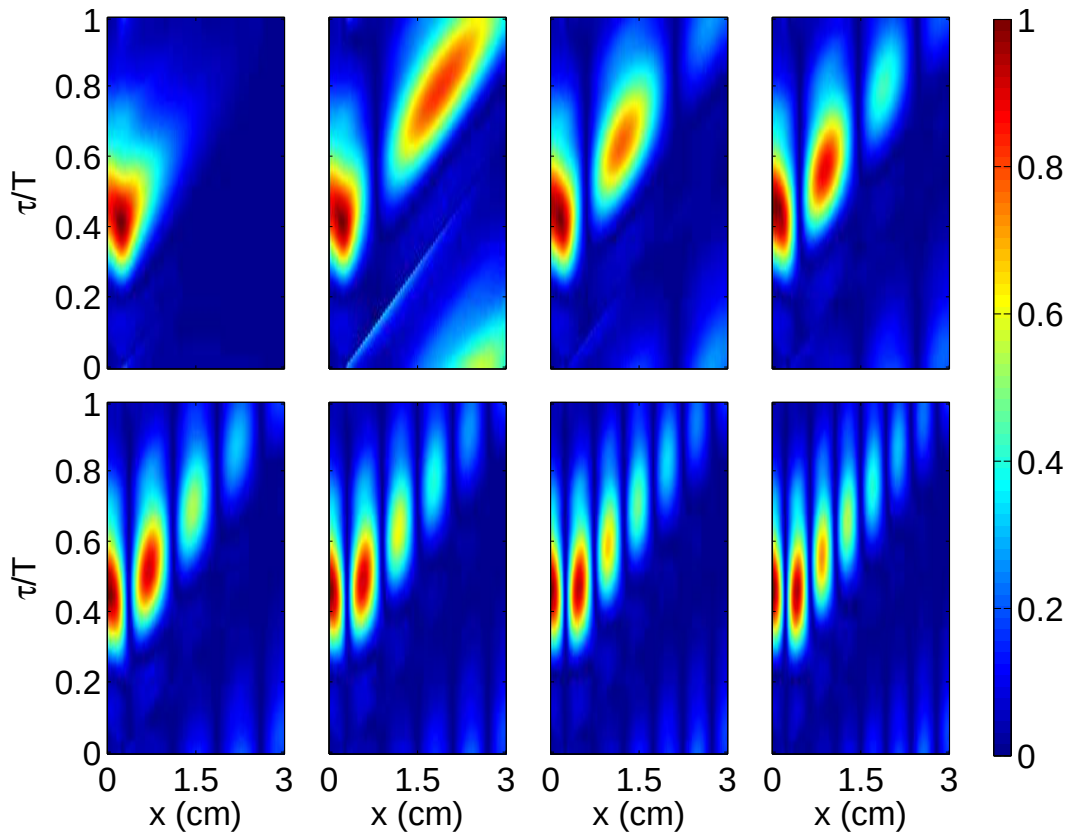

Figure 43: $|f_i^u(x,\tau)|$ for the eight leading modes for $L = 3$ cm and $T = 185$ ms. Top, from left to right: $i = 1, 2, 3, 4$. Bottom, from left to right: $i = 5, 6, 7, 8$.

4.4 Conclusion

This study demonstrates that, for the ring geometry, model-based control considerably outperforms TDAS in suppressing alternans. The advantages of model-based control over TDAS are twofold: (i) alternans is suppressed in a shorter time and (ii) the risk of tissue damage is reduced due to smaller control current. Although we used a particular control theoretic approach (LQR), our results support the conclusion that using a model of cardiac dynamics in the implementation and development of control procedures generally allows one to improve the effectiveness, while at the same time reducing the side effects of control, compared with the leading empirical approaches such as TDAS.

It is important to mention an issue that will inevitably arise in an experimental

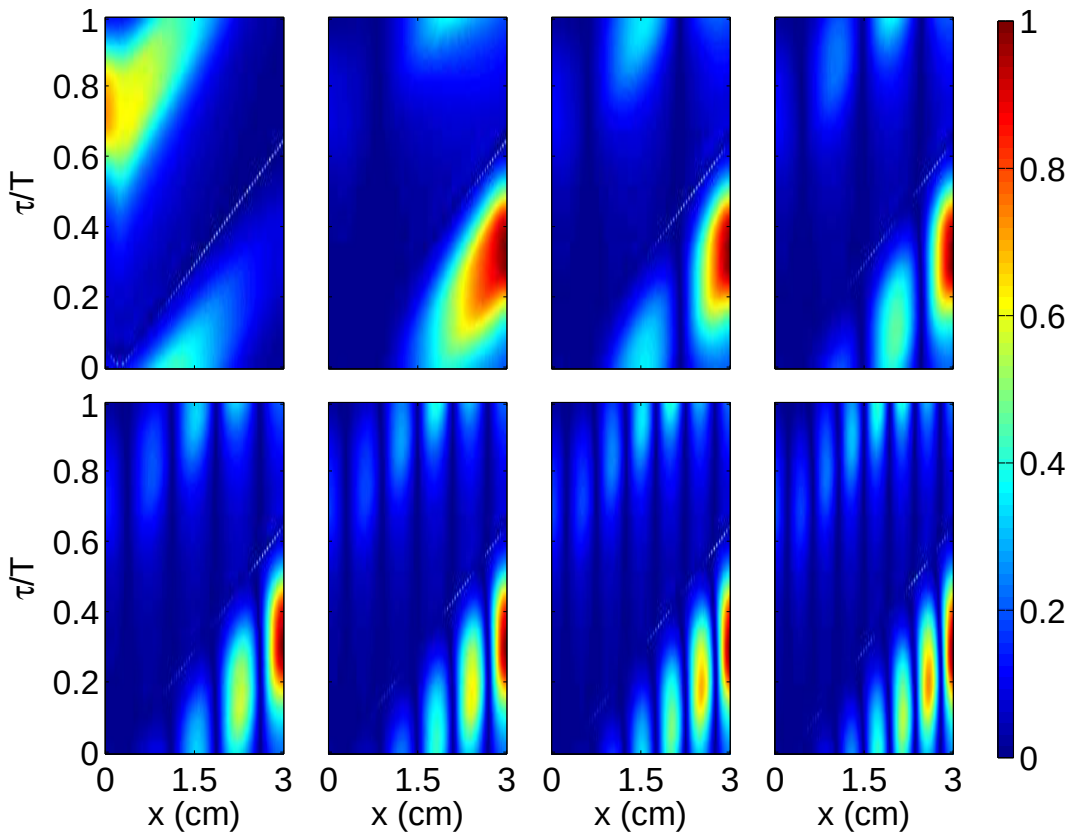

Figure 44: $|e_i^u(x,\tau)|$ for the eight leading modes for $L = 3$ cm and $T = 185$ ms. Top, from left to right: $i = 1, 2, 3, 4$. Bottom, from left to right: $i = 5, 6, 7, 8$.

implementation of any model-based control protocol: determining the system state. For model-based control on the ring, we assumed knowledge of the complete system state (all variables at all points in space) at the beginning of each time period $t = t_n$. Although the use of voltage- and calcium-sensitive dyes and microelectrode recordings in principle allows one to determine the spatial distribution of certain model variables in real time [19], this approach is extremely impractical, especially *in vivo*. A more practical alternative approach involves state reconstruction (or state estimation, in the language of control theory) based on measurements of a few model variables at one or several spatial locations [17, 5]. As mentioned previously, we demonstrated the feasibility of state estimation for the open fiber. A control scheme based on state estimation for the ring geometry should be the subject of future study.

For the open fiber, we have shown that following a systematic model-based approach it is possible to design a control procedure that overcomes the limitations of the PIA approach, yet is equally simple to implement experimentally. One important feature of the model-based method used is the ability to estimate the system state from measurements of the transmembrane voltage by just a few electrodes. The model-based analysis also allows one to determine how the electrodes should be arranged along the fiber, regardless of the method used to determine the feedback current. Finally, we explained that PIA control breaks down due to the loss of controllability when the second unstable mode appears. The criterion based on the number of unstable modes is more accurate and conceptually more straightforward that the one derived using the amplitude equation formalism [21]. More importantly, it allows one to constructively solve the control problem for $L \geq 1$ cm.

Although our results apply only to rather simplified situations (reduced models in a 1D medium), they suggest that model-based control should have similar advantages for actual cardiac tissue. In order to test this hypothesis, more realistic ionic models and physiologically relevant geometries must be investigated first, with experimental validation to follow.

There is no guarantee that the model-based approaches implemented here will succeed at suppressing alternans in all physiologically relevant ranges of parameters and initial conditions. This is primarily due to the fact that a linear approximation of the dynamics is used for the calculation of the control current. The occasional failures of this approximation are made evident by the several instances reported here in which LQR control in the ring geometry induced conduction block, an essentially nonlinear phenomenon. Similarly, for the ring, at large amplitudes, the average conduction velocity of the fully developed alternans state might deviate sufficiently from that of the target state for linear control to be successful. Besides shielding the control method against conduction block, incorporating elements of nonlinear dynamics of the

system is also expected to improve efficiency as reflected, for example, in a reduction of the control time and the current magnitude. This topic should be addressed in future research.

CHAPTER V

CONCLUSIONS

Alternans is a dynamical regime of the heart that in some instances precedes the onset of ventricular fibrillation (VF) [10]. We found that the onset of the alternans, in both the ring and the open fiber, occurs when the normal rhythm becomes unstable. For the ring geometry, we found that the state of alternans arises as a limit cycle by means of a supercritical Hopf bifurcation that renders the normal rhythm (stationary solution) unstable. For the open fiber the state of alternans arises by a period-doubling bifurcation of the normal rhythm. From the perspective of the stroboscopic map, this is a bifurcation from a fixed point (the normal rhythm) to a periodic orbit of period 2. Hence the phase-space scenario of a regime in which alternans is present is essentially the same for both the ring and the open fiber: an unstable fixed point (the normal rhythm) is surrounded by a stable periodic orbit (the state of alternans). We found that this picture becomes more complex for the open fiber in a subset of the (L, T) parameter space. In this region of parameters, three different states of alternans coexist in what preliminary results indicate is a cusp bifurcation. A more in-depth study of this bifurcation should be the subject of future research.

Suppression of alternans using feedback control represents a possible therapy for the prevention of VF. Despite the efforts in this direction, only limited success has been achieved in the suppression of alternans so far. In this thesis we introduced a new approach to alternans control. It is based on a combination of well known tools of nonlinear dynamics and control theory: (i) linear stability analysis based on eigenmodes of the linearized dynamics. (ii) Galerkin truncation and Poincare section which reduce the infinite dimensional representation of electrical activity in terms of

a PDE to a discrete-time low-dimensional map. (iii) Feedback control of linear time invariant systems. And finally, (iv) state estimation from the limited data that can be actually gathered in experiments.

The control methods based on this approach are referred to as *model-based* to emphasize the fact that they rely on a model of the dynamics. This is in contrast with previously studied techniques that do not use a model (non-model-based methods). We assessed the performance of model-based control methods for one dimensional media, using two geometrical configurations: a ring and an open fiber. In both cases, we found model-based methods to outperform non-model-based techniques as explained below.

For the ring geometry, we found that model-based control outperformed non-model-based (time delay autosynchronization, TDAS [72]) control concerning two aspects: (i) alternans is suppressed in a shorter time and (ii) the risk of tissue damage is reduced due to a smaller control current. For the open fiber, model-based control was able to suppress alternans for longer fibers and higher pacing rates than non-model-based (pacing interval adjustment, PIA [21]) control. Additionally, we found that PIA has a significant effect only on the leading mode and, hence, this procedure fails when the subleading mode becomes unstable.

It is not granted that the model-based control methods implemented here will succeed at suppressing alternans in all physiologically relevant ranges of parameters and initial conditions. This is due to the fact that a linear approximation of the dynamics around the normal rhythm is used for the calculation of the control current. This approximation is inappropriate, for instance, for describing the saturation of the growth of a perturbation as the state of fully developed alternans (FDA) is approached. This explains why in many cases our model-based control approach fails for initial conditions lying near FDA. The results obtained for the ring were an exception to this behavior. In that case, model-based control was effective even when the

initial condition was FDA. This is explained by the fact that since L was close to the bifurcation point L_c, FDA was weakly attracting and hence was easily overridden by the linear control. To generalized model-based control so that it would also be effective in the proximity of FDA for parameter values far from the bifurcation point (a topic for future research), we would need to study how the eigenmodes of the normal rhythm and FDA and its eigenmodes are related. Center manifold theory [7] might be useful in determining these relations. Therefore, bifurcation analysis of alternans has not only a theoretical interest but also a practical application.

PIA control is highly effective at suppressing perturbations proportional to the leading eigenmode. This high efficacy seems not to be explained by the controllability criterion introduced in Sect. 4.3.4, based on linear stability analysis with a fixed period T. Conceivably, performing linear stability analysis that allows the period to vary might bring light into the workings of PIA. The efficacy of PIA concerning the leading eigenmode also motivates the design of a hybrid control procedure that would initially use PIA to diminish the leading component of the perturbation (the most significant one in some cases) and later would switch to model-based control.

We used the Noble model for the ionic current mainly with the purpose of comparison with Ref. [21]. However, this model is not an accurate description of canine Purkinje fibers (the ones typically used in experiments). For instance, the model-predicted conduction velocity (the velocity with which an action potential travels) is around 30 cm/s while the one observed experimentally is 200 cm/s [16]. Therefore, in order for the model-based methods presented here to be tested in experiments, our results need to be reproduced using more realistic models of canine Purkinje fibers.

Model-based control of alternans can also serve as a tool for model validation. As any other system that is object of scientific research, heart tissue can be seen as a black box that delivers outputs in response to inputs. Control provides an opportunity for submitting heart tissue to a different set of inputs (control currents)

than those traditionally used (mainly limited to the short initial injection of current that generates a traveling wave). Control therefore affords a different perspective that could reveal key aspects of arrhythmia development.

For an open fiber of arbitrary length, for each eigenmode, the spatio-temporal region where the absolute value of the mode's left (right) eigenfunction has a significant value is a region of enhanced controllability (observability). For successful control, the controlling and observing electrodes and the times of control and observation must be located inside these optimal regions for all the relevant modes (unstable or weakly stable modes). When the optimal regions of the relevant modes overlap substantially, control can be achieved by few observing and controlling electrodes (the best possible case is illustrated by Fig. 39, in which control and observation are performed by one and the same electrode). If overlap is less ubiquitous, multiple controlling and observing electrodes might be required (this is illustrated by Fig. 44 in which the optimal region of observation for mode 1 has little overlap with the optimal regions for the remaining modes). We must note that, although we use the same time for control and observation in the compensator control, this procedure can be generalized to the case when these times are different.

The model-based approach presented here can be extended to the control of two- and three-dimensional tissue, and, eventually, the entire ventricles in vivo. An accurate model of the ventricles must emulate properties such as their shape (represented by appropriate boundary conditions) and the spatial heterogeneity and anisotropy of the tissue [25]. The accuracy of the model also improves by giving a separate treatment to the intra- and extracellular spaces (bidomain model [38]) and by using a more detailed description of the ionic current dynamics, such as the Luo-Rudy model [53]. A remarkable fact is that, however daunting the complexity of the model, it is possible to cast the evolution equation in the form (56) and from that point onward proceed to the modal decomposition by the methodology described in Sect. 3.2.2.

Due to the matrix-free numerical techniques used for the calculation of the normal rhythm (Newton-Krylov method) and the eigenmodes (Arnoldi method), the computational time scales as the time required to integrate the evolution equation during one pacing period. Hence, although a substantial increase of the computational time is expected, computational demands are far from being a prohibitive obstacle. As for the open fiber, the number of electrodes required for control and observation of 2D and 3D tissue depend on the extent of the overlap of the regions of non negligible controllability (left eigenfunctions) and observability (right eigenfunctions) of relevant modes. In the most favorable scenario, high overlap would lead to a small number of electrodes.

APPENDIX A

NUMERICAL METHODS

A.1 Integration of evolution equation

For both the open fiber and the ring, the solutions of the nonlinear PDE, either (6) or (40), were computed numerically by discretizing the PDE in space and time by the method of finite differences. For the open fiber, we integrated the evolution equation (6) in the stationary reference frame using explicit Euler time stepping. We used a mesh size of $\Delta x = 0.01$ cm and a time step of $\Delta t = 0.01$ ms. For non-model-based control (TDAS, see section 4.2.1) on the ring, we integrated the evolution equation in the fixed reference frame by explicit Euler. We used a uniform mesh of 2000 points, which corresponds to a mesh size $\Delta x = L/2000$. For a typical length of 10 cm this corresponds to $\Delta x = 5 \times 10^{-3}$ cm. The time step was set to 8.25×10^{-4} ms. For the free dynamics and model-based control we used the co-moving reference frame. In the co-moving reference frame the explicit Euler method becomes unstable due to the presence of the advection term $\partial_x \mathbf{z}$. For that reason, Eq. (40) was integrated using an operator-splitting method. The Crank-Nicolson method was used for the diffusion and advection terms, while the reaction terms were advanced by Heun's method [81]. In this case we also used a uniform mesh of 2000 points. The time step was set to 2×10^{-3} ms.

A.2 Open fiber

A.2.1 Calculation of the fixed point (normal rhythm)

For the open fiber, the normal rhythm as well as the state of alternans are described in the laboratory reference frame as periodic solutions, with periods T and $2T$ respectively, of the evolution equation (6) subject to the pacing current (14). Here we describe a method for the calculation of periodic orbits. We present the method applied only to the calculation of the normal rhythm, although a substitution of T by $2T$ readily gives its extension to the determination of the state of alternans.

Let $G(\mathbf{z}; T, 0)$ denote the time evolution operator of (6) from $t = 0$ to $t = T$,

$$\mathbf{z}(x, T) = G[\mathbf{z}(x, 0); T, 0]. \tag{122}$$

Since $\mathbf{z}_p(x, 0)$ is a periodic orbit,

$$\mathbf{z}_p(x, 0) = \mathbf{z}_p(x, T). \tag{123}$$

From (122) and (123) it follows that $\mathbf{z}_p(x, 0)$ is a fixed point of $G(\mathbf{z}; T, 0)$,

$$\mathbf{z}_p = G[\mathbf{z}_p; T, 0]. \tag{124}$$

or

$$G[\mathbf{z}_p; T, 0] - \mathbf{z}_p = 0. \tag{125}$$

We can solve (125) using Newton's method. In order to find a correction $\delta\mathbf{z}_n$ to an approximation $\mathbf{z}_n$ to $\mathbf{z}_p$ we approximate the l.h.s of (125) by its Taylor series expansion up to first order

$$0 = G[\mathbf{r}_n + \delta\mathbf{r}_n] - \mathbf{r}_n - \delta\mathbf{r}_n \tag{126}$$

$$\approx G(\mathbf{r}_n) + J_G|_{\mathbf{z}_n}\delta\mathbf{r}_n - \mathbf{r}_n - \delta\mathbf{r}_n, \tag{127}$$

where J_G is the Jacobian of G evaluated at $\mathbf{z}_n$

$$J_G|_{\mathbf{z}_n}\delta\mathbf{z} = \lim_{\epsilon\to 0}\frac{G[\mathbf{z}_n + \epsilon\delta\mathbf{z}] - G[\mathbf{z}_n]}{\epsilon}. \tag{128}$$

Rearranging terms in (127), we obtain

$$\left(J_G|_{\mathbf{z}_n} - 1_o\right) \delta\mathbf{z}_n = \mathbf{z}_n - G(\mathbf{z}_n), \tag{129}$$

where 1_o is the identity operator. (129) is a linear equation with the function $\delta\mathbf{z}_n$ as unknown. In order to solve (129), we discretized it by the method of finite differences on a uniform grid of N points, $x_i = (i-1)h, \quad i = 1, ..., N$ with $h = L/(N-1)$. For the open fiber, $h = 0.01$ cm. Hence, the state vector $\mathbf{z}$ with $(\zeta + 1)$ elements, each of which is a function of x, $\mathbf{z}(x) = [u(x), n_1(x), n_2(x), ..., n_\zeta(x)]$, becomes a vector of $N(\zeta + 1)$ elements, $\mathbf{r} = [r_1, ..., r_{N(\zeta+1)}]$,

$$\begin{aligned} [r_1, ..., r_N] &= [u(x_1), ..., u(x_N)] \\ [r_{N+1}, ..., r_{2N}] &= [n_1(x_1), ..., n_1(x_N)] \\ &\vdots \\ \left[r_{N\zeta}, ..., r_{N(\zeta+1)}\right] &= [n_\zeta(x_1), ..., n_\zeta(x_N)]. \end{aligned} \tag{130}$$

Similarly, (129) becomes a linear system of algebraic equations

$$\left(J_{\widetilde{G}}|_{\mathbf{r}_n} - \widetilde{1}\right) \delta\mathbf{r}_n = \mathbf{r}_n - \widetilde{G}(\mathbf{r}_n), \tag{131}$$

where $\widetilde{G}$ is the discretized version of G, $J_{\widetilde{G}}|_{\mathbf{z}_n}$, the Jacobian of $\widetilde{G}$ (defined by an expression similar to (128)) is an $N(\zeta+1) \times N(\zeta+1)$ matrix and $\widetilde{1}$ is the unit matrix. We solved (131) by generalized minimal residual method (GMRES) implemented by the Matlab function **gmres**. In using GMRES we have two alternatives: providing the explicit matrix representation of $\left(J_{\widetilde{G}}|_{\mathbf{r}_n} - \widetilde{1}\right)$ or providing instead a routine that calculates the matrix-vector product (matrix-free form). For efficiency, we used the second alternative with the first term of the matrix-vector product approximated by

$$J_{\widetilde{G}}\Big|_{\mathbf{r}_n} \delta\mathbf{r}_n \approx \frac{\widetilde{G}[\mathbf{r}_n + \epsilon\delta\mathbf{r}_n] - \widetilde{G}[\mathbf{r}_n]}{\epsilon}, \tag{132}$$

where ϵ was chosen so that $\epsilon\|\delta\mathbf{r}_n\|_1/\|\mathbf{r}_n\|_1 = 10^{-6}$, where $\|\mathbf{r}\|_1 = \max_i |r_i|$. The operator $\widetilde{G}[\mathbf{z}]$ is calculated by integrating in time the set of ODEs resulting from the

spatial discretization of (6). For the open fiber we used explicit Euler method with a time step of 0.01 ms.

The recurrence relation $\mathbf{r}_{n+1} = \mathbf{r}_n + \delta\mathbf{r}_n$, with $\delta\mathbf{r}_n$ given by Eq. (131) converges toward $\mathbf{r}_p$, for a good enough initial guess $\mathbf{r}_0$. The use of Newton's method together with the matrix-free form of a Krylov-space linear solver like GMRES, constitutes what is known as a matrix-free Newton-Krylov method [47].

A.2.2 Calculation of the right eigenfunctions

The spectrum of the discretized version of $U(T,0)$, $\widetilde{U}(T,0)$, was found using the implicitly re-started Arnoldi iteration method [50], implemented by the MATLAB routine **eigs**. For the sake of efficiency, this method was also applied in its matrix-free form using a routine that calculates the matrix-vector product, in this case $\widetilde{U}(T,0)\delta\mathbf{r}$ (where $\mathbf{r}$ is the discretized version of $\mathbf{z}$), instead of the explicit matrix representation of $\widetilde{U}(T,0)$. It is possible to prove that $U(T,0)$ is the same as the Jacobian $J_G|_{\mathbf{z}_p}$ defined by Eq. (128), evaluated at $\mathbf{z}_p$. Therefore the matrix-vector product can be calculated by

$$\widetilde{U}(T,0) \approx \frac{\widetilde{G}[\mathbf{r}_p + \epsilon\delta\mathbf{r}] - \widetilde{G}[\mathbf{r}_p]}{\epsilon}, \tag{133}$$

with ϵ chosen as in (132).

A.2.3 Calculation of the left eigenfunctions

The eigenfunctions $\mathbf{f}_i(0)$ of $U^\dagger(T,0)$ are computed using the matrix-free approach described previously. We computed the "matrix-vector" product $U^\dagger(T,0)\delta\mathbf{z}$ as follows. If Eq. (58), in the absence of control, is integrated in time by explicit Euler step, we obtain

$$U(T,0) \approx \prod_{i=0}^{N-1} \left(1 + \Delta t J_{\mathcal{N}}(t_i)\right), \tag{134}$$

where $t_i = i\Delta t$ with Δt the time step and $N = T/\Delta t$. Taking the adjoint of both sides of (134),

$$U(T,0)^\dagger \approx \prod_{i=N-1}^{0} \left(1 + \Delta t J_{\mathcal{N}}^\dagger(t_i)\right). \tag{135}$$

For a uniform mesh, the discretization of $J_{\mathcal{N}}^\dagger(t_i)$ is the transpose conjugate of the discretization of $J_{\mathcal{N}}(t_i)$. The product on the r.h.s. of (135) is the sequence of Euler steps necessary for the calculation of $U(T,0)^\dagger \delta\mathbf{z}$. The relationship $\mathbf{f}_i(\tau) = U^\dagger(\tau,0)\mathbf{f}_i(0)$ is then used to compute the eigenfunctions for other values of τ.

A.3 Ring geometry

A.3.1 Calculation of the normal rhythm

For the ring geometry in the co-moving reference frame, the normal rhythm $\mathbf{z}_p$ is a stationary solution, $\partial_t \mathbf{z}_p = 0$, of the dynamical equation (41) in the absence of control current,

$$\mathcal{N}[\mathbf{z}_p] = 0 \tag{136}$$

where

$$\mathcal{N}[\mathbf{z}] \equiv c\partial_x \mathbf{z} + \widetilde{D}\partial_x^2 \mathbf{z} + F(\mathbf{z}), \tag{137}$$

As no time dependence is present in (136), this equation is a system of ODEs with x an independent variable. We can turn (136) into a system of first order ODEs by defining the variable $\rho = \partial u/\partial x$,

$$\dot{\rho} = -\frac{1}{D_{11}}[c\rho + F_1(\mathbf{z})] \tag{138a}$$

$$\dot{u} = \rho \tag{138b}$$

$$\dot{z}_2 = -\frac{1}{c}F_2(\mathbf{z}) \tag{138c}$$

$$\dot{z}_3 = -\frac{1}{c}F_3(\mathbf{z}) \tag{138d}$$

where the dot means derivation with respect to x and z_2 and z_3 are the two gate variables of the 3-variable Fenton-Karma model. As periodic boundary conditions

must be satisfied, solving (136) is equivalent to finding a periodic orbit $\mathbf{y}_p = [\rho_p, \mathbf{z}_p]$ of (138) with period equal to the ring length L. The value of c is also found in the process. We first attempted to find $\mathbf{y}_p$ by the simple shooting method [81]. However, this method failed due to the fact that $\mathbf{y}_p$ is highly unstable. We succeeded using a more refined approach, the variational method [49] (see Section A.4). This method was modified to obtain a higher density of mesh points in the region where the variables change faster. This allowed the back and the front of the pulse to be accurately resolved while allowing a more sparse sampling of the plateau and the unexcited region (Section A.4).

A.3.2 Calculation of the right eigenfunctions

The leading eigenvalues and eigenfunctions were found numerically by discretizing (48) on the nonuniform mesh produced by the variational method. The advection and diffusion terms in $J_{\mathcal{N}}$ were approximated by finite differences. The corresponding matrix eigenvalue problem was then solved via the implicitly re-started Arnoldi iteration method [50] implemented by the MATLAB (Mathworks, Inc.) routine `eigs`.

A.3.3 Calculation of the left eigenfunctions

The adjoint eigenfunctions $\mathbf{f}_i$ were computed by approximating

$$J_{\mathcal{N}}^{\dagger}\mathbf{f}_j(x) = \lambda_j^*\mathbf{f}_j(x). \tag{139}$$

by a matrix eigenvalue problem. The matrix representation of $J_N^{\dagger}$ was obtained by discretizing the equation that defines the adjoint of J_N [40],

$$\langle J_N\mathbf{z}', \mathbf{z}''\rangle = \left\langle \mathbf{z}', J_N^{\dagger}\mathbf{z}''\right\rangle, \tag{140}$$

for all $\mathbf{z}'$ and $\mathbf{z}''$. From (140) the matrix elements of $J_N^{\dagger}$ are found to be related to the matrix elements of J_N by

$$(J_N^{\dagger})_{ik} = h_i^{-1}h_k(J_N)_{ki}^*, \tag{141}$$

where h_i is the length of the interval between the mesh points i and $i+1$.

A.4 Variational method for the calculation of periodic orbits

A.4.1 Introduction

The variational method, which is the limit of the multiple shooting method [81] when the number of points goes to infinity, is recommended for the calculation of highly unstable periodic orbits, for which the simple shooting method fails.

Ref. [81] calls this method *general Newton's method* and *quasilinearization*, while Ref.[49] refers to it as a *variational method*. It is presented in [81] in the context of the solution of more general boundary value problems (the calculation of a periodic orbit is a boundary value problem with periodic boundary conditions). Although following seemingly different lines of reasoning, [81] and [49] arrive at the same iteration rule.

Let

$$\frac{d\mathbf{y}}{dx} = \mathbf{v}(\mathbf{y}, \mathbf{p}), \tag{142}$$

be the dynamical system of interest, where $\mathbf{y}(x) = [y_1(x), y_2(x), ..., y_n(x)]$ is the state variable and $\mathbf{p} = [p_1, p_2, ..., p_m]$ is the set of parameters. We want to find a periodic orbit $\mathbf{y}^*(x)$ of (142), $\mathbf{y}^*(0) = \mathbf{y}^*(\lambda)$, where λ is the period. For dynamical systems like (142) not driven by a periodic external force, the period λ is usually left as an unknown that must be determined by the algorithm. In some applications, however, it is more convenient to choose the value of λ and allow one of the parameters, p_k, to be the unknown. This happens for instance when periodic orbits do not exist for values of p_k outside a range whose precise limits are not known a priori. In the next section we recast the problem in a way that makes no distinction between these two cases.

The method and its numerical implementation using finite differences approximation are explained in section A.4.3. In section A.4.4 we present a way of obtaining a variable mesh size that allows a better resolution of zones of fast dynamics.

A.4.2 Reformulation of the problem

Performing the change of variable $s = x/\lambda$, (142) can be written as

$$\frac{d\tilde{\mathbf{y}}}{ds} = \lambda \mathbf{v}(\tilde{\mathbf{y}}, \mathbf{p}), \tag{143}$$

where $\tilde{\mathbf{y}}(s) = \mathbf{y}(\lambda s)$. Note that λ appears in (143) as an additional parameter. We fix the values of all parameters except one, q, that could be any of $\lambda, p_1, ..., p_m$, and whose value must be determined by the algorithm. For convenience we put (143) in the form

$$\frac{d\tilde{\mathbf{y}}}{ds} = \tilde{\mathbf{v}}(\tilde{\mathbf{y}}, q) \tag{144}$$

where

$$\tilde{\mathbf{v}}(\tilde{\mathbf{y}}, q) = \begin{cases} q\,\mathbf{v}(\tilde{\mathbf{y}}, \mathbf{p}), \text{ if } q = \lambda \\ \lambda\,\mathbf{v}(\tilde{\mathbf{y}}, [p_1, ..., p_{k-1}, q, p_{k+1}..., p_m]), \text{ if } q = p_k \end{cases} \tag{145}$$

The periodicity condition $y^*(0) = y^*(\lambda)$ is transformed into $\tilde{\mathbf{y}}^*(0) = \tilde{\mathbf{y}}^*(1)$. Therefore our original problem is turned into that of finding a periodic orbit of (144), $\tilde{\mathbf{y}}^*$, with period one and the value $q = q^*$, for which such orbit exists.

A.4.3 Variational method

In this method the initial approximation to $\tilde{\mathbf{y}}^*(s)$ is a closed orbit $\mathbf{z}^0(s)$ defined for all s in $[0, 1]$. $\mathbf{z}^0(s)$ does not necessarily satisfy (144) and hence the functional

$$F[\mathbf{z}^0, r_0] = \int_0^1 \left\| \frac{d\mathbf{z^0}}{ds} - \tilde{\mathbf{v}}(\mathbf{z}^0, r_0) \right\|^2 ds, \tag{146}$$

where r_0 is an initial approximation to q^*, is in general different from zero, $F[\mathbf{z}^0, r_0] \neq 0$. $\mathbf{z}^0$ is improved by adding to it a correction $\Delta\mathbf{z}^0(s)$ that is a periodic orbit of a linear dynamical system. A correction Δr_0 for r_0 is also calculated. If $\mathbf{z}^0$ is close enough to $\tilde{\mathbf{y}}^*$, iteration of this procedure gives a sequence of approximations $\mathbf{z}^{l+1} = \mathbf{z}^l + \Delta\mathbf{z}^l$ that converges to $\tilde{\mathbf{y}}^*$. As

$$F[\tilde{\mathbf{y}}^*, q^*] = 0 = \min_{\mathbf{z}, r} F[\mathbf{z}, r], \tag{147}$$

this technique is a variational method with respect to $F[\mathbf{z}, r]$.

In explaining the rule for the calculation of the correction $\Delta\mathbf{z}$ (the superscript l is omitted) we follow the exposition of [81] restricted to the case of periodic boundary conditions. Substituting $\tilde{\mathbf{y}} = \mathbf{z} + \Delta\mathbf{z}$ and $q = r + \Delta r$ into (144), performing a Taylor series expansion and keeping only the linear terms

$$\frac{d\mathbf{z}}{ds} + \frac{d(\Delta\mathbf{z})}{ds} = \tilde{\mathbf{v}}(\mathbf{z}, r) + \left.\frac{D\tilde{\mathbf{v}}}{D\tilde{\mathbf{y}}}\right|_{\mathbf{z},r} \Delta\mathbf{z} + \left.\frac{\partial\tilde{\mathbf{v}}}{\partial q}\right|_{\mathbf{z},r} \Delta r \tag{148}$$

where $D\tilde{\mathbf{v}}/D\tilde{\mathbf{y}}$ is the Jacobian of $\tilde{\mathbf{v}}$, $(D\tilde{\mathbf{v}}/D\tilde{\mathbf{y}})_{ij} = \partial\tilde{v}_i/\partial\tilde{y}_j$. Rearranging (148) we obtain

$$\left(\frac{d}{ds} - \frac{D\tilde{\mathbf{v}}}{D\tilde{\mathbf{y}}}\right)\Delta\mathbf{z} - \frac{\partial\tilde{\mathbf{v}}}{\partial q}\Delta r = \tilde{\mathbf{v}}(\mathbf{z}, r) - \frac{d\mathbf{z}}{ds} \tag{149}$$

(the evaluation notation has been dropped). This is a linear differential equation for $\Delta\mathbf{z}$ with an unknown parameter Δr.

In order to solve (149) numerically we discretize it by the method of finite differences, obtaining

$$L\mathbf{a} - \mathbf{b}\Delta r = \mathbf{c}, \tag{150}$$

where the column vector $\mathbf{a}$ is the discretized version of $\Delta\tilde{\mathbf{y}}(s)$,

$$\begin{aligned}
[a_1, ..., a_n] &= [\Delta z_1(s_1), ..., \Delta z_n(s_1)] \\
[a_{n+1}, ..., a_{2n}] &= [\Delta z_1(s_2), ..., \Delta z_n(s_2)] \\
&\vdots \\
\left[a_{(N-1)n+1}, ..., a_{Nn}\right] &= [\Delta z_n(s_N), ..., \Delta z_n(s_N)].
\end{aligned} \tag{151}$$

where the grid points s_i are evenly spaced $s_i = (i-1)h$ with $h = 1/N$ the mesh size and N the number of grid points. Similarly, $\mathbf{b}$ and $\mathbf{c}$ are the discretized versions of $\partial\tilde{\mathbf{v}}/\partial q$ and $\tilde{\mathbf{v}}(\mathbf{z}, q) - d\mathbf{z}/ds$ and L is an $nN \times nN$ matrix that corresponds to the differential operator $d/ds - D\tilde{\mathbf{v}}/D\tilde{\mathbf{y}}$. Following [49] we use the four-point approximation for the first derivative. For a given variable u

$$\left.\frac{du}{ds}\right|_{s_k} \approx \frac{u(s_{k-2}) - 8u(s_{k-1}) + 8u(s_{k+1}) - u(s_{k+2})}{12h}, \quad 3 \le k \le N-2. \tag{152}$$

The matrix representation of d/ds that this formula generates and the proper handling of the periodic boundary conditions $\Delta\mathbf{z}(0) = \Delta\mathbf{z}(1)$, together with the discretization of $D\tilde{\mathbf{v}}/D\tilde{\mathbf{y}}$ are explained in Ref. [49].

Eq. (150) is a system of Nn linear equations with $Nn+1$ unknowns ($a_1, ..., a_{Nn}$ and Δr) and therefore is underdetermined. An indeterminacy also exists in the problem of finding a periodic orbit of (144): if $\tilde{\mathbf{y}}^*$ a is periodic solution, hence all functions $\tilde{\mathbf{y}}^*_\chi(s) = \tilde{\mathbf{y}}^*(s+\chi),\ \chi \in (0,1)$ are periodic solutions too. We can remove this indeterminacy and at the same time obtain a complimentary condition for (150) by choosing the value of one of the variables, $\tilde{y}_k$, at a given location s_i, $\tilde{y}^*_k(s_i) = y_p$, where y_p is fixed. Therefore

$$\Delta z_k(s_i) = a_j = 0, \tag{153}$$

where j is related to k and i according to (151). Taken together, (150) and (153) form a linear system with a unique solution,

$$\begin{pmatrix} L & \mathbf{b} \\ \mathbf{g} & 0 \end{pmatrix} \begin{pmatrix} \mathbf{a} \\ \Delta r \end{pmatrix} = \begin{pmatrix} \mathbf{c} \\ 0 \end{pmatrix} \tag{154}$$

where $\mathbf{g}$ is a row vector such that $g_j = 1$, for j defined by (153) and $g_i = 0$ for $i \neq j$. Eq. (154) was solved by biconjugate gradient method implemented by the MATLAB routine **bicg**.

In some cases it was necessary to multiply the correction $\Delta\mathbf{z}^l$ by a factor $\alpha < 1$ in order to ensure that the new approximation $\mathbf{z}^{l+1} = \mathbf{z}^l + \alpha\Delta\mathbf{z}^l$ was closer to the solution $\tilde{\mathbf{y}}^*$,

$$F[\mathbf{z}^{l+1}, r_{l+1}] < F[\mathbf{z}^l, r_l]. \tag{155}$$

A.4.4 Adaptive mesh size

Using a grid of equally spaced points, $s_i = (i-1)h$, is inconvenient if along the periodic orbit some variables change rapidly. For a uniform grid, regions of rapid change will be poorly sampled while an unnecessarily high number of points will be

used in sampling regions of slow dynamics. Therefore, it is preferable to use instead a variable mesh size that would allow a finer resolution of the zones of fast dynamics. This can be achieved, without modifying the algorithm presented above, if (143) is replaced by an associated dynamical system that traverses the same periodic orbits as the original one, but with a more constant speed $\|\mathbf{v}\|$. Using the notation of (143) we write the original dynamical system as

$$\frac{d\tilde{\mathbf{y}}}{dt} = \lambda \mathbf{v}(\tilde{\mathbf{y}}, \mathbf{p}) \tag{156}$$

(for convenience we use t for the independent variable). The associated dynamical system is defined as

$$\frac{d\mathbf{w}}{ds} = \frac{\beta}{f[\mathbf{v}(\mathbf{w}, \mathbf{p})]} \mathbf{v}(\mathbf{w}, \mathbf{p}) \tag{157}$$

where β is the period and $f[\mathbf{v}]$ is a properly chosen scalar function. Setting $\mathbf{w}(s) = \tilde{\mathbf{y}}(t)$ and using (156) and (157), we find

$$dt = \frac{\beta}{\lambda} \frac{ds}{f[\mathbf{v}(\mathbf{w}, \mathbf{p})]}. \tag{158}$$

Hence if a periodic orbit of (157), $\mathbf{w}^*$, is calculated by the variational method, a periodic orbit of (156) can be obtained as $\tilde{\mathbf{y}}^*(t) = \mathbf{w}^*(s)$, where t and s are related by the integrated form of (158)

$$t = \frac{\beta}{\lambda} \int_0^s \frac{ds'}{f\{\mathbf{v}[\mathbf{w}^*(s'), \mathbf{p}]\}}. \tag{159}$$

From (159) and the requirement that $t = 1$ when $s = 1$ we get a formula for λ

$$\lambda = \beta \int_0^1 \frac{ds'}{f\{\mathbf{v}[\mathbf{w}^*(s'), \mathbf{p}]\}}. \tag{160}$$

In our numerical implementation $\Delta s_i = s_{i+1} - s_i = h$. Hence, $\Delta t_i = t_{i+1} - t_i$ as given by (158) is

$$\Delta t_i = \frac{\beta}{\lambda} \frac{h}{f\{\mathbf{v}[\mathbf{w}(s_i), \mathbf{p}]\}}. \tag{161}$$

It is convenient to choose $f[\mathbf{v}]$ as an increasing function of the flow speed, $\|\mathbf{v}\|$, for example,

$$f[\mathbf{v}] = 1 + c_1\|\mathbf{v}\|^{c_2}, \tag{162}$$

where $c_1, c_2 > 0$ are tunable parameters whose values are chosen based on visual inspection of the concentration of grid points along the orbit $\tilde{\mathbf{y}}(t)$. From (162) and (161) we can see that the mesh size Δt_i is smaller (larger) in portions of the orbit where $\|\mathbf{v}\|$ is large (small). So the periodic orbit in the parametrization of the original dynamical system, t_i, has a variable mesh size that resolves more (less) finely portions of the orbit with fast (slow) dynamics as was our initial goal.

REFERENCES

[1] A.Karma, "Electrical alternans and spiral wave breakup in cardiac tissue," *Chaos*, vol. 4, p. 461, 1994.

[2] Al-Khadra, A., Nikolski, V., and Efimov, I. R., "The role of electroporation in defibrillation," *Circ. Res.*, vol. 87, pp. 797–804, 2000.

[3] Allexandre, D. and Otani, N. F., "Preventing alternans induced spiral wave breakup in cardiac tissue: an ion channel based approach," *Phys. Rev. E*, vol. 70, p. 061903, 2004.

[4] Amann, H., *Ordinary differential equations: an introduction to nonlinear analysis*. New York: Walter de Gruyter, 1990.

[5] Anderson, B. D. O. and Moore, J. B., *Optimal control: linear quadratic methods*. Englewood Cliffs, N.J.: Prentice Hall, 1990.

[6] Bueno-Orovio, A., Cherry, E. M., and Fenton, F. H., "Minimal model for human ventricular action potential in tissue," *Journal of Theoretical Biology*, vol. 253, pp. 544–560, 2008.

[7] Carr, J., *Applications of centre manifold theory*. New York: Springer-Verlag, 1981.

[8] Chen, P.-S., Wu, T.-J., Ting, C.-T., Karagueuzian, H. S., Garfinkel, A., Lin, S.-F., and Weiss, J. N., "A tale of two fibrillations," *Circulation*, vol. 108, pp. 2298–2303, 2003.

[9] Cherry, E. M. and Fenton, F. H., "Visualization of spiral and scroll waves in simulated and experimental cardiac tissue," *New Journal of Physics*, vol. 10, p. 125016 (43pp), 2008.

[10] Choi, B. R., Jang, W., and Salama, G., "Spatially discordant voltage alternans cause wavebreaks in ventricular fibrillation," *Heart Rhythm*, vol. 4(8), pp. 1057–1068, 2007.

[11] Christini, D. J., Riccio, M. L., Culianu, C. A., Fox, J. J., Karma, A., and Gilmour Jr., R. F., "Control of alternans in canine cardiac purkinje fibers," *Phys. Rev. Lett.*, vol. 96, p. 104101, 2006.

[12] Comtois, P. and Vinet, A., "Alternans amplification following a two-stimulus protocol in a one-dimensional cardiac ionic model of reentry: From annihilation to double-wave quasiperiodic reentry," *Chaos*, vol. 17, p. 023125, 2007.

[13] Courtemanche, M., Glass, L., and Keener, J. P., "Instabilities of a propagating pulse in a ring of excitable media," *Phys. Rev. Lett.*, vol. 70, pp. 2182–2185, 1993.

[14] Courtmanche, M. and Winfree, A. T., "Re-entrant rotating waves in a beeler-reuter based model of two dimensional cardiac electrical activity," *Int. J. Bifurcation Chaos*, vol. 1, p. 431, 1991.

[15] Davies, M. J., "Anatomic features in victims of sudden coronary death: coronary arthery pathology," *Circulation*, vol. 85(suppl I), pp. I–19–I–24, 1992.

[16] Dominguez, G. and Fozzard, H. A., "Effect of streach on conduction velocity and cable properties of cardiac purkinje fibers," *Am. J. Physiol.*, vol. 237, pp. C119–C124, 1979.

[17] Dorato, P., Abdallah, C., and Cerone, V., *Linear-quadratic control: an introduction*. Englewood Cliffs, N.J.: Prentice Hall, 1995.

[18] Dubljevic, S., "Optimal boundary control of cardiac alternans," *Int. J. Robust Nonlinear Control*, vol. 19, p. 135, 2009.

[19] Dubljevic, S., Lin, S.-F., and Christofides, P. D., "Studies of feedback control of cardiac alternans," *Comp. Chem. Eng.*, vol. 32, pp. 2086–2098, 2008.

[20] Echebarria, B. and Karma, A., "Instability and spatiotemporal dynamics of alternans in paced cardiac tissue," *Phys. Rev. Lett.*, vol. 88, p. 208101, 2002.

[21] Echebarria, B. and Karma, A., "Spatiotemporal control of cardiac alternans," *Chaos*, vol. 12, pp. 923–930, 2002.

[22] Echebarria, B. and Karma, A., "Amplitude equation approach to the spatiotemporal dynamics of cardiac alternans," *Phys. Rev. E*, vol. 76, p. 051911, 2007.

[23] Engelstein, E. D. and Zipes, D. P., "Sudden cardiac death," in *The Heart, Arteries and Veins* (Alexander, R. W., Schlant, R. C., and Fuster, V., eds.), (New York, NY), pp. 1081–1112, McGraw-Hill, 1998.

[24] Fenton, F. and Karma, A., "Erratum:"vortex dynamics in three-dimensional continuous myocardium with fiber rotation: filament instability and fibrillation" [chaos 8, 20-47 (1998)]," *Chaos*, vol. 8, p. 879, 1998.

[25] Fenton, F. and Karma, A., "Vortex dynamics in three-dimensional continuous myocardium with fiber rotation: filament instability and fibrillation," *Chaos*, vol. 8, p. 20, 1998.

[26] Fenton, F. H., Cherry, E. M., Hastings, H. M., and Evans, S. J., "Multiple mechanisms of spiral wave breakup in a model of cardiac electrical activity," *Chaos*, vol. 12, p. 852, 2002.

[27] Fenton, F. H., Cherry, E. M., Hastings, H. M., and Evans, S. J., "Real-time computer simulations of excitable media: Java as a scientific language and as a wrapper for c and fortran programs," *BioSystems*, vol. 64, pp. 73–96, 2002.

[28] Fink, M. and Noble, D., "Noble model.," *Scholarpedia*, vol. 3, p. 1803, 2008.

[29] Fox, J. J., Riccio, M. L., Hua, F., Bodenschatz, E., and Gilmour Jr., R. F., "Spatiotemporal transition to conduction block in canine ventricle," *Circ. Res.*, vol. 90, pp. 289–296, 2002.

[30] Garfinkel, A., Kim, Y.-H., Voroshilovsky, O., Qu, Z., Kil, J. R., Lee, M.-H., Karagueuzian, H. S., Weiss, J. N., and Chen, P.-S., "Preventing ventricular fibrillation by flattening cardiac restitution," *Proc. Natl. Acad. Sci. U.S.A.*, vol. 97, p. 6061, 2000.

[31] Garzón, A., Grigoriev, R. O., and Fenton, F. H., "Model-based control of cardiac alternans on a ring," *Phys. Rev. E*, vol. 80, p. 021932, 2009.

[32] Grigoriev, R., "Symmetry and control: spatially extended chaotic systems," *Physica D*, vol. 140, pp. 171–193, 2000.

[33] Guevara, M. R., Ward, G., Shrier, A., and Glass, L., "Electrical alternans and period doubling bifurcations," *Comput. Cardiol.*, pp. 167–170, 1984.

[34] Hagen, G. and Mezić, I., "Control spillover in dissipative evolution equations," in *Proc. of the American Control Conference*, vol. 6, (Chicago, Illinois), pp. 3783–3787, June 2000.

[35] Hall, G. M. and Gauthier, D. J., "Experimental control of cardiac muscle alternans," *Phys. Rev. Lett.*, vol. 88, p. 198102, 2002.

[36] Handel, A. and Grigoriev, R. O., "Pattern selection and control via localized feedback," *Physical Review E*, vol. 72, p. 066208, 2005.

[37] Hassard, B. D., Kazarinoff, N. D., and Wan, Y.-H., *Theory and applications of Hopf bifurcation.* Cambridge: Cambridge University Press, 1981.

[38] Henriquez, C. S., "Simulating the electrical behavior of cardiac tissue using the bidomain model," *Critical Reviews in Biomedical Engineering*, vol. 21, pp. 1–77, 1993.

[39] Hirsch, F. and Lacombe, G., *Elements of functional analysis.* New York: Springer-Verlag, 1999.

[40] Horn, R. A. and Johnson, C. R., *Matrix analysis.* Cambridge, N.Y.: Cambridge University Press, 1985.

[41] http://www.americanheart.org 2010.

[42] Ideker, R. E. and Rogers, J. M., "Human ventricular fibrillation: wandering wavelets, mother rotors, or both?," *Circulation*, vol. 114, pp. 530–32, 2006.

[43] Jacquemet, V., "Steady-state solutions in mathematical models of atrial cell electrophysiology and their stability," *Math. Biosci.*, vol. 208, pp. 241–269, 2007.

[44] Jain, P. K., Ahuja, O. P., and Ahmad, K., *Functional Analysis*. New York: John Wiley & sons, 1995.

[45] Jalife, J., "Ventricular fibrillation: mechanisms of initiation and maintenance," *Annu. Rev. Physiol.*, vol. 62, pp. 25–50, 2000.

[46] Kailath, T., *Linear Systems*. Englewood Cliffs, N.J.: Prentice Hall, 1980.

[47] Knoll, D. A. and Keyes, D. E., "Jacobian-free newton-krylov methods:a survey of approaches and applications," *Journal of Computational Physics*, vol. 193, p. 357, 2004.

[48] Koller, M. L., Riccio, M. L., and Gilmour Jr., R. F., "Dynamic restitution of action potential duration during electrical alternans and ventricular fibrillation," *Am. J. Physiol.*, vol. 275, pp. H1635–H1642, 1998.

[49] Lan, Y. and Cvitanović, P., "Variational method for finding periodic orbits in a general flow," *Phys. Rev. E*, vol. 69, pp. 016217–1,016217–10, 2004.

[50] Lehoucq, R. B., Sorensen, D., and Yang, C., *ARPACK Users' Guide: Solution of Large-Scale Eigenvalue Problems with Implicitly Restarted Arnoldi Methods*. Philadelphia: SIAM Publications, 1998.

[51] Li, M. and Otani, N. F., "Controlling alternans in cardiac cells," *Ann. Biomed. Eng.*, vol. 32, pp. 784–792, 2004.

[52] Lopshire, J. C. and Zipes, D. P., "Sudden cardiac death: Better understanding of risks, mechanisms, and treatment," *Circulation*, vol. 114, pp. 1134–1136, 2006.

[53] Luo, C.-H. and Rudy, Y., "A dynamic model of the cardiac ventricular action potential: I. simulations of ionic currents and concentration changes," *Circulation Research*, vol. 74, pp. 1071–1096, 1994.

[54] Mines, G. R. *J. Physiol. (London)*, vol. 46, p. 349, 1913.

[55] Myerburg, R. J. and Castellanos, A., "Cardiac arrest and sudden death," in *Heart Disease: A Textbook of Cardiovascular Medicine* (Braunwald, E., ed.), (Philadelphia, PA), pp. 742–779, W. B. Saunders, 1997.

[56] Myerburg, R. J., Interian, A., Simmons, J., and Castellanos, A., "Sudden cardiac death," in *Cardiac Electrophysiology: From Cell to Bedside* (Zipes, D. P., ed.), (Philadelphia, PA), pp. 720–731, W. B. Saunders, 2004.

[57] Myles, R. C., Burton, F. L., Cobbe, S. M., and Smith, G. L., "The link between repolarization alternans and ventricular arrhythmias: does the cellular phenomenon extend to the clinical problem?," *J Mol Cell Cardiol*, vol. 45, pp. 1–10, 2008.

[58] Nanthakumar, K., Jalife, J., Masse, S., Downar, E., Pop, M., Asta, J., Ross, H., Rao, V., Mironov, S., Sevaptsidis, E., Rogers, J., Wright, G., and Dhopeshwarkar, R., "Optical mapping of langendorff perfused human hearts: establishing a model for the study of ventricular fibrillation in humans.," *Am. J. Physiol.*, vol. 293, pp. H875–H880, 2007.

[59] Narayan, S. M. and Smith, J. M., "Exploiting rate-related hysteresis in repolarization alternans to improve risk stratification for ventricular tachycardia," *J. Am. Coll. Cardiol.*, vol. 35, p. 1485, 2000.

[60] Nattel, S., "Atrial electrophysiology and mechanisms of atrial fibrillation," *J. Cardiovasc. Pharmacol. Ther.*, vol. 8, pp. S5–11, 2003.

[61] Nikolski, V. P. and Efimov, I. R., "Electroporation of the heart," *Europace*, vol. 7, pp. S146–S154, 2005.

[62] Noble, D., "A modification of the hodgkin-huxley equations applicable to Purkinje fibre action and pacemaker potentials," *J. Physiol.*, vol. 160, p. 317, 1962.

[63] Nolasco, J. B. and Dahlen, R. W., "A graphic method for the study of alternation of cardiac action potentials," *J. Appl. Physiol.*, vol. 25, pp. 191–196, 1968.

[64] Otani, N. F. and Gilmour Jr., R. F., "Memory models for the electrical properties of local cardiac systems," *J. Theor. Biol.*, vol. 187, p. 409, 1997.

[65] Panfilov, A. V., "Spiral breakup in an array of coupled cells," *Phys. Rev. Lett.*, vol. 88, p. 118101, 2002.

[66] Passman, R. and Kadish, A., "Shouldn't everyone have an implantable cardioverter-defibrillator?," *Circulation*, vol. 120, p. 2166, 2009.

[67] Pastore, J. M., Girouard, S. D., Laurita, K. R., Akar, F. G., and Rosenbaum, D. S., "Mechanisim linking t-wave alternans to the genesis of cardiac fibrillation," *Circulation*, vol. 99, pp. 1385–1394, 1999.

[68] Pastore, J. M. and Rosenbaum, D. S., "Role of structural barriers in the mechanism of alternans-induced reentry," *Circ. Res.*, vol. 87, p. 1157, 2000.

[69] Pyragas, K., "Continuous control of chaos by self-controlling feedback," *Phys. Lett. A*, vol. 170, p. 421, 1992.

[70] Qu, F., Ripplinger, C. M., Nikolski, V. P., Grimm, C., and Efimov, I. R., "Three-dimensional panoramic imaging of cardiac arrhythmias in rabbit heart," *J. Biomed. Opt.*, vol. 12, p. 044109, 2007.

[71] Qu, Z., Garfinkel, A., Chen, P.-S., and Weiss, J. N., "Mechanisms of discordant alternans and induction of reentry in simulated cardiac tissue," *Circulation*, vol. 102, pp. 1664–1670, 2000.

[72] Rappel, W. J., Fenton, F., and Karma, A., "Spatiotemporal control of wave instabilities in cardiac tissue," *Phys. Rev. Lett.*, vol. 83, pp. 456–459, 1999.

[73] Restrepo, J. G. and Karma, A., "Spatiotemporal intracellular calcium dynamics during cardiac alternans," *Chaos*, vol. 19, p. 037115, 2009.

[74] Reuter, H., "The dependence of slow inward current in Purkinje fibres on the extracellular calcium concentration.," *J. Physiol. (London)*, vol. 192, p. 479, 1967.

[75] Rogers, J. M. and Ideker, R. E., "Fibrillating myocardium: rabbit warren or beehive?," *Circ. Res.*, vol. 86, pp. 369–70, 2000.

[76] Rosamond, W., Flegal, K., Furie, K., Go, A., Greenlund, K., Haase, N., Hailpern, S. M., Ho, M., Howard, V., Kissela, B., Kittner, S., Lloyd-Jones, D., McDermott, M., Meigs, J., Moy, C., Nichol, G., O'Donnell, C., Roger, V., Sorlie, P., Steinberger, J., Thom, T., Wilson, M., and Hong, Y., "Heart disease and stroke statistics-2008 update: a report from the american heart association statistics committee and stroke statistics subcommittee," *Circulation*, vol. 117, pp. e25–146, 2008.

[77] Rosenbaum, D. S., Jackson, L. E., Smith, J. M., Garam, H., Ruskin, J. N., and Cohen, R. J., "Electrical alternans and vulnerability to ventricular arrythmias," *N. Engl. J. Med.*, vol. 330, pp. 235–241, 1994.

[78] Roth, B. J., "Bidomain model," *Scholarpedia*, vol. 3, no. 4, p. 6221, 2008.

[79] Saksena, S. and Nagarakanti, R., "The future of implantable defibrillator and cardiac resynchronization therapy," *J. Interv. Card. Electrophysiology*, vol. 23, pp. 29–39, 2008.

[80] Samie, F. H. and Jalife, J., "Mechanisms underlying ventricular tachycardia and its transition to ventricular fibrillation in the structurally normal heart," *Cardiovasc. Res.*, vol. 50, p. 242, 2001.

[81] Stoer, J. and Bulirsch, R., *Introduction to numerical analysis*. New York: Springer-Verlag, 1998.

[82] Strogatz, S. H., *Nonlinear dynamics and chaos*. Reading, M.A.: Perseus books, 1994.

[83] Tachibana, H., Kubota, I., Yamaki, M., Watanabe, T., and Tomoike, H., "Discordant s-t alternans contributes to formation of reentry: a possible mechanism of reperfusion arrhythmia," *Am. J. Physiol.*, vol. 275, p. H116, 1998.

[84] Tolkacheva, E. G., Schaeffer, D. G., Gauthier, D. J., and Mitchell, C. C., "Analysis of the Fenton-Karma model through an approximation by a one-dimensional map," *Chaos*, vol. 12, p. 1034, 2002.

[85] Vigmond, E. G., dos Santos, R. W., Prassll, A. J., Deo, M., and Plank, G., "Solvers for the cardiac bidomain equations," *Progress in biophysics and molecular biology*, vol. 96, no. 1, p. 3, 2007.

[86] Walker, M. L. and Rosenbaum, D. S., "Repolarization alternans: implications for the mechanism and prevention of sudden cardiac death," *Cardiovasc. Res.*, vol. 57, p. 599, 2003.

[87] Wang, P. K. C. and Kogan, B. Y., "Parametric study of the Noble's action potential model for cardiac Purkinje fibers," *Chaos, Solitons and Fractals*, vol. 33, pp. 1048–1063, 2007.

[88] Watanabe, T., Fenton, F., Evans, S., Hastings, H., and Karma, A., "Mechanisms for discordant alternans," *J. Cardiovasc. Electrophysiol*, vol. 12, pp. 196–206, 2001.

[89] Wilders, R. and Jongsma, H. J., "Beating irregularity of single pacemaker cells isolated from the rabbit sinoatrial node," *Biophysical Journal*, vol. 65, pp. 2601–2613, 1993.

[90] Wu, T. J., Lin, S. F., Weiss, J. N., Ting, C. T., and Chen, P.-S., "Two types of ventricular fibrillation in isolated rabbit hearts," *Circulation*, vol. 106, pp. 1859–66, 2002.

[91] Zak, S. H., *Systems and control*. New York: Oxford University Press, 2003.

[92] Zipes, D. P. and Wellens, H. J. J., "Sudden cardiac death: Better understanding of risks, mechanisms, and treatment," *Circulation*, vol. 114, pp. 1134–1136, 2006.

VITA

Alejandro Garzon, the son of Hilda Leyton and Rafael Garzon, was born in 1975 in Florencia, a small city laying on the border where the Andean cordillera and the Amazon forest meet in the south of Colombia. After finishing high school, he moved to Bogota to pursue studies in the Medical School of Colombia National University. Two years later, dissatisfied with medical school, Alejandro transferred to the Physics Department where he concluded his undergrad studies and obtained a Master of Science with a thesis on nuclear physics. In 2003 he moved to Atlanta, United States, to begin doctoral studies at the Georgia Institute of Technology. After the completion of these studies, he plans to return to his country and find a faculty position. Apart from science, Alejandro's major interest is Tibetan Buddhism, specially the Geluk tradition.